January 2015

Ablation and Plasma Effects during Nanosecond Laser Matter Interaction in Air and Water

Yunfeng Cao
Purdue University

Recommended Citation

Cao, Yunfeng, "Ablation and Plasma Effects during Nanosecond Laser Matter Interaction in Air and Water" (2015). *Open Access Dissertations*. 1099.
https://docs.lib.purdue.edu/open_access_dissertations/1099

Graduate School Form 30
Updated 1/15/2015

PURDUE UNIVERSITY
GRADUATE SCHOOL
Thesis/Dissertation Acceptance

This is to certify that the thesis/dissertation prepared

By Yunfeng Cao

Entitled
ABLATION AND PLASMA EFFECTS DURING NANOSECOND LASER MATTER INTERACTION IN AIR AND WATER

For the degree of Doctor of Philosophy

Is approved by the final examining committee:

Yung Shin
Chair

Galen King

Fu Zhao

Gary Cheng

To the best of my knowledge and as understood by the student in the Thesis/Dissertation Agreement, Publication Delay, and Certification Disclaimer (Graduate School Form 32), this thesis/dissertation adheres to the provisions of Purdue University's "Policy of Integrity in Research" and the use of copyright material.

Approved by Major Professor(s): Yung Shin

Approved by: Jay P. Gore 9/22/2015
Head of the Departmental Graduate Program Date

ABLATION AND PLASMA EFFECTS DURING NANOSECOND LASER MATTER INTERACTION IN AIR AND WATER

A Dissertation

Submitted to the Faculty

of

Purdue University

by

Yunfeng Cao

In Partial Fulfillment of the

Requirements for the Degree

of

Doctor of Philosophy

December 2015

Purdue University

West Lafayette, Indiana

Dedicated to my family

ACKNOWLEGEMENTS

I would like to express my sincere gratitude to my academic advisor, Prof. Yung C. Shin, for his valuable advice, effective guidance, passionate encouragement, and kind support during my Ph.D study at Purdue. I also would like to thank Prof. Galen B. King, Prof. Fu Zhao, and Prof. Gary J. Cheng for serving on my committee, with all my heart for their great help and insight for my study.

I am thankful to my collaborators, Prof. Benxin Wu, Prof. Xin Zhao, Dr. Tylor Davis, and Prof. Chang Ye, who worked together with me on different projects and inspired me through fruitful discussions. Also my other lab mates, Prof. Hongtao Ding, Dr. Wenqian Hu, Dr. Shaoyi Wen, Xiaoyang Ye, and so many other persons, gave me a lot of help in many aspects and enriched my life at Purdue.

I am also grateful to Mr. Eric Holloway who provided me an opportunity to work as a Graduate Teaching Assistant in the First Year Engineering program, where I worked with Dr. Michele Strutz for two years and was recognized with a Magoon Teaching Excellence award.

Finally, I want to deeply thank my parents and my wife for their selfless love, support, and encouragement during my Ph.D study and in my whole life.

TABLE OF CONTENTS

LIST OF TABLES

LIST OF FIGURES

Figure Page

Figure Page

Figure Page

Appendix Figure Page

ABSTRACT

Cao, Yunfeng. Ph. D, Purdue University, December 2015. Ablation and Plasma Effects during Nanosecond Laser Matter Interaction in Air and Water. Major Professor: Yung C. Shin, School of Mechanical Engineering.

Despite extensive research work, a clear understanding of laser matter interaction in the high energy nanosecond laser ablation process is still lacking, which may differ significantly depending on surrounding medium, laser parameters, and target material characteristics. The mechanical and thermal effects of the confined plasma and water breakdown plasma during laser ablation in water have not been fully investigated as well.

In this work, nanosecond laser ablation of metal targets in air and water is investigated through a self-contained hydrodynamic model under different laser fluences with the consideration of phase explosion. In case of nanosecond laser ablation of aluminum in water, deeper crater depths are found in all the conditions studied in this work. The analysis of the shock compression in air and water indicates that the shock compression is mainly responsible for this enhancement of ablation in water.

The mechanical effects of confined plasma is also investigated, including the target surface integrity change and induced residual stresses in the Laser shock peening (LSP) process and shock wave propagation and spallation behavior in LSP. By combining a 3-D finite element model with a previously developed confined plasma model, the residual

stresses induced in the substrate material as well as the indentation profile on the substrate surface are predicted for both single shot and overlapping LSP. The spallation induced by shock wave propagation in targets during the laser shock peening process is also investigated in this work. The spallation zone location is calculated for various materials with different thickness of foils and various laser shock peening parameters and validated against with previously reported experimental results.

The melt ejection behavior during nanosecond laser ablation with phase explosion is successfully predicted by combined molecular dynamics (MD) and smoothed particle hydrodynamics (SPH) simulations and validated against the experiments. The commonly adopted 0.9 T_c (critical temperature) criterion for phase explosion boundary is also assessed with the prediction of the ablation depth for both aluminum and copper, and it is found that the 0.9 T_c criterion does not always work.

Laser induced water breakdown plasma, which is generated by the strong interaction between nanosecond laser and water, is used in this work to etch the surface layer of a carbon fiber reinforced composite sample. It is found that the polymer layer can be effectively removed by the plasma while the carbon fiber remains almost intact.

CHAPTER 1. INTRODUCTION

1.1 Background

A sudden removal of material from a surface due to irradiation by a pulsed laser beam is generally called laser ablation. During a nanosecond (1 ns = 10^{-9} s) laser ablation process, the interaction between a high energy laser beam and the target material will lead to the strong ablation of the target and consequently the formation of a crater on the target surface (Von Allmen, 1987). A lot of research work has been devoted to the investigation of ablation behavior in the nanosecond laser ablation process, which may differ significantly depending on surrounding medium, laser parameters, and target material characteristics. Most investigations on nanosecond laser ablation fall into two categories: in air (Porneala and Willis, 2006; Miotello and Kelly, 1999; Gusarov and Smurov, 2003; Fishburn et al., 2000; Gristoforetti et al., 2008; Vladoiu et al., 2008; Gragossian et al., 2009; Lu, 2003; Domer and Bostanjoglo, 2003) or in liquid (typically water) (Nichols et al., 2006; Kang et al., 2008; Mahdieh et al., 2010; Kim and Lee, 2001; Dupont et al., 1995; Kang et al., 2006; Mariella et al., 2010; Chen et al., 2006; Ohara et al., 1997).

Figure 1.1 is a schematic diagram for nanosecond laser matter interaction in air and water. When the surrounding medium is air, as shown in Figure 1.1 (a), a short pulse laser (typically about 1- 20 ns) is focused directly onto a solid workpiece. If the laser beam is intense enough, the strong interaction between the laser pulse and the workpiece will evaporate and also ionize the workpiece to form a high temperature plume and plasma near the target surface, which will expand into the air along with a shock wave. Under higher fluence, some liquid melts and droplets might be ejected explosively from the melt pool after the initial ablation by evaporation and ionization as depicted in Figure 1.1 (a), which is usually referred to as phase explosion or explosive boiling (Miotello and Kelly, 1999).

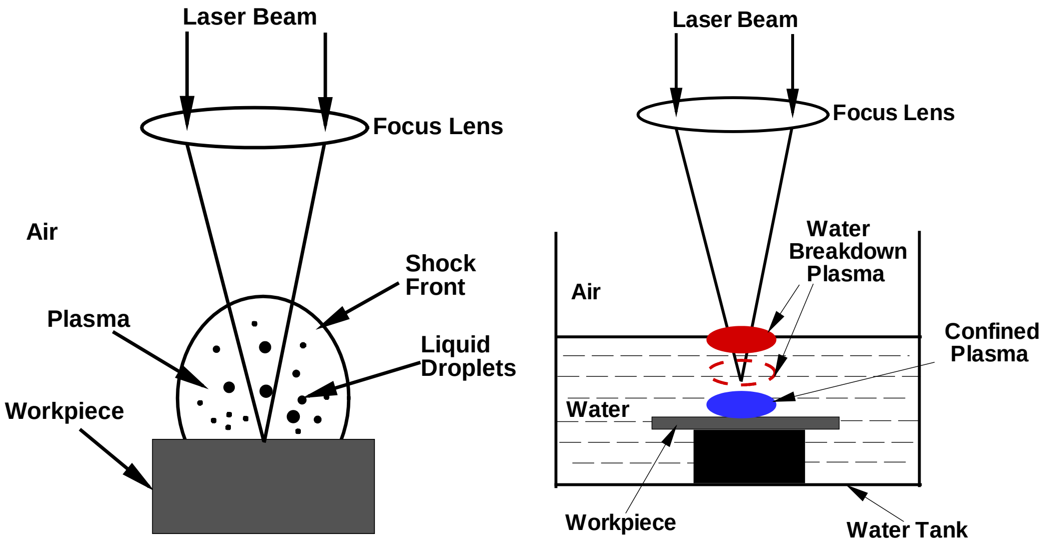

(a) (b)

Figure 1.1. Schematic diagrams for laser matter interaction in (a) air and (b) water.

When the surrounding medium is water, as shown in Figure 1.1 (b), a short pulse laser is irradiated through the water layer onto the workpiece surface. Under this configuration, the strong interaction between the laser pulse and the workpiece will ionize both the workpiece and water vapor immediately above the workpiece surface, which will finally form the so-called "confined plasma". The expansion of the produced confined plasma is suppressed by the confinement layer, thus creating a high magnitude (in the order of ~ GPa) recoil pressure pulse that may last longer than the laser pulse duration, which will send a shock wave into the workpiece. When the pressure of the shock wave exceeds the dynamic yield strength of the metal workpiece, plastic deformation occurs and residual stresses are induced, which will modify the near-surface microstructure and mechanical properties (Charles et al., 2002). In a closely-related process, laser shock peening, a coating layer is applied on the surface of the workpiece to protect the surface from the thermal damage due to the laser-coating interaction. In the laser shock peening process, the confined plasma and its expansion as a shock wave into the workpiece clearly play a very important role in the residual stress generation and plastic deformation in the sub-surface region of the workpiece.

A water layer is generally transparent to a laser beam. However, when the laser power density is above certain thresholds, water breakdown may occur, and the "breakdown plasma" is generated, by which a significant amount of incident laser energy will be absorbed. It should be noted that the plasma initially forms at the laser focal spot (dashed ellipse in Figure 1.1 (b)) if the laser power density at the focal spot just exceeds the breakdown threshold. If the laser power density is much higher than the water breakdown threshold, the laser power density at the air–water interface may be high enough to break down the water at the air–water interface. Therefore, the water breakdown plasma could be observed in any region from the focal spot (dashed ellipse in Figure 1.1 (b)) to the air–water interface (solid ellipse in Figure 1.1 (b)) depending on the laser power density. The optically opaque water breakdown plasma is usually considered to be detrimental for the laser ablation process since it blocks the laser-target interaction. However this extremely hot plasma could be useful in certain applications by effectively utilizing the plasma-matter interaction from the thermal point of view. This thermal effect has rarely been reported in literature.

As laser ablation is finding new applications in numerous manufacturing processes, a thorough understanding of laser matter interaction becomes more critical. During the laser matter interaction in air and water as shown in Figure 1.1, there are still lots of phenomena that are not completely understood. When the laser fluence is high enough during laser ablation in air, explosive ejection of melt and liquid droplets has been observed. However, the detailed mechanism of this phenomenon is not fully understood and theoretical investigations of this phenomenon are missing. The ablation rate was also found to be higher in the water than in the air (Kang et al., 2008; Mahdieh et al., 2010; Kim and Lee, 2001; Dupont et al., 1995; Kang et al., 2006). However, there are no satisfactory explanations for this material behavior due to the lack of understanding of laser ablation mechanism. The mechanical and thermal effects of the confined plasma and the water breakdown plasma are not fully understood as well and deserve more in-depth investigations.

This study seeks to investigate the nanosecond laser ablation process in air/water and the plasma effect during the laser matter interaction to obtain a better understanding of the process shown in Figure 1.1.

1.2 Literature Review

1.2.1 Nanosecond Laser Ablation Mechanism

Depending on the laser parameters, the absorption of laser energy may induce melting, normal evaporation, normal boiling, and eventually phase explosion if the laser fluence exceeds a certain threshold. No mass removal is involved during the melting process. Therefore it will not be discussed here.

A) Normal Evaporation

Normal evaporation is the escape of the molecules or atoms from a liquid surface to the ambient gas, which will occur whenever the saturation vapor pressure at the liquid surface temperature is higher than the pressure of the ambient gas (Xu and Willis, 2002). In nanosecond laser ablation on metal targets, material evaporation is the major ablation mechanism in the low fluence range (typically less than several J/cm^2), where the target material vaporizes directly from the surface of the liquid melt pool.

During normal evaporation the vapor particles leaving the surface have velocity components in the direction away from the surface and develop to an equilibrium normal velocity distribution over the distance of several mean free paths (known as Knudsen layer) due to collisions among particles (Wu and Shin, 2006c). The vapor above the Knudsen layer experiences an adiabatic expansion and eventually forms a shock wave, which could be considered as a gas dynamic flow with the continuum approximation (Wu and Shin, 2006c).

B) Normal Boiling

Another possible mass removal mechanism is normal boiling. Similar to the evaporation, boiling also involves the liquid-vapor phase change. However, during boiling the development of the vapor bubbles occurs below the liquid surface, while during evaporation the vapor escapes from the liquid surface. The boiling process heavily relies on the presence of heterogeneous nucleation sites (such as solid impurities or solid/liquid interface). Miotello and Kelly (1995) suggested that the density of heterogeneous bubble nucleation sites is too small to induce a significant boiling process capable of producing the high rates of material removal achieved in most nanosecond laser ablation processes. Also, the time for growth of heterogeneous nuclei is too long compared to the time scale of heating process (Miotello and Kelly, 1999). Therefore, the effect of normal boiling is considered negligible in this work.

C) Phase Explosion

With the increase of laser fluence, the surface temperature of the target material may rise close to 90% of the critical temperature or even higher (Porneala and Willis, 2006; Miotello and Kelly, 1999). Under this condition, phase explosion will occur and may start to dominate the ablation process. An observable jump in the ablation rates has been reported in literature (Gragossian et al., 2009; Lu et al., 2002; Porneala and Willis, 2006) when the laser fluence reaches a threshold value, which marks the transition from normal evaporation to phase explosion.

The existence of phase explosion has been reported in literature for nanosecond laser ablation both in air (Porneala and Willis, 2006) and in water (Nichols et al., 2006). For laser ablation of aluminum in air, time-resolved shadowgraph images (Porneala and Willis, 2006) indicate that the phase explosion occurs at around 52 ns after the laser pulse under the laser fluence of 5.2 J/cm^2. Nichols et al. (2006) investigated the nanosecond laser ablation on a platinum target in water, and found small droplets with sizes ranging from 100 nm to 1 μm inside the crater formed by laser ablation under the laser fluence of 11 J/cm^2, which indicates that molten droplets were ejected from the target and then fell into the crater after laser ablation.

Phase explosion can affect the resultant crater shape and the amount of material removed from the target. However, the detailed mechanism of phase explosion is not fully understood and theoretical investigations on the evolution of phase explosion are still missing.

1.2.2 Melt Ejection during Phase Explosion

It is generally known that the laser ablated material consists not only of evaporated atoms, but also particles or droplets formed, either directly by the laser–solid interaction, or later, through condensation (smaller particles condense onto the larger particles), collision between particles, or hydrodynamic sputtering (large particles) in the expanding plume.

In the low laser power density regime, the particles/droplets are mainly in the nano or sub-micron scale, which are formed mainly through laser evaporation (Becker et al., 1998). A number of models have been reported to describe particle formation and growth in the expanding vapor plume, based on condensation and nucleation theories (Kar and Mazumder, 1994; Gnedovets et al., 1999 & 2000; Gusarov et al., 2000; Blair et al., 2001). In general, condensation droplets are typically formed in long-pulse (ms) and low-intensity (10^4–10^5 W/cm^2) regimes (Gnedovets et al., 1999); however, they can also be generated at higher laser intensity and shorter pulse (e.g. 10^8–10^{10} W/cm^2 and few ns pulse) under the slow expansion of the vapor plume into the background gas (Brailovsky et al., 1995).

With the increase of laser fluence, the surface temperature of a target material may rise close to 90% of the critical temperature or even higher (Porneala and Willis, 2006; Miotello and Kelly, 1999). Under this condition, phase explosion will occur and may start dominating the ablation process. In this high fluence regime, larger particles/droplets may form with different mechanisms depending on target material and laser conditions. It was proposed based on experimental observation that the vaporized atoms and ions condense as tiny particles on the ejected larger droplets, forming an outer layer and even larger particles (Liu et al., 2005). For metals, particles are assumed to be formed by liquid (large droplet) ejection, which can be the result of several processes. Large droplets can be ejected as a result of transient melting and motion of a liquid caused by steep pressure gradients and the vapor plume recoil pressure (Muhammad et al., 2013; Tong and Browne, 2011; Von Allmen, 1987; Bennett et al., 1995). The formation of large droplets is assumed to be from the collision between small particles. According to Hergenroder (2006), hydrodynamic sputtering may also play a very important role on the large particle formation in a laser ablation process.

At high laser power density, the particle size was measured to have a bimodal size distribution (Hergenroder, 2006). Clearly, there are two mechanisms for the particle generation. One is the evaporation induced by laser ablation, which corresponds to the lower peak in the particle size distribution. The other one is due to either condensation, collision between small particles, or hydrodynamic sputtering, which corresponds to the higher peak.

It still remains a difficult challenge to capture the ejected droplets during the material removal by conventional modeling methods (for example, Hydrodynamics model) using generated mesh. The meshes need to be several times smaller than the ejected molten materials, which require massive computing resources. Lu (2003) proposed a one-dimensional fluid model to describe the thermodynamic evolution during phase explosion. However, Lu's model couldn't predict the melt ejection behavior and the resulting ablation depth. As a work-around, most researchers use 0.9 T_c (critical temperature) as the ablation depth prediction criterion when handling phase explosion (Yoo et al., 2000; Lu et al., 2002; Gragossian et al., 2009). In the authors' previous work (Cao et al., 2013), 0.9 T_c as the ablation depth prediction criterion was shown to yield good accuracy when predicting the ablation depth for aluminum with phase explosion. However, it was found that 0.9 T_c doesn't work when dealing with a copper target.

There are some numerical methods proposed in literature to capture these nonlinear phenomena, such as molecular dynamics (MD) and smoothed particle hydrodynamics (SPH). Molecular dynamics (MD) simulation provides an explicit atomistic representation of material heating, vaporization, and plume expansion, and solves problems that cannot be accounted for by continuum models, such as highly non-equilibrium states and fast phase transformations induced by high fluence laser irradiation (Zhigilei and Ivanov, 2005). The interatomic potential V is one of the most important parameters governing MD simulation of a certain material, because this potential defines the interactions among atoms that the material consists of and dominates the properties of the material (Allen and Tildesley, 1989). The force exerted on each atom by other atoms is also determined by the interatomic potential. Therefore, once the interatomic potential is given, MD can be used to simulate many problems with their specific external forces, initial conditions and boundary conditions.

MD simulation work reported in literature is mainly focused on the femto- or picosecond laser ablation, where a relatively short laser heating makes it possible for atomic scale modeling. Very few reports are available on the nanosecond laser ablation with MD simulation. Perez et al. (2006) investigated the nanosecond laser ablation of molecular solids with MD. However the approach is not expandable to metal targets since metals have much higher melting temperature than the molecular solids and therefore require much longer heating time. Zhang and Wang (2008) proposed a hybrid model to investigate the long-time phase change in nanosecond laser-material interaction. In their approach, MD domain is used to capture the laser heating, while the finite difference domain is used to consider the heat conduction in the deeper region. The time scale is still limited to around 60 ns in this hybrid method and therefore it is not possible to predict the phase explosion process.

SPH is a meshless computational method represented by a set of particles where each particle moves according to the governing dynamics (Manenti, 2009). In SPH, differential equations are therefore solved by a Lagrangian technique. The basic concept of SPH is that continuous media are represented by discrete particles with volume, density and mass. The particles have a kernel function to define their range of interaction, and the hydrodynamic variables are approximated by integral interpolations. Meshes are not needed in the simulation, which is a major advantage of SPH over Eulerian methods for complex geometries. However, since SPH is a mesoscale method (Manenti, 2009) that deals with the particle size in the sub-micron to micron range, SPH alone can't predict the initial particle formation in the laser ablation process, where the initial particle size could be far less than 1 micron.

1.2.3 Mechanical Effects of Confined Plasma

As discussed in the previous section, confined plasma will play an important role in the laser shock peening (LSP) process, where high energy laser irradiated on the target surface can generate high-pressure plasma in the water confinement regime (Berthe et al., 1997; Wu and Shin, 2005). When the pressure wave propagates into the substrate material as a shock wave, compressive residual stresses can be imparted into the surface region (Braisted and Brockman, 1999), which in turn can improve the material's fatigue properties and wear resistance. To protect the surface from the thermal damage that may occur in the process of

LSP, a coating layer of black paint or aluminum tape is usually applied on the surface of substrate material.

Fabbro et al. (1990) proposed a very straightforward 1-D analytical model to consider the physics of the confinement of laser-generated plasmas by a transparent overlay (glass). The ratios of plasma thermal energy to internal energy and laser-plasma absorption coefficient were treated as free variables that have to come from experimental measurements. This model was later improved by Sollier et al. (2003) and Zhang et al. (2004). However, the laser-plasma absorption coefficient remains a constant in these models. Wu and Shin (2005) proposed a self-closed thermal model to consider the LSP under water confinement, which has no free variables and has considered most of the important physical phenomena, including the laser ablation of the coating layer, water evaporation, plasma ionization and expansion, laser-plasma interaction, etc.

The finite element simulation of laser shock peening and induced residual stress has been reported in the literature (Braisted and Brockman, 1999; Ding and Ye, 2003a; Ding and Ye, 2003b). In their approaches, the ABAQUS/Explicit and ABAQUS/Standard were combined to simulate the short duration shock wave propagation and the resulting residual stresses in the target material. The target material was considered as perfectly elastic-plastic even under very high strain rates and the dynamic yield strength was connected with Hugoniot Elastic Limit (HEL) and Poisson's ratio by a simple expression. Peyre et al. (2003; 2007) employed a Johnson-Cook type model to describe the dynamic behavior of target materials during LSP. Warren et al. (2008) simulated the multi-pass LSP on AISI 52100 steel without a coating layer. The overlapping effect of laser shock peening of AISI 1045 steel was investigated by Hu and Yao (2008). The changes of mechanical properties of the specimen treated by different overlapping rates were investigated by both experiments and FEM simulation. Voothaluru et al. (2012) also investigated the overlapping effect of laser shock peening using FEM simulation. Vasu and Grandhi (2013) studied the effect of curved geometry on residual stress in laser shock peening with FEM. By using either a concave or a convex geometry, the residual stress induced by laser shock peening could be altered. However, the inputs of these finite element models, the confined plasma pressure, mostly come from the simple analytical model proposed by Fabbro et al. (1990), which has two free variables.

A considerable amount of experimental work on single shot LSP has been reported (Berthe et al., 1997; Sollier et al., 2003; Hill et al., 2005), most of which is related to the residual stress measurement and the effect of LSP parameters on the induced residual stresses in the target material. For single-track and multi-track overlapping LSP, only a limited amount of work is available in literature. Zhang and Yao (2002) investigated the micro scale laser shock processing on a copper foil of thickness 90 μm. The laser beam employed in their work is only 6 μm in radius. They concluded that it is possible to impart desirable residual stress distribution into micro scale metallic components by properly choosing laser intensity, number of pulses and overlapping ratio. Rubio-Gonza´lez et al. (2006) conducted a multi-pass LSP on 6061-T6 aluminum alloy with non-bright black paint coating. They examined the effect of absorbent coating on the residual stress induced by LSP. Dorman et al. (2012) investigated the effect of LSP on residual stress and fatigue life of clad 2024 aluminium sheet. The induced residual stress field was measured using incremental hole drilling and synchrotron X-ray diffraction techniques. They found out that the overlapping of laser shot results in the large compression strains.

Despite the abundant work in this area as reviewed in this section, complete predictive modeling on the change of target surface integrity and residual stresses by single shot and overlapping LSP has rarely been reported, which must take into account of the accurate laser-induced plasma pressure with strict physics-based theories.

The confined plasma model developed earlier by Wu and Shin (2005) can be used to calculate the plasma pressure generated during LSP in a water confinement regime. In their model, the plasma expansion was treated as a one-dimensional phenomenon because the two-dimensional effects are important only when the laser beam diameter is very small. Wu and Shin (2007b) further demonstrated that the 1-D assumption is valid when the laser beam diameter is equal or larger than 300 μm. Wu and Shin (2007c) also developed a FEM model and combined with the confined plasma model to predict the residual stress generated in LSP. This is a complete and self-closed model which requires only the laser parameters and material properties to model the LSP process. Both the FEM model and the confined plasma model (Wu and Shin, 2005) will be employed in this work as a foundation to investigate the mechanical effects of confined plasma in LSP process.

1.2.4 Shock Wave Induced by Confined Plasma and Its Propagation

As reviewed in the previous section, high energy laser irradiated on the target surface can generate high-pressure plasma in the LSP process, (Berthe et al., 1997; Wu and Shin, 2005), which will propagate into the substrate material as a shock wave. If the shock wave amplitude and the duration of this shock wave are sufficient, spallation will take place at the interface or inside the bulk material.

Laser induced spallation is an experimental technique developed in the last several decades to understand the adhesion of thin films with substrates (Cottet and Boustie, 1989). A high energy pulsed laser (typically Nd:YAG) is used to create a compressive stress pulse in the substrate. This compressive stress wave propagates into the film and reflects as a tensile wave at the boundary. If the amplitude of the tensile stress wave is greater than the interface bonding strength, this tensile stress pulse spalls the thin film while propagating inside the substrate. Using the theory of wave propagation in solids it is possible to model the laser induced spallation process. The stress pulse created in this fashion is usually around 3-8 nanoseconds in duration while its magnitude varies as a function of laser fluence (Cottet and Boustie, 1989).

A typical laser spallation setup is shown in Figure 1.2. The constraining material is transparent to the laser pulse (usually water or glass). The expansion of laser ablation-induced plasma under the confinement generates a compressive stress pulse propagating toward the test coating, which is deposited on the substrate's back surface. When this shock wave reaches the interface, it is partially transmitted and then reflected in a release wave on the free surface of the coating. Since the loading has a short duration, the incident shock is also rapidly followed by another release wave and the crossing of both generates a tensile stress at the interface, which will finally lead to spallation (complete removal).

The critical stress at the interface can be calculated by measuring the transient displacement history of the coating's free surface, which is induced during pulse reflection, by using an optical interferometer in the single shot mode. Gupta et al. (1994) related the measured free surface velocity to the local interface stress via wave mechanics-based simulation.

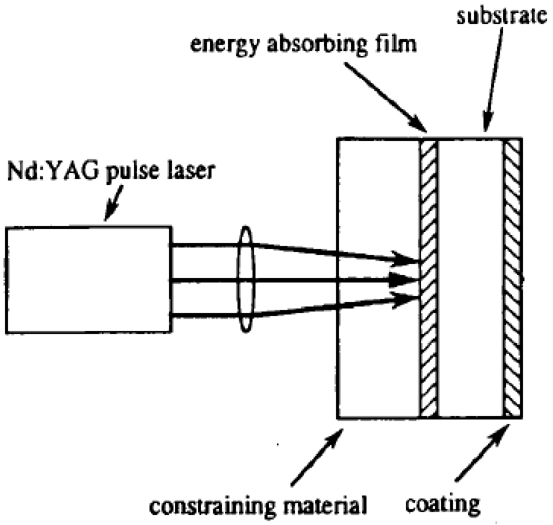

Figure 1.2. Scheme of laser spallation with water confinement (Gupta et al., 1994).

In Auroux et al.'s (2001) work, the laser beam was focused on the bare face of the substrate to create a plasma whose expansion induced a shock wave into the target. The target was placed in a vacuum chamber to avoid air breakdown because the laser intensity used in the experiment was extremely high. They found that the laser intensity required to spall the coating from the substrate is highly dependent on substrate thickness and laser pulse duration. One interesting observation from their work is that the spallation can occur in the substrate instead of at the interface if the laser pulse is long enough, as shown in Figure 1.3.

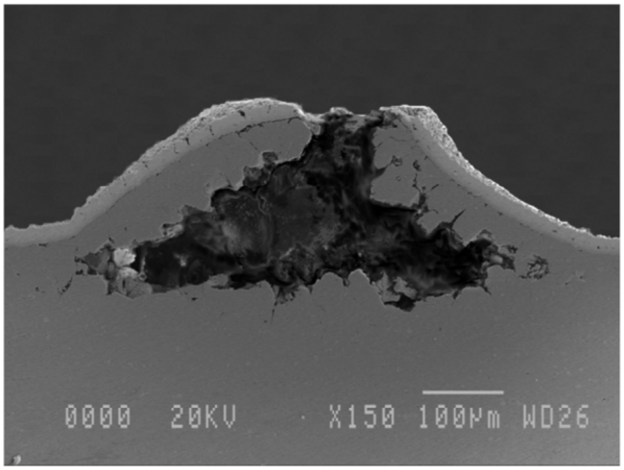

Figure 1.3. SEM observation of a cohesive rupture into Hastelloy X coated with diffused Pt and irradiated on the opposite surface with an intensity of 0.8 TW/cm^2 (Auroux et al., 2001).

Cottet and Boustie (1989) first introduced hydrodynamic equations and an elastoplastic model to simulate the shock wave propagation induced by laser irradiation. They also employed a cumulative damage criterion to describe the spallation process. Their model can predict the general behavior of spallation, including the spall thickness and spallation threshold in different conditions. Fortov and Kostin (1991) modified the above model by introducing a continuous kinetic model of spallation, which took into account the duration of loading and effective stress. Once the maximum tensile stress reaches the threshold value, the spallation process starts and the voids inside the material begin to grow. The stress relaxation after the crack was also considered in this model. It should be mentioned that the pressure wave input for the above two models were both from the simple analytical scaling law, which generates significant errors in the pressure wave predictions.

To avoid this input error, Tollier et al. (1998) measured the rear free surface velocity using the velocity interferometer system for any reflector (VISAR) and estimated the pressure loading based on their measurement. By applying the continuous kinetic model, they also investigated the spallation process for aluminum and copper films. Using a same approach, Bolis et al. (2007) studied the coating/substrate adhesion strength.

The direct laser irradiation configuration used by all of the above works has disadvantages compared with those using a confinement regime for the study of laser spallation process. In the case of LSP in a confinement regime, plasma expansion is suppressed by the confining medium (usually water or glass), which leads to the generation of pressure waves higher and longer than those in the direct regime under the same laser parameters (Berthe et al., 1997; Wu and Shin, 2005; Bolis et al., 2007). Therefore, it is desirable to investigate the laser spallation process under a confinement regime by predictive modeling.

1.2.5 Thermal Effects of Laser-Induced Plasma - Etching

Carbon fiber-reinforced plastic (CFRP) is a composite material made of a polymer matrix reinforced with carbon fibers, which is widely used in aerospace, automotive, and civil industries due to their superior material properties and light weight (Hull and Clyne, 1996). Under excessive tensile force, however, shear failure can occur at the interface between the fibers and polymer matrix (Puck and Schurmann, 2002). As the application of composite materials becomes more extensive, the need for repair of damaged composite parts grows.

Conventional repair of the composite structures (Armstrong, 1997) is done by grinding the damaged part manually using a diamond angle grinder and then refilling the cavity with preimpregnated ("pre-preg") plies. Finally the whole system must be cured with the vacuum bag technique. This mechanical grinding process is time-consuming and highly depends on the expertise of the repair personnel. Furthermore, mechanical stresses could be introduced into the workpiece. Laser-based repair of composite materials was proposed recently (Fisher et al., 2010), where direct laser ablation was utilized to remove the damaged part to obtain a cavity for further refilling. The major disadvantage of the method proposed by Fisher et al. (2010) is that both the polymer matrix and the carbon fibers were completely removed by direct laser ablation under high laser fluence, which will significantly affect the material strength of the repaired patch since the fibers were broken.

One of the better alternatives to repair the damaged composite material is to etch the polymer matrix only and then refill the polymer to generate a new bond between the polymer and the carbon fibers. This method appears to be cost-effective but has never been reported in literature. Etching by laser induced water breakdown plasma, which is generated by the strong interaction between nanosecond laser and water (Horvat et al., 2010; Berthe et al., 1998; Saarela et al., 2010; Berthe et al., 1997; Kudryashov and Zvorykin, 2008), is therefore proposed in this work to remove the polymer matrix from a carbon fiber reinforced composite sample more effectively based on the state-of-the-art of the composite material repair.

By focusing an incident high power laser beam in water, extremely high peak power density can be generated at the focal spot. When the peak power density exceeds the ionization threshold of the water, the strong laser-water interaction will result in the generation of free electrons at the focal spot through multi-photon ionization. The cascade ionization process then becomes dominant for the fast growth of free electrons via inverse bremsstrahlung absorption. When the free electron density exceeds the critical value of

10^{20}/cm^3, optical breakdown of water occurs, leading to the formation of dense and optically opaque plasma at the focal spot (Berthe et al., 1999).

The etching (material removal) by the laser induced water breakdown plasma starts with laser-water interaction and then becomes a thermal-kinetic process, which can be explained by the plasma-matter interaction (Pallav et al., 2011). From the thermal point of view, heat energy is transmitted from the extremely hot plasma to the workpiece through conduction (if the plasma touches the workpiece surface) and/or radiation (if the plasma is away from the workpiece surface) over a relatively small area of the workpiece during the plasma-matter interaction. As a result, the local temperature of the workpiece will experience a sudden increase. When the temperature exceeds the boiling point, the high temperature region of the workpiece will be melted or even vaporized. From the kinetic point of view, the plasma also occupies the initial water region (see Figure 1.1 (b) for more details about the plasma position) and applies a large pressure on the workpiece surface, which holds back the molten material. As soon as the plasma collapses at the end of the laser pulse, the water flows back rapidly to fill the void. The sudden decrease in pressure due to the plasma collapse also results in an instantaneous expulsion of the molten and vaporized material from the workpiece surface, thus resulting in material etching (Pallav et al., 2011). Since the polymer matrix has a lower boiling temperature (in the order of several hundred Kelvins (Wolynski et al., 2011)) than the carbon fibers (in the order of several thousand Kelvins (Wolynski et al., 2011)), the polymer matrix will be vaporized first.

1.3 Research Objectives

In the review above, some important issues that remain unsolved have been identified for laser-matter interaction in air/water. The objective of this research work is to address these issues via numerical modeling and experiments:

1. Investigate the nanosecond laser ablation mechanism in air and water, specifically the enhancement of ablation rate in water and with phase explosion;

2. Study the melt ejection behavior during phase explosion through experiments and numerical modeling;

3. Explore the mechanical effects of confined plasma in LSP on various metal samples through predictive modeling and experimental studies, especially in the target surface integrity change and induced residual stresses in terms of laser parameters and overlapping ratio;

4. Develop a complete and general model for the confined plasma induced shock wave propagation and spallation during the laser shock peening process;

5. Investigate the thermal effects of a laser-induced water breakdown plasma for selective etching of the polymer from the composite material.

1.4 Thesis Outline

Research background, literature review, and research objectives have been presented in this chapter.

Chapter 2 will describe in detail the nanosecond laser ablation of metal targets in air and water through a self-contained hydrodynamic model under different laser fluences involving no phase explosion and phase explosion. The ablation depths and profiles are predicted and validated against the literature data and experiments. In case of nanosecond laser ablation of aluminum in water, deeper crater depths are found in all the conditions studied in this work, which may be attributed to the combination effects of laser ablation and shock compression.

Nanosecond laser ablation of metal targets with phase explosion is studied in Chapter 3 through a multi-scale model and experimental verification. The melt ejection behavior during phase explosion is successfully predicted by combined molecular dynamics and smoothed particle hydrodynamics simulations and validated against the experiments. The commonly adopted 0.9 T_c (critical temperature) criterion for phase explosion boundary is also assessed with the prediction of the ablation depth for both aluminum and copper, and it is found that the 0.9 T_c criterion does not always work for all materials.

The mechanical effects of confined plasma are presented in Chapter 4, including the target surface integrity change and induced residual stresses in the LSP process and shock wave propagation and spallation in LSP. To gain a better understanding of the laser-coating interaction in the LSP process, a series of experiments, including single shot, single-track overlapping, and multi-track overlapping LSP, have been carried out on various metals with different coatings. A 3-D finite element model has also been developed to simulate the LSP process. Combining this with the previously developed confined plasma model, which has been verified by the experimental data from literature, a 3-D finite element model is used to predict the residual stresses induced in the substrate material as well as the indentation profile on the substrate surface. The model prediction of indentation profiles is compared with the experimental data. The residual stresses in the depth direction are also validated against the X-Ray diffraction (XRD) measurement data for 4140 steel and Ti-6Al-4V. The effect of process parameters on the residual stress is also investigated both experimentally and theoretically.

The spallation induced by shock wave propagation in targets during the laser shock peening process is also investigated in Chapter 4. Physical aspects concerning laser-matter interaction, shock wave propagation, and spallation are considered. A continuous kinetic model for the spallation process is included in a one-dimensional finite difference hydrodynamic code using Lagrangian coordinates in order to calculate the laser-induced spallation phenomena. Shock wave propagation in solids is calculated and validated against experimental data. The spallation zone location is then calculated for various materials with different thickness of foils and various laser shock peening parameters.

Chapter 5 introduces the thermal effects of water breakdown plasma. An etching process by water breakdown plasma is used in this work to etch the surface layer of a carbon fiber reinforced composite sample. It is found that the polymer layer can be effectively removed by the plasma while the carbon fiber remains almost intact. The dependence of the etching depth on the laser power density, laser focus position, and the number of shots are also investigated in this work.

The conclusions and proposals for future study are discussed in Chapter 6.

CHAPTER 2. NANOSECOND LASER ABLATION IN AIR AND WATER

2.1 Introduction

As reviewed in Chapter 1, phase explosion (PE) can affect the resultant crater shape and the amount of material removed from the target during nanosecond laser ablation. However, the occurrence of phase explosion is usually neglected when dealing with laser ablation due to its complexity, which could lead to incorrect understanding of the laser ablation process, especially in the high fluence range.

In this chapter, the nanosecond laser ablation rate of metal targets is investigated from low fluence to high fluence in air and water. Especially, the enhancement of ablation rate in water is investigated with the consideration of phase explosion. For nanosecond pulses with irradiances of several GW/cm^2, the plasma induced by laser ablation of metal targets can be described by the hydrodynamic (HD) equations for the whole physical domain, where the condensed phase contributes a mass to the plasma region mainly through hydrodynamic expansion. The laser-matter interaction and the plasma expansion can be treated as either one-dimensional (1D) (Wu and Shin, 2007a) or two-dimensional (2D) (Wu and Shin, 2007b) phenomenon depending on the laser beam diameter. Wu and Shin (2007b) demonstrated that the 1D assumption is valid only when the laser beam diameter is larger than 300 μm. Since the laser-beam diameter used in this work is around 100 μm, it is necessary to use the 2-D model to describe the interaction between the laser and target material.

2.2 Experiments and Simulation Methods

2.2.1 Experimental Setup

The experimental setup used in this study is shown in Figure 2.1. An Nd-YAG laser (wavelength 1064 nm) is used to generate a laser beam, which passes through a half-wave plate, polarizer, three high reflecting mirrors and a focus lens, and finally focuses on the surface of workpiece. The workpiece is placed into a water tank. The movement of workpiece in X and Y direction is controlled by two linear motion stages. With this setup, the laser power density can be easily adjusted by fine-tuning the orientation of the half-wave plate. The laser beam diameter focused on the workpiece surface can also be changed by varying the distance between the focus lens and the surface of the workpiece. The beam profile used in this work is nearly top-flat spatially. For laser ablation in air, the target will be simply put on the linear motion stage without the water tank.

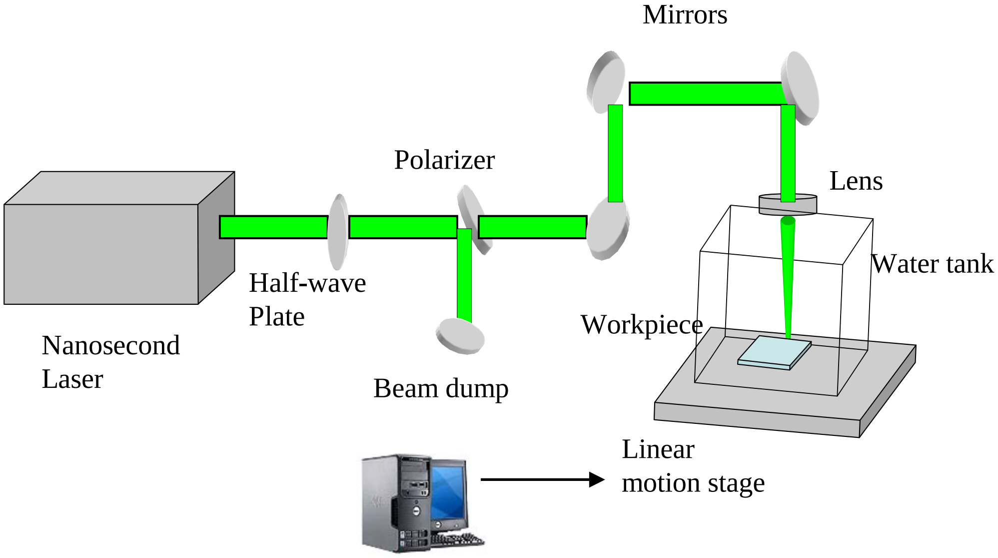

Figure 2.1. Experimental setup of laser ablation in water.

2.2.2 Two-Dimensional Hydrodynamics Model

The 2-D model set-up for the interaction of laser radiation with a target surface in a medium (air or water) is shown in Figure 2.2. At the beginning of calculation, the top half of the calculation domain is filled with the surrounding medium, while the aluminum target is located in the bottom half. Laser radiation comes from the top of the domain and propagates towards the aluminum target. For this system, the 2-D hydrodynamic (HD) equations can be expressed as (Wu and Shin, 2007b):

$$
\begin{aligned}
&\frac{\partial}{\partial t}\begin{bmatrix} \rho_1 \\ \rho_2 \\ \rho u \\ \rho v \\ E+0.5\rho\left(u^2+v^2\right) \end{bmatrix} + \frac{\partial}{\partial r}\begin{bmatrix} \rho_1 u \\ \rho_2 u \\ \rho u^2+P \\ \rho uv \\ u\left[E+0.5\rho\left(u^2+v^2\right)+P\right]+q_r+Q_r \end{bmatrix} + \\
&\frac{\partial}{\partial z}\begin{bmatrix} \rho_1 v \\ \rho_2 v \\ \rho uv \\ \rho v^2+P \\ v\left[E+0.5\rho\left(u^2+v^2\right)+P\right]+q_z+Q_z-I \end{bmatrix} + \frac{1}{r}\begin{bmatrix} \rho_1 u \\ \rho_2 u \\ \rho u^2 \\ \rho uv \\ u\left[E+0.5\rho\left(u^2+v^2\right)+P\right]+q_r+Q_r \end{bmatrix} = 0
\end{aligned}
\tag{1}
$$

where ρ_1 and ρ_2 are the densities of the metal and air (or water), respectively. ρ is the total density defined as $\rho = \rho_1 + \rho_2$. u and v are the velocities in r and z direction, respectively, P the pressure, E the volumetric internal energy, I the net flux in laser radiation in the z direction, q_r and q_z the heat flux of thermal conduction in r and z direction, respectively, and Q_r and Q_z the radiative heat flux in r and z direction, respectively.

The dynamic change of the whole system, including the water/air medium and target material, can be captured by this 2D HD model. The evolution of the target to evaporated material and to ionized material (plasma) can be calculated according to the laser energy inputs (Wu et al., 2007c). A recoil pressure (plasma pressure) is generated as the by-product of laser ablation and can also be calculated from this 2D HD model (Wu and Shin, 2007b).

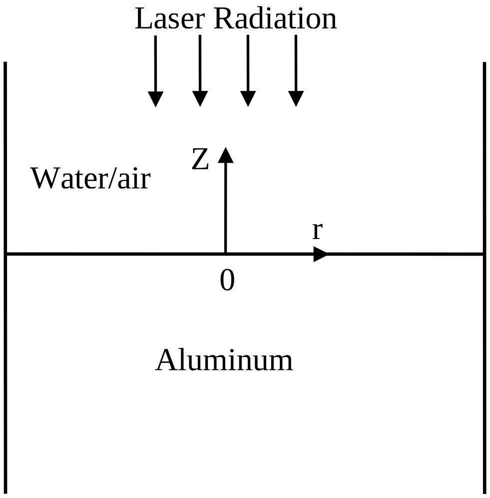

Figure 2.2. Schematic diagram of the 2-D model setup.

To solve the hydrodynamic equations, appropriate equations of state (EOS) must be employed. For the aluminum targets, the quotidian equation of state (QEOS) (Wu and Shin, 2007b; More et al., 1988) is applied, which is an EOS model for the hydrodynamic simulation of high-pressure phenomena. For water, the EOS table developed by Ree (1976) is applied, which covers a very wide range of density (0.002 Kg/m^3 ~ 4.0×10^5 Kg/m^3) and temperature (290 K ~ 2.9×10^5 K). For air, the ideal gas EOS is adopted when the air is not ionized. If the ionization of the air occurs, the electron part is added to the air pressure after obtaining the electron number density through Saha equations (Wu et al., 2007c).

The 2D HD equations are solved using a non-oscillatory central finite difference scheme (Liu and Osher, 1998). The numerical domain is chosen to be large enough such that there will be essentially no heat and mass transfer at the domain boundary. In the laser irradiated region, there is a heat flux into the material from laser irradiation. There is also mass transfer from the material into the surrounding medium through laser ablation. More details of the numerical method can be found in (Wu and Shin, 2007b; Wu et al., 2007c). It should be noted the code used in this work is mainly developed by Wu and Shin (2007b). Certain modifications have been made to extract the temperature information and therefore to predict the ablation depth under different laser conditions.

2.3. Results and Discussion

To validate the capability of the 2D HD code in the prediction of ablation depth, several laser ablation cases were first calculated in the air without phase explosion. The laser fluence was then further increased to investigate the transition from evaporation to phase explosion in nanosecond laser ablation. At the end, the laser ablation of aluminum in water under high fluence was also investigated both experimentally and numerically. The target material used in this work is aluminum. The evaporation and critical temperatures of aluminum are 2793 K and 5410 K (Fishburn et al., 2000), respectively. The laser parameters used in the calculation in this work are listed in Table 2.1. It should be noted that the laser beam diameter is measured at the full width at half maximum (FWHM) location.

Table 2.1. Laser parameters for laser ablation on aluminum.

Case Number	Ablation Medium	FWHM Diameter (μm)	Wavelength (nm)	Pulse Duration (ns)	Fluence (J/cm^2)	PE Threshold (J/cm^2)
1	Air	120	266	6.0	10~25	30.0[1]
2		150	532	40.0	20~100	150.0[2]
3		100	1064	10.0	1~5	7.5[3]
4	Air	100	1064	10.0	1~20	7.5[3]
5		100	1064	5.0~35.0	5~35	7.5[3]
6		100	266~1064	10.0	5, 15	7.5[3]
7		1000	1064	6.0	24	5.2[4]
8	Water	1000	1064	6.0	10~50	5.2[4]

Note: [1] Data taken from Gusarov and Smurov, 2003; [2] Data taken from Fishburn et al., 2000; [3] Data taken from Fishburn et al., 20001; [4] Data taken from Porneala and Willis, 2006.

2.3.1 Laser Ablation in Air without Phase Explosion

Evaporation temperature was used as the ablation criterion in this low fluence condition by assuming all the materials with temperature higher than evaporation temperature will be ablated. To compare with published data (Gusarov and Smurov, 2003; Fishburn et al., 2000; Gristoforetti et al., 2008), the calculation domain is chosen to be 500 μm in depth and 500 μm in radius. The lower half of the calculation domain is filled with target metal, while the upper half is air. The laser beam irradiates the target surface in the center of the calculation domain. In all three cases (case 1-3 in Table 2.1), the laser fluences used were below the phase explosion threshold values.

The crater profile of laser ablation of aluminum in air is calculated by the 2D HD model. Figure 2.3 shows several typical crater profiles after single shot laser ablation. The comparison of predicted ablation depth with experimental data under different laser fluence is shown in Figure 2.4. Good agreements are obtained for all three cases, which indicate that the ablation criterion (evaporation temperature) works well for the low fluence range. Only exception is case 2 with the longest laser pulse (40.0 ns), where the simulation results are much smaller than the experimental data in ablation depth. In this case, the experimental data were taken as the average ablation depth from a multiple-pulse laser ablation experiment, where the so called "incubation effects" (Ashkenasi et al., 1999) may have lowered the ablation threshold and therefore increased the average ablation depth. Also, the discrepancy between the experimental data and the simulation results is getting larger with the increase of the laser fluence, which implies that a different ablation mechanism might take place with higher laser intensity.

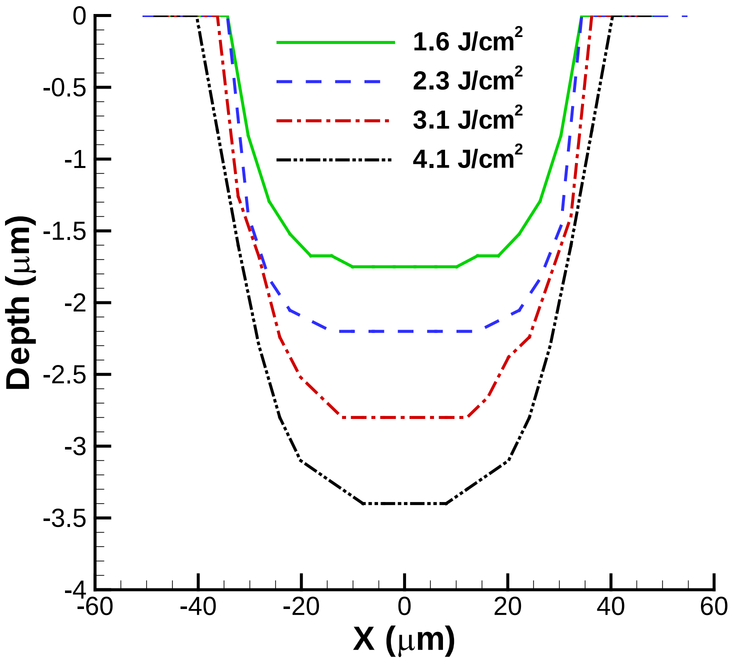

Figure 2.3. Crater profile after laser ablation of aluminum in air (laser pulse duration 10.0 ns, laser wavelength 1064 nm, beam diameter 100.0 μm, top-hat beam, single shot ablation).

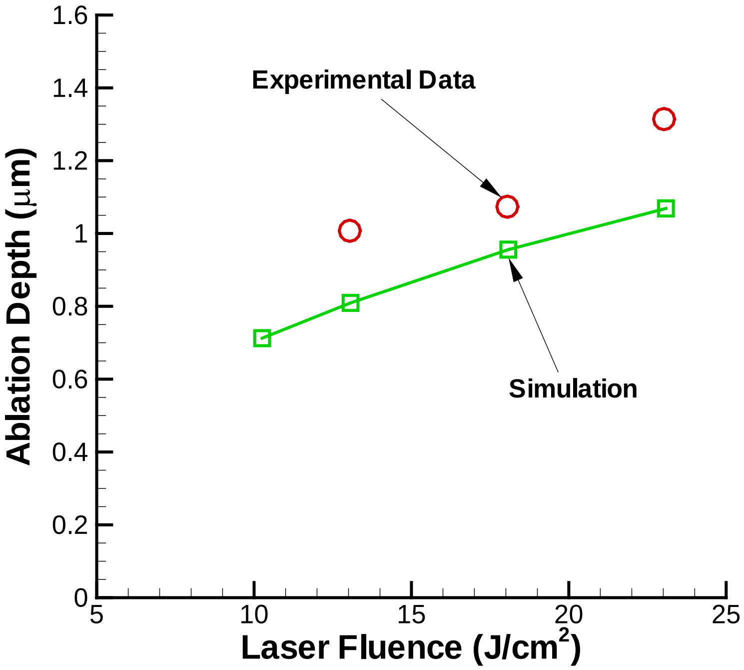

(a)

Figure 2.4. Comparison of ablation depth under different laser fluence with different laser system (a) Case 1, top-hat beam, experimental data from Gusarov and Smurov (2003) (b) Case 2, Gaussian beam, experimental data from Fishburn et al. (2000) (c) Case 3, top-hat beam, experimental data from Gristoforetti et al. (2008).

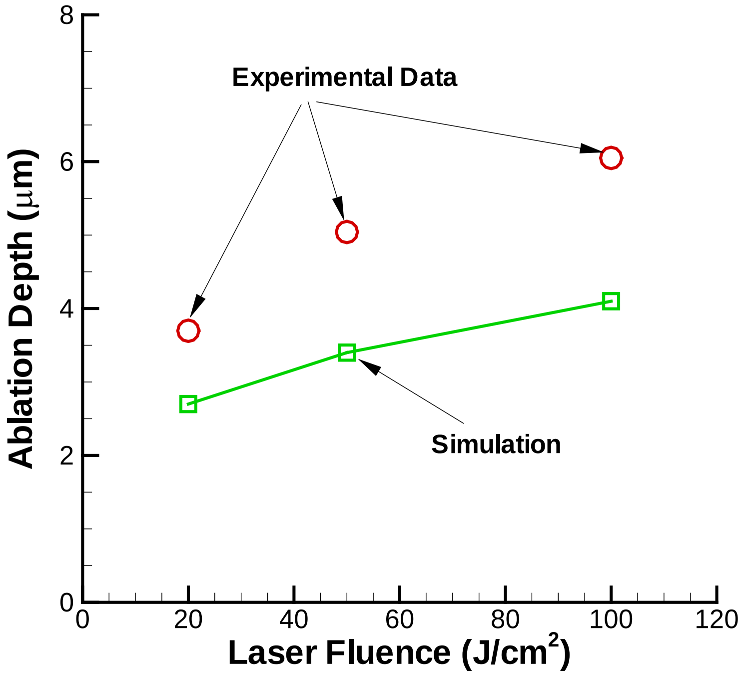

(b)

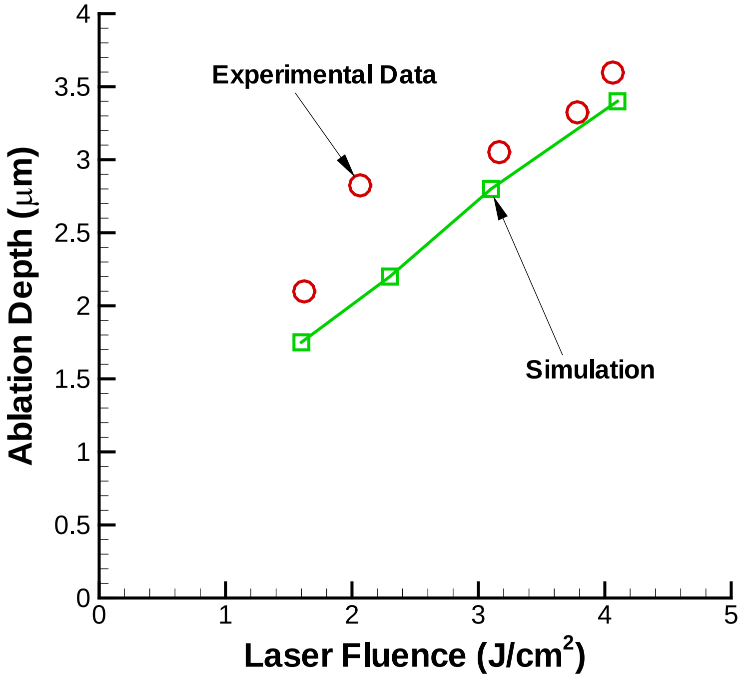

(c)

Figure 2.4. Continued.

For case 1 to 3 investigated here, the ablation depth shows a near linear dependence on the laser fluence in the low fluence range, where no phase explosion occurs.

2.3.2 Laser Ablation in Air with Phase Explosion

The laser ablation of aluminum in air with higher fluence is calculated by the 2D HD model. In this case, the phase explosion will occur and the ablation criterion is defined as the 90% of the critical temperature (0.9 T_c) (Gragossian et al., 2009).

The ablation depth of aluminum under different laser fluence is shown in Figure 2.5 for Case 4. In this case, the laser fluence is more than 10 J/cm^2, which is higher than the threshold for phase explosion (7.5 J/cm^2) as listed in Table 2.1. The agreement between the model prediction and the data from Gragossian et al. (2009) is very good in the fluence range between 10 and 20 J/cm^2, which is a strong validation of the 2D HD model in the high fluence range. To show the trend of the ablation depth with the increase of laser fluence, the ablation depth in the lower laser fluence range is also calculated and plotted in Figure 2.5. Clearly, there is a sharp increase of ablation rate around 10 J/cm^2, which indicates that a transition from evaporation to phase explosion occurs above this threshold laser fluence.

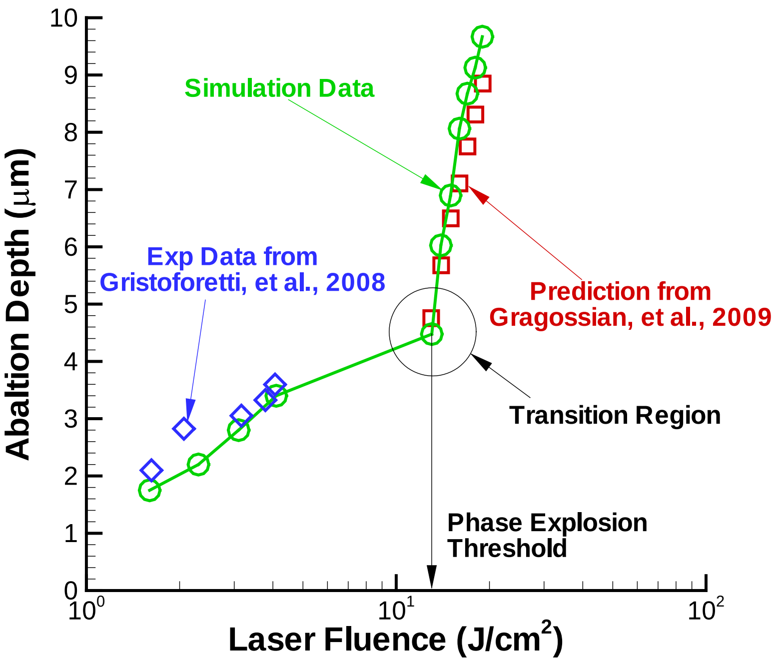

Figure 2.5. Comparison of ablation depths of aluminum under different laser fluence (Case 4: laser pulse duration 10.0 ns, wavelength 1064 nm, beam diameter 100.0 μm, Gaussian beam, single shot ablation, experimental data from Gristoforetti et al., 2008 and prediction at high fluence range from Gragossian et al., 2009).

The dependence of ablation depth on the laser pulse duration is then investigated. In case 5, the laser beam diameter is around 100 μm. The laser beam wavelength is 1064 nm and the laser pulse duration changes from 5.0 to 35.0 ns. The laser fluence is first fixed at 15.0 J/cm^2. The ablation depth under different laser pulse duration is shown in Figure 2.6. Almost same ablation depths are obtained for laser pulses with different duration, which indicates that the ablation depth is nearly independent of the laser pulse duration with fixed laser fluence. Similar findings (Laville et al., 2002; Colina et al., 2011) have been reported for nanosecond laser ablation on aluminum and other materials. Next the power density is fixed at 1.0 GW/cm^2 and the laser fluence is varied from 5.0 to 35.0 J/cm^2 corresponding to the pulse duration. The ablation depth under different laser pulse duration is then plotted in Figure 2.6. A clear increase pattern can be seen in this case with fixed power density, which indicates that the ablation depth depends strongly on the laser fluence when other laser parameters (for example, laser wavelength, laser beam diameter, etc) are kept fixed.

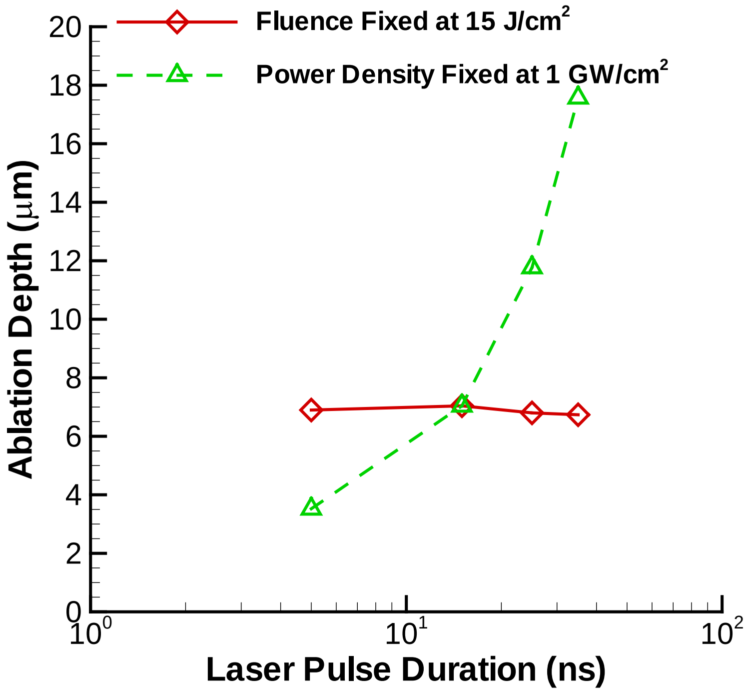

Figure 2.6. Ablation depth dependence on laser pulse duration (Case 5: laser wavelength 1064 nm, beam diameter 100.0 μm, Gaussian beam, single shot ablation).

It should be noted that the case with a fluence of 5.0 J/cm^2 (pulse duration 5 ns) in Figure 2.6 is still in the evaporation domain. Therefore, the ablation rate increases sharply after 15 J/cm^2 (pulse duration 15 ns), which again indicates the occurrence of phase explosion.

The dependence of ablation depth on the laser wavelength is also investigated. In case 6, the laser beam diameter is around 100 μm and the laser pulse duration is 10 ns. The laser wavelengths investigated here are 266, 355, 532, and 1064 nm. The laser fluence is fixed at 15.0 J/cm^2 or 5.0 J/cm^2. The dependence of ablation depth on the laser wavelength is shown in Figure 2.7. Under laser fluence of 15.0 J/cm^2, where phase explosion will dominate, the ablation depth decreases from around 9.3 μm at 266 nm to around 6.8 μm at 1064 nm monotonically. When the laser fluence is fixed at 5.0 J/cm^2, where the evaporation will dominate, the ablation depth decreases from around 4.3 μm at 266 nm to around 3.7 μm at 1064 nm. However, the decrease in this case is not as steep as in the case with higher fluence due to the fact that the absorption coefficient is relatively close under different laser wavelength at the evaporation temperature (Ehrenreigh et al., 1963).

To explain the ablation behavior of aluminum at high laser fluence shown in Figure 2.7, the absorption coefficient of aluminum under different wavelength near the critical point is calculated with Drude model (Wu and Shin, 2006a). At critical state, the density of aluminum is around 300 Kg/m^3 (Wu and Shin, 2006a). The absorption coefficients of aluminum near the critical state are shown in Figure 2.8. Clearly, the absorption coefficient is the highest at 266 nm among the four wavelengths at all temperatures investigated here. Also, the absorption coefficient decreases with the increase of laser wavelength. This is a clear indication that the largest ablation depth at 266 nm is mainly because the absorption coefficient is the largest at this wavelength. Due to the better laser absorption in the UV region, more laser energy is absorbed by the target material and more material is ablated at 266 nm.

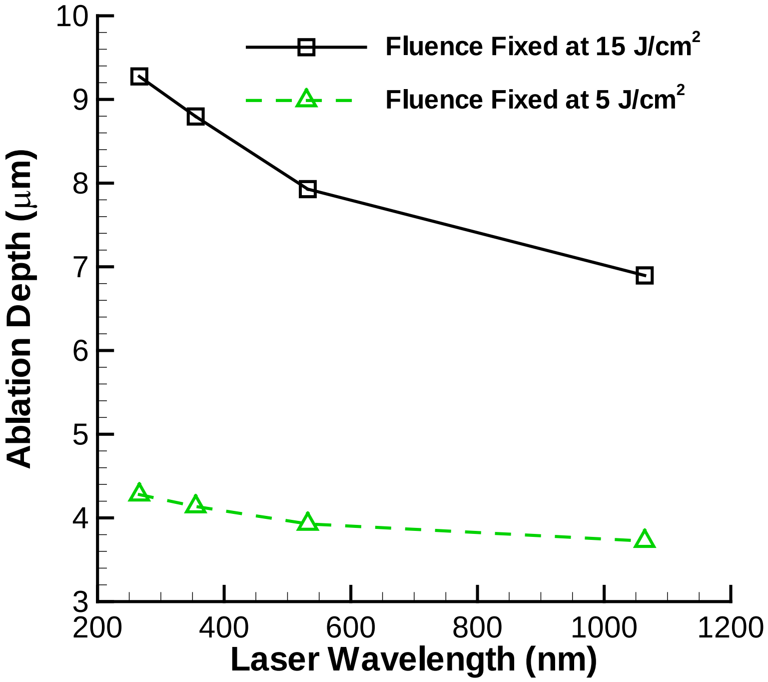

Figure 2.7. Dependence of ablation depth on the laser wavelength (Case 6: laser pulse duration 10 ns, beam diameter 100.0 μm, laser fluence fixed at 15 J/cm^2, Gaussian beam, single shot ablation).

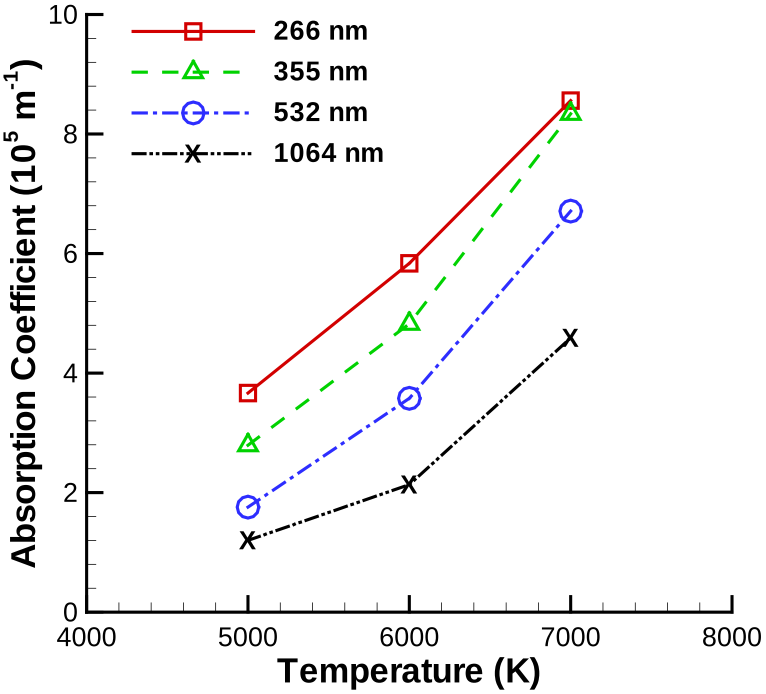

Figure 2.8. Absorption coefficient of aluminum under different laser wavelength at three different temperatures calculated from Drude model (ϱ = 300 Kg/m^3).

It is well known that the absorption of aluminum is enhanced at 800 nm and the laser beam can couple with the material more effectively at room temperature. The enhanced absorption is due to an interband contribution to the dielectric function of the material around 800 nm (Ehrenreigh et al., 1963). However, recent ab-initio calculations (Benedict et al., 2005; Ogitsu et al., 2009) revealed that the peak value of absorption around 800 nm disappeared if the temperature exceeds the melting point (950 K). As a result, the absorption coefficient of aluminum should decrease monotonically with the laser wavelength at the evaporation temperature (2793 K) and critical temperature (5410 K) as seen in Figure 2.8.

Laser ablation experiments with higher laser fluence were conducted to obtain the laser ablation crater profile in air. The target material is aluminum, which was carefully polished before the experiments. The laser beam wavelength is 1064 nm and the beam diameter is around 1.0 mm. The comparison of the predicted and experimentally measured crater profiles under laser fluence of 24.0 J/cm^2 is shown in Figure 2.9 for case 7. The experimental crater profile is measured with an optical 3D surface profilometer (KLA-Tencor, MicroXAM-100), which has a good resolution in depth measurement (in nm level). In the laser ablation experiment, the energy loss due to the optics absorption is around 3%, which is taken into account in the code. The only other possible source for measurement uncertainty is the laser beam diameter, which is measured by a laser beam profiler (Spiricon LW130). The measurement error for laser beam diameter is estimated to be less than 5%. It can be seen from Figure 2.9 that the simulated crater profile is relatively close to the experimentally obtained one according to the above analysis of measurement uncertainties.

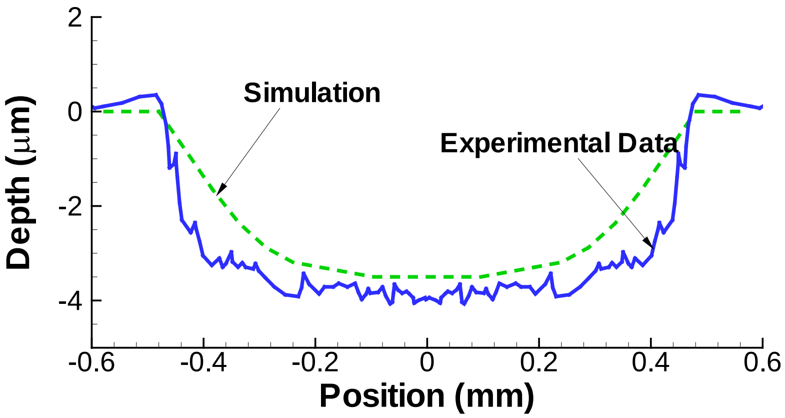

Figure 2.9. Comparison of crater profile from simulation and experiment after a single laser shot in air (Case 7: laser pulse duration 6 ns, wavelength 1064 nm, beam diameter 1.0 mm, laser fluence 24.0 J/cm^2, top-hat beam profile).

2.3.3 Laser Ablation of Aluminum in Water

A very limited amount of data has been reported in the literature on the laser ablation of aluminum in water in the high laser fluence range. Therefore, some experiments were conducted to obtain crater depths under different laser fluences. Figure 2.10 shows the crater profile obtained after single shot laser ablation in water with the previously mentioned optical surface profilometer. The laser fluence used in the experiment is from 10 to 50 J/cm^2. It can be seen that very smooth crater was generated after laser ablation. The maximum crater depth is around 8.0 μm for the laser fluence of 24 J/cm^2.

The laser ablation depth was calculated by the 2D hydrodynamics code. The contribution from shock compression cannot be neglected due to the long pulse and the high magnitude of the pressure wave (several GPa) generated during laser ablation in water. Therefore, the indentation depth generated by shock compression is also calculated using a previously-developed FEM model (Cao et al., 2010). The indentation depth increases from around 2.5 μm in the case of 12.0 J/cm^2 to around 6.0 μm in the case of 42.0 J/cm^2, as shown in Figure 2.11.

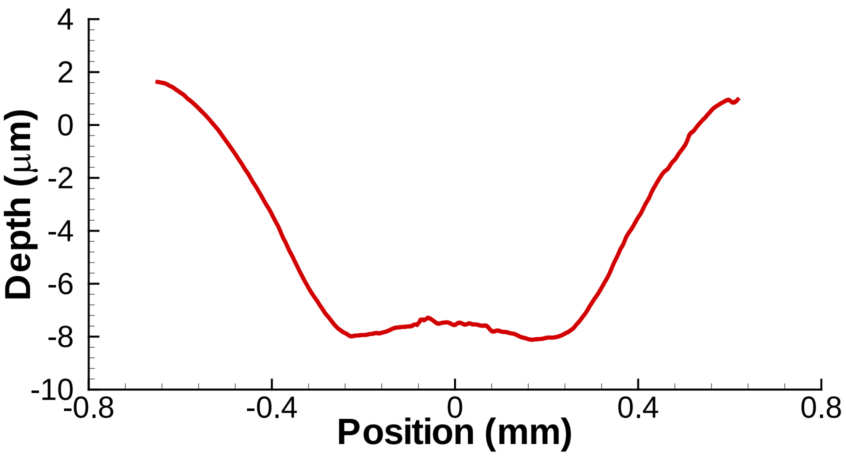

Figure 2.10. Crater profile after a single shot laser ablation in water (laser pulse duration 6 ns, wavelength 1064 nm, beam diameter 1.0 mm, laser fluence 24.0 J/cm^2, top-hat beam profile).

To show the combining effect of laser ablation and shock compression, the total crater depth is plotted with the experimental data in Figure 2.12 for case 8. Clearly, the combined depth shows a better agreement with the experimental data, which indicates that the shock compression effect is very important in the case of laser ablation in water. This combined effects account for a deeper crater depth in water than in air, as reported in literature (Kang et al., 2008; Mahdieh et al., 2010; Kim and Lee, 2001; Dupont et al., 1995; Kang et al., 2006). The crater profile of the laser ablation in water is also calculated and compared with the experimentally obtained profile. Figure 2.13 shows the comparison of the prediction with the experimentally obtained crater profile. Clearly, much better agreement can be observed with the consideration of shock compression effect.

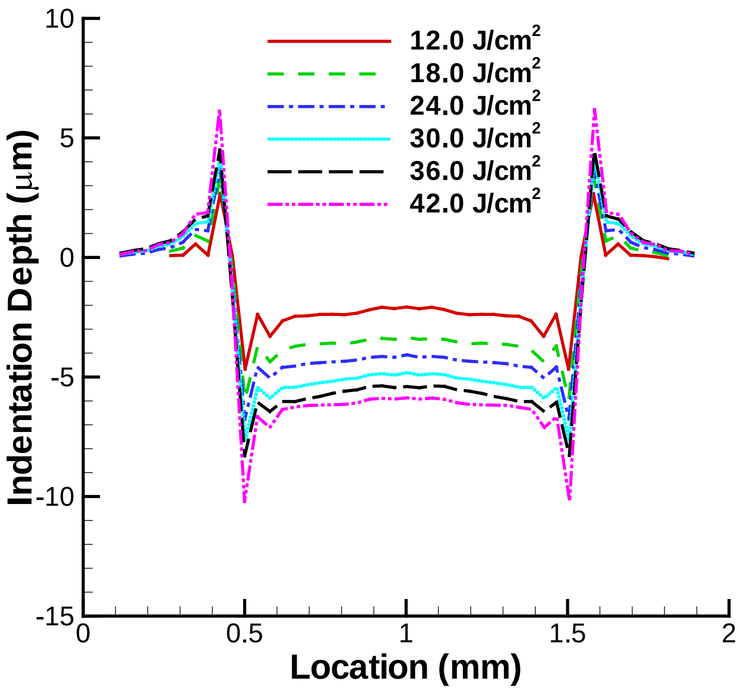

Figure 2.11. Indentation depth from shock compression (laser pulse duration 6 ns, wavelength 1064 nm, beam diameter 1.0 mm, top-hat beam profile, single shot laser ablation).

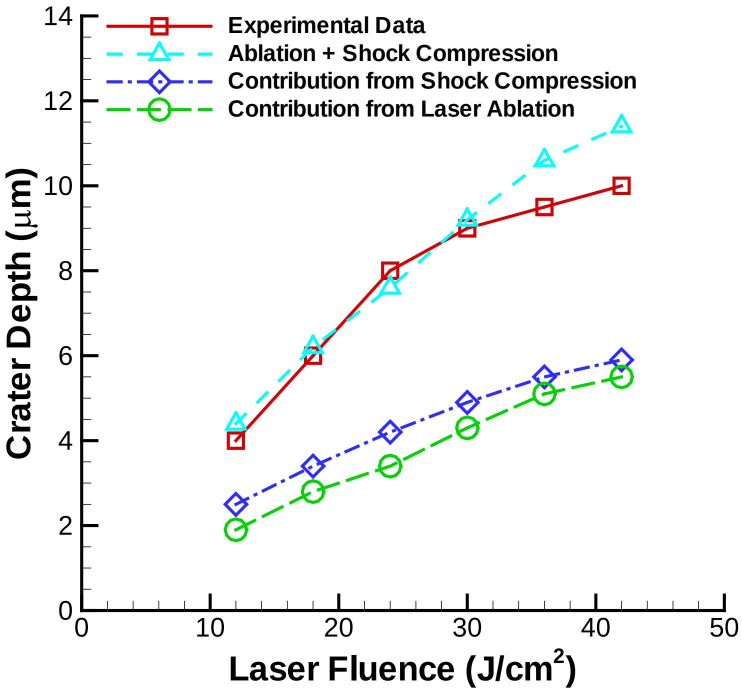

Figure 2.12. Crater depth under different laser fluence in water with contribution from laser ablation and shock compression (Case 8: laser pulse duration 6.0 ns, wavelength 1064 nm, beam diameter1.0 mm, top-hat beam, single shot laser ablation).

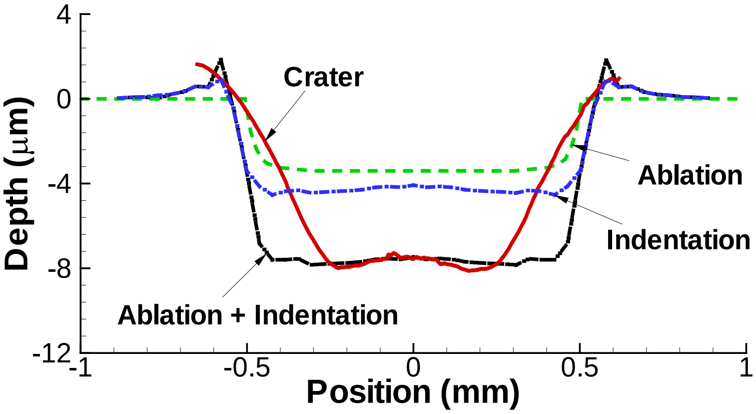

Figure 2.13. Crater profile and indentation, ablation profile after a single laser shot in water (laser pulse duration 6 ns, wavelength 1064 nm, beam diameter 1.0 mm, laser fluence 24.0 J/cm^2, top-hat beam profile).

The effect of shock compression in air is also investigated. Figure 2.14 shows the plasma pressure generated in the laser ablation in air and water. The maximum magnitude of the shock wave pressure in air is around 1.6 MPa as shown in Figure 2.14, which is far less than the plasma pressure generated in water (around 3.5 GPa) and thus will generate almost no indentation on the target surface. Therefore, the shock compression effect can be neglected in the case of laser ablation in air.

2.4 Summary

Nanosecond laser ablation of aluminum in air and water was investigated through a self-contained hydrodynamic model under different laser fluences involving no phase explosion and phase explosion. The predicted ablation depths agreed well with the literature data and experiments. A sharp increase in ablation rate is observed for nanosecond laser ablation of aluminum at around 10 J/cm^2 with the occurrence of phase explosion for a 1064 nm, 10 ns laser pulse. The ablation depth is found to be nearly independent of the laser pulse duration, while it decreases with the increase of laser wavelength. Deeper crater depths in water found in all the conditions studied in this work are due to the high-magnitude shock compression.

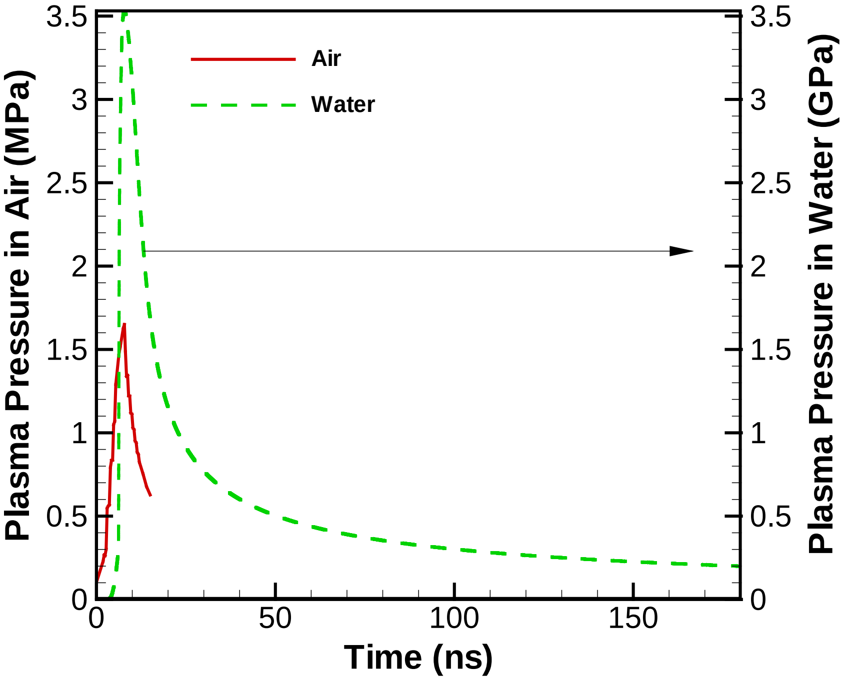

Figure 2.14. Plasma pressure generated in the laser ablation in air and water (laser pulse duration 6 ns, wavelength 1064 nm, beam diameter 1.0 mm, laser fluence 42.0 J/cm^2, top-hat beam profile, single shot laser ablation).

CHAPTER 3. MULTI-SCALE MODELING OF MELT EJECTION IN PHASE EXPLOSION

3.1 Introduction

As reviewed in Chapter 1, it still remains a difficult challenge to capture the ejected droplets during the material removal by conventional modeling methods (for example, HD model). To correctly model the laser ablation process with high laser intensity, particle formation inside the melt pool is simulated by a molecular dynamics model, and the particle movement and the further ejection are described by a smoothed particle hydrodynamic (SPH) model, while all the other parts of the target are modeled by hydrodynamics (HD) equations. Such a coupled HD-MD-SPH model is proposed in this work.

3.2 Numerical Model

A multi-scale model has been developed in this work to tackle the challenges presented earlier. In the initial stage of the laser ablation process, no particle is formed. Therefore the whole domain is described by the HD model. Then in the later stage, some particles will be generated inside the melt pool and the expanding vapor due to either evaporation, condensation (smaller particles condense onto the larger particles), collision between particles, or hydrodynamic sputtering (large particles). At this point, two calculation domains are formed. One is the particle domain (SPH domain) and the other is the HD domain. To obtain the initial particle distribution for the SPH calculation, MD simulation is employed from the beginning of the laser-matter interaction. The HD calculation is based on the model developed earlier in the authors' group (Wu and Shin, 2007b), while the MD/SPH calculation is conducted with the LAMMPS package (lammps.sandia.gov; Ganzenmuller et al., 2011).

Figure 3.1 shows the relative position of the MD domain in the multi-scale model, which is right under the laser beam and taken directly from the HD domain. The left and right sides of the MD domain are set with periodic boundary conditions. Figure 3.2 shows the calculation flow chart for the coupled model. Clearly, the pressure, temperature, and velocity of the interface cells in HD domain need to be passed to SPH domain. In Figure 3.2, the heat flux (q") at the interface is calculated based on the temperature gradient at the boundary in MD/SPH domain. The force at the interface is calculated based on the pressure gradient at the boundary in HD domain. The mass transfer rate m' is calculated from the mass conservation equation at the interface region.

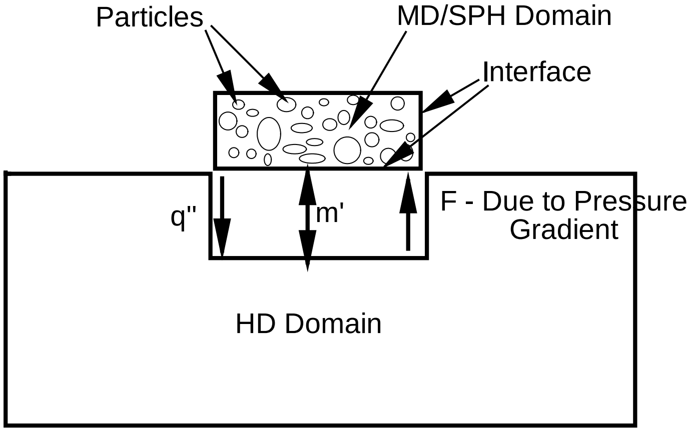

Figure 3.1. Calculation domain for multi-scale model.

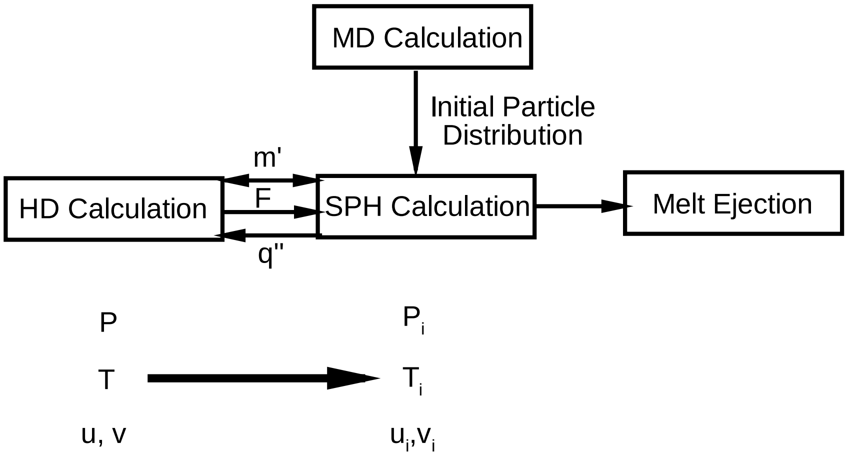

Figure 3.2. Calculation flow chart for multi-scale model.

In the nanosecond laser ablation process, the laser beam diameter is usually in the range of 100 μm to 10 mm, which is much larger than the normal MD simulation size. To consider a larger non-uniform beam used in the experiment as shown in Figure 3.1, multiple representative MD cells are taken from the target surface based on the laser intensity distribution to obtain a more accurate initial particle distribution from MD calculation, as seen in Figure 3.3. Based on the given beam profile, multiple calculations with different laser fluences are conducted to obtain the particle distribution.

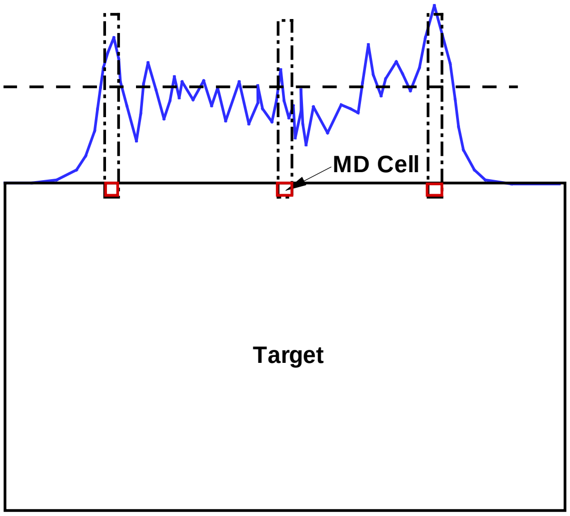

Figure 3.3. Laser beam distribution and MD cells.

In the MD calculation, the atom number is about 12.5 million in the initial computation domain of 20 nm × 20 nm × 32 μm. The dimension of the domain is chosen with the consideration of the ablation depth of metal targets (around 5.0 μm, Cao et al., 2013) and the plume expansion. The interaction between the atoms of the system was governed by the modified embedded atom method (MEAM) potential (Baskes, 1992), which has been widely used in the MD simulation for face centered cubic (fcc) metal targets, such as aluminum, copper, silver, etc. In the MEAM formulation, the total energy E of a system of atoms is given by (Baskes, 1992)

$$E = \sum_i \left\{ F_i(\rho_i) + \frac{1}{2} \sum_{i \neq j} \emptyset_{ij}(r_{ij}) \right\} \tag{2}$$

where *F* is the embedding energy which is a function of the atom electron density ϱ, and ϕ is a pair potential interaction. The pair interaction is summed over all neighbors *j* of atom *i* within the cutoff distance. MEAM potential is applied in this calculation and the parameters for both aluminum and copper are taken from Baskes' work (1992).

The instability of the liquid between the binodal and spinodal line is considered by addressing the density/thermal fluctuations for the atoms in the surface region (Linhart et al., 2005). If the liquid is in the superheated state (between the binodal and spinodal) and close to the binodal line, the density fluctuation could push the liquid phase to the spinodal line or pull back to the binodal line. With the increase of superheating, the free energy barrier separating the liquid and vapor states becomes lower. Under this condition, the thermal fluctuation could easily cross the barrier and facilitate the phase separation. This will be further analyzed in the thermodynamic trajectory later in the results section.

Figure 3.4 shows the atom distribution at different time for the laser fluence of 12 J/cm^2. The initial solid target is located at the bottom half (z <= 15 μm) of the calculation domain. With the laser energy coming from the top, the surface region is melted and the atoms begin to move upwards. Also some large clusters of atoms are formed in the region of 8 to 16 μm. Figure 3.5 shows the atom distribution prediction at t = 60 ns from MD simulation under different laser fluences. Clearly with different laser energy input, different numbers of clusters are formed with different size.

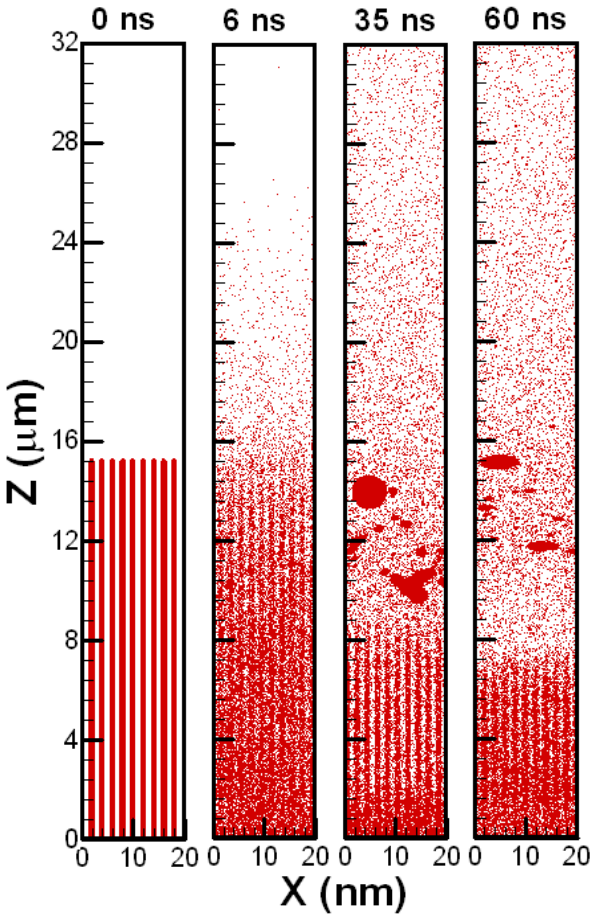

Figure 3.4. Atom distribution at different time (laser fluence 12 J/cm^2, wavelength 1064 nm, pulse duration 6 ns).

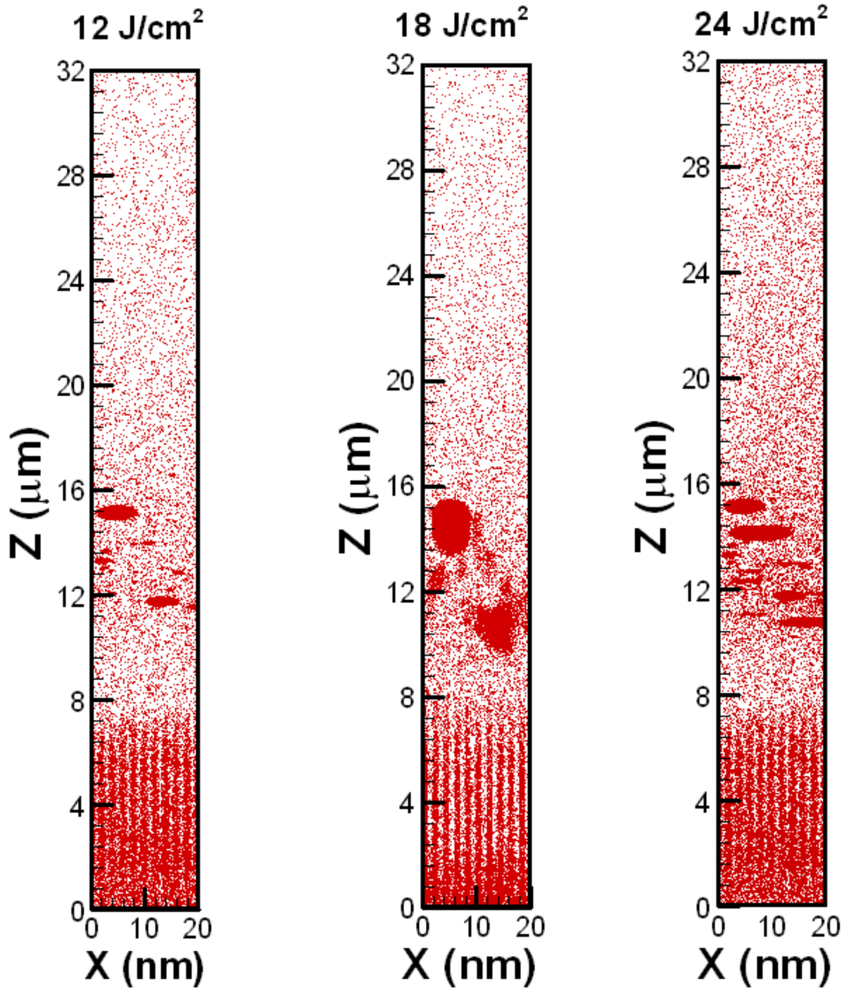

Figure 3.5. Atom distribution at t = 60 ns from MD simulation under different laser fluences.

The initial atom distributions obtained from MD simulation can be combined according to the beam profile to get an atom distribution in a larger domain size using the periodic boundary assumption. By combining the MD simulation results, one can obtain the initial SPH particles distribution, as shown in Figure 3.6. In this step, the initial SPH particles are assumed to be in the spherical shape. The location of the SPH particles in each large cell is determined by the initial atom positions and the mass distribution in the large cell. The temperature and velocity information of all the atoms can also be transferred to the corresponding SPH particles using the same method.

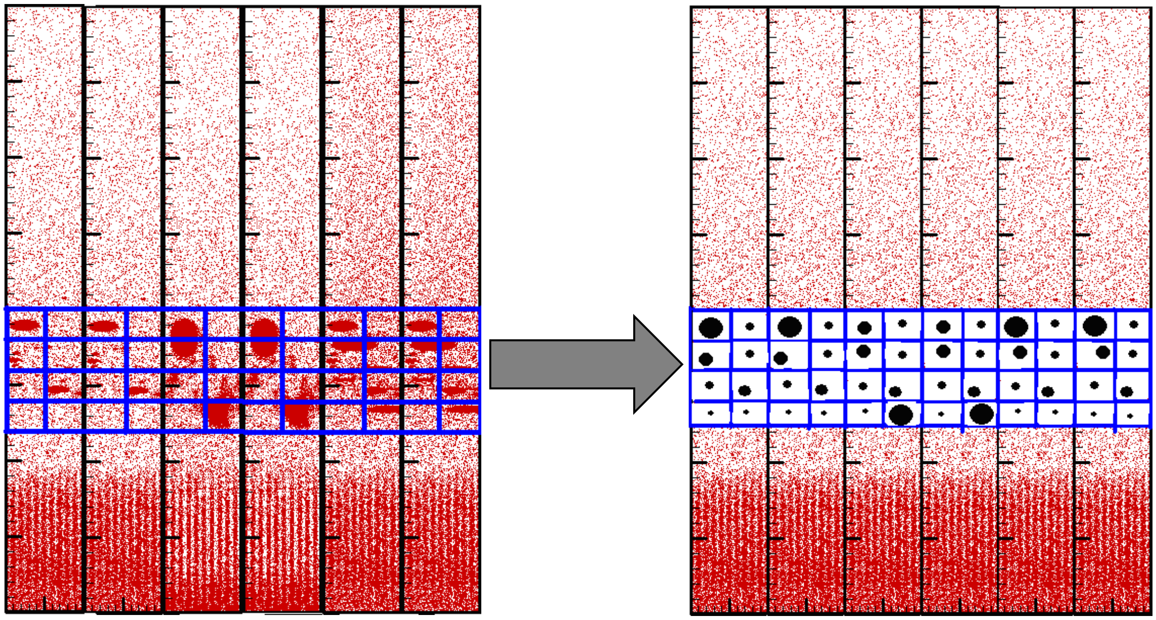

Figure 3.6. Mapping of particles predicted by MD to SPH particles.

The SPH calculation then starts with the input from MD model. Figure 3.7 shows the initial configuration of SPH calculation. The close-up view shows the particle distribution from the MD calculation, where particles are formed with different sizes. The bottom of the whole calculation domain is set to be stationary in the SPH calculation. With the above procedure, the SPH model should be able to calculate the temperature evolution inside the molten pool, the large particle movement, and eventually the melt ejection.

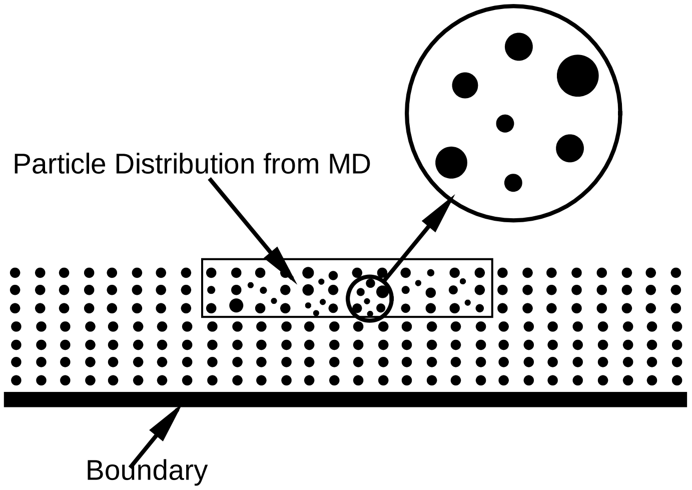

Figure 3.7. Initial configuration of SPH calculation.

3.3 Experimental Setup and Procedures

A probe beam-pump beam technique is used in this work to observe the phase explosion. Figure 3.8 shows the experimental setup. The pump beam is produced by the Nd-YAG nanosecond laser (Continuum Surelite) operating at 1064 nm with a pulse duration of 6 ns. The Nd-YVO_4 picosecond laser (Lumera Rapid) is used to provide the green probe beam (532 nm, a pulse duration of 10 ps). Two photo detectors (with photodiode inside, ThorLabs, DET200) are used in the experimental setup to synchronize the probe beam (ps laser) and pump beam (ns laser). To control the exposure time accurately and obtain the images at different time, the CCD camera (Imaging Source, DFK 42BUC03) needs to be externally triggered and synchronized to work with the probe beam/pump beam together.

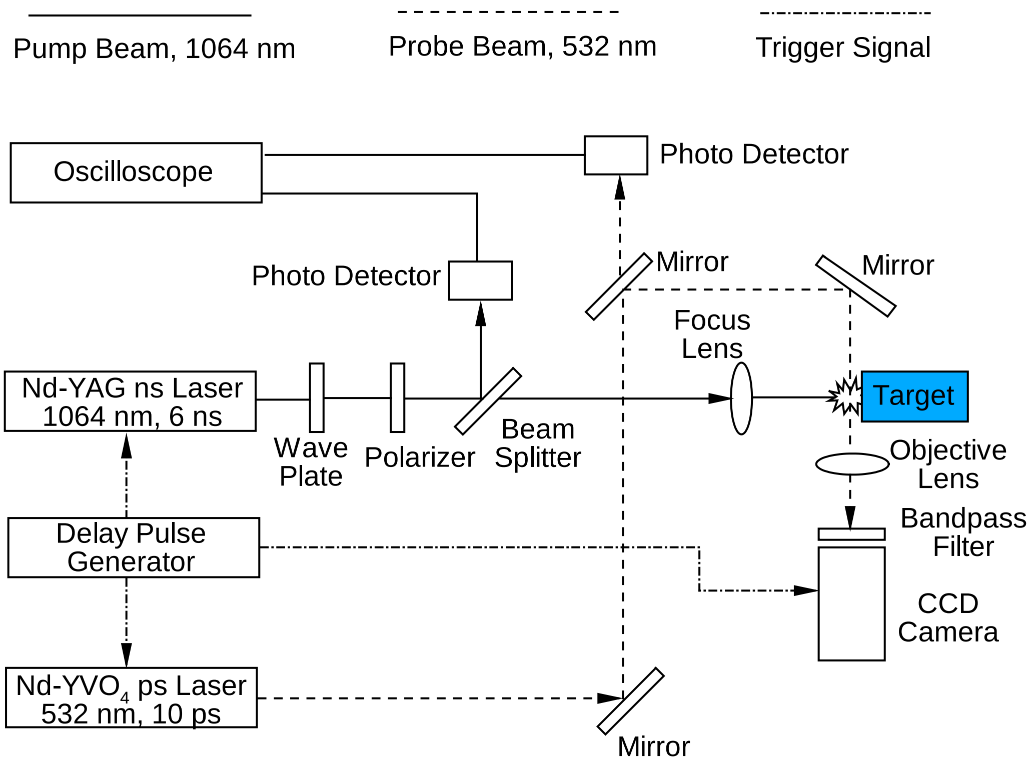

Figure 3.8. Schematic drawing of the experimental setup.

The probe beam laser, the pump beam laser, and the CCD camera are triggered externally by the delay pulse generator (BNC 555). The time sequence of the triggering signals is shown in Figure 3.9. For the ps laser, the 1120 ns is the default delay time before a laser pulse could be generated when a trigger signal is sent to the laser. Similarly, 137 μs and 240.1 μs are the default delay time for the CCD camera and the ns laser, respectively. To precisely determine when the CCD images are taken, the ps laser and ns are synchronized first and then the CCD camera is added later. It should be noted that the delay time between the trigger signals are carefully controlled to make sure that the probe ps beam illuminates the ns laser ablation site during the CCD exposure period. To eliminate the effect of background light, the experiments are conducted in a dark environment. By changing the delay time between the nanosecond laser pulse and the picosecond laser, one can capture the images at different time instants after the nanosecond laser pulse irradiates the target surface.

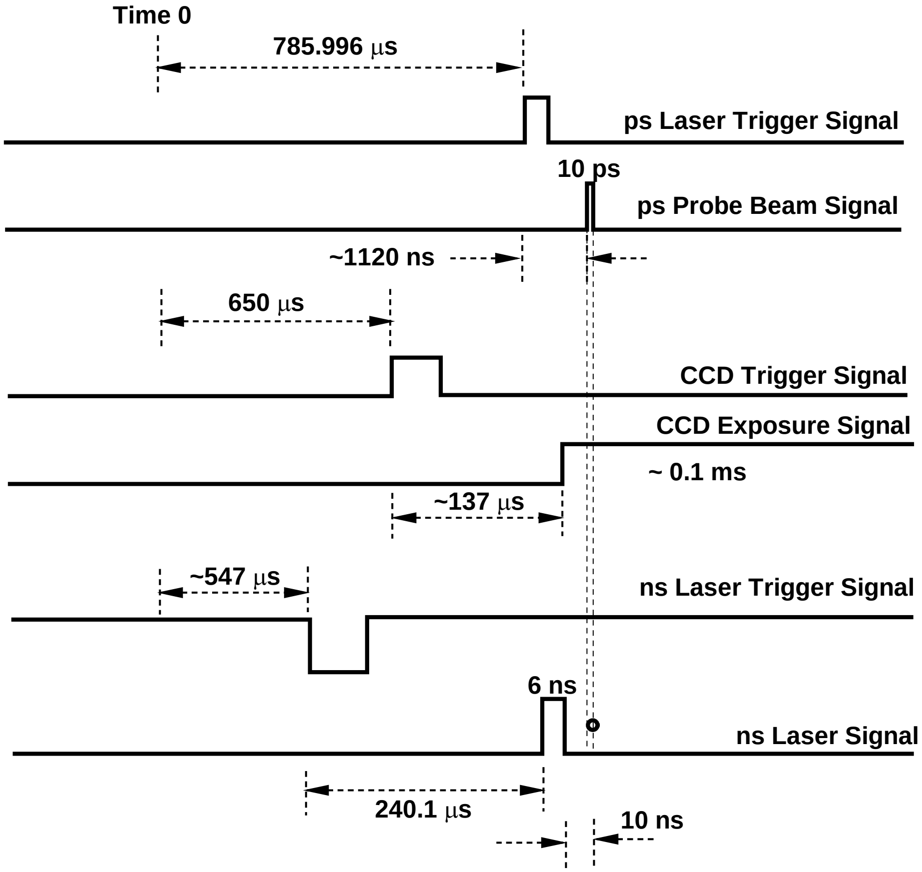

Figure 3.9. Time sequence of triggering signals.

3.4 Results and Discussion

3.4.1 Laser Ablation of Aluminum

To compare the experiment results with the simulation data, the MD/SPH simulation of the laser ablation process was conducted under the same condition. The melt ejection could be calculated using the SPH model with the initial particle distribution from MD calculation.

Case A: Laser Fluence at 12 J/cm^2

The laser fluence in this case is right above the phase explosion threshold according to the previous HD calculation (Cao, Zhao, and Shin, 2013). Figure 3.10 shows the calculation results at different time instants for this case. In all the CCD images and prediction results shown in this work, time 0 is defined as the instant when the ns laser beam irradiates the target surface. Some large particles can be observed to being ejected from the melt pool at 72 ns, as seen in Figure 3.10 (b). Therefore, the starting time of melt ejection (phase explosion) is around 72 ns after the ns laser beam irradiates the target surface. The experimental results from Porneala and Willis (2006) indicated a starting time between 52 and 114 ns under the similar condition.

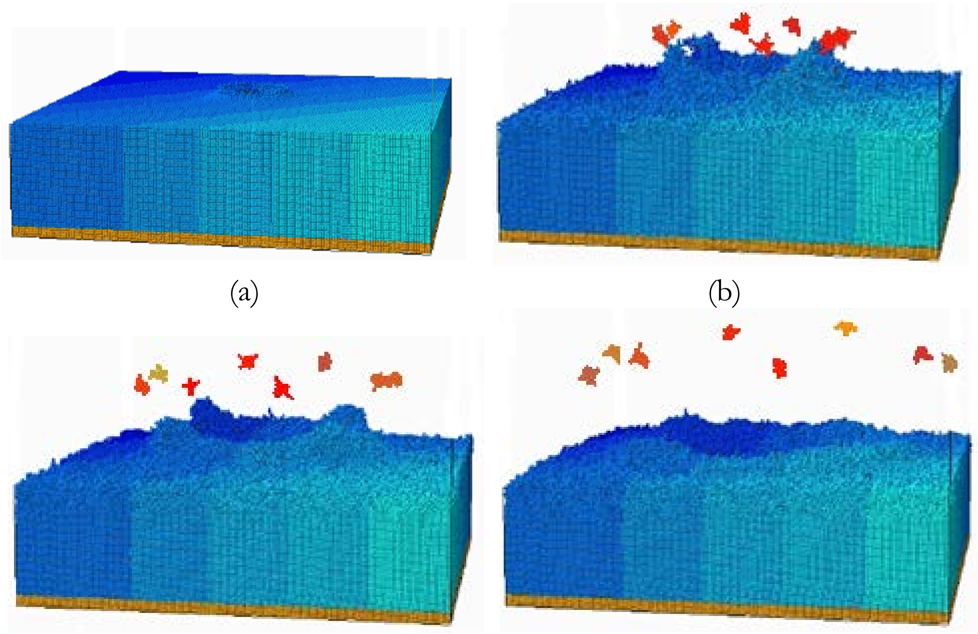
(a) (b)
(c) (d)

Figure 3.10. Modeling results of melt ejection after laser ablation (a) 66 ns (b) 72 ns (c) 78 ns (d) 84 ns (laser fluence 12 J/cm^2, pulse duration 6 ns, 1064 nm, beam diameter 200 μm).

Figure 3.11 shows the experimental observation under the same condition. In the CCD images shown, the bottom boundary is the target surface. The center region is the ns laser ablation site. The laser beam irradiates the target surface from the top of the image. At around t = 70 ns, some particles (black dots) can be observed in the bottom-center region. With the increase of time, more particles are ejected from the melt pool. The particles move vertically first and then expands in the radial direction, which is very similar to the model prediction shown in Figure 3.10. One of the possible reasons behind this particle movement behavior is that the pressure gradient inside the melt pool may have a radial component. In the later stage of the phase explosion, this component becomes significant and therefore affects the direction of the particle ejection. Further analysis about the particle size distribution at different time will be shown later.

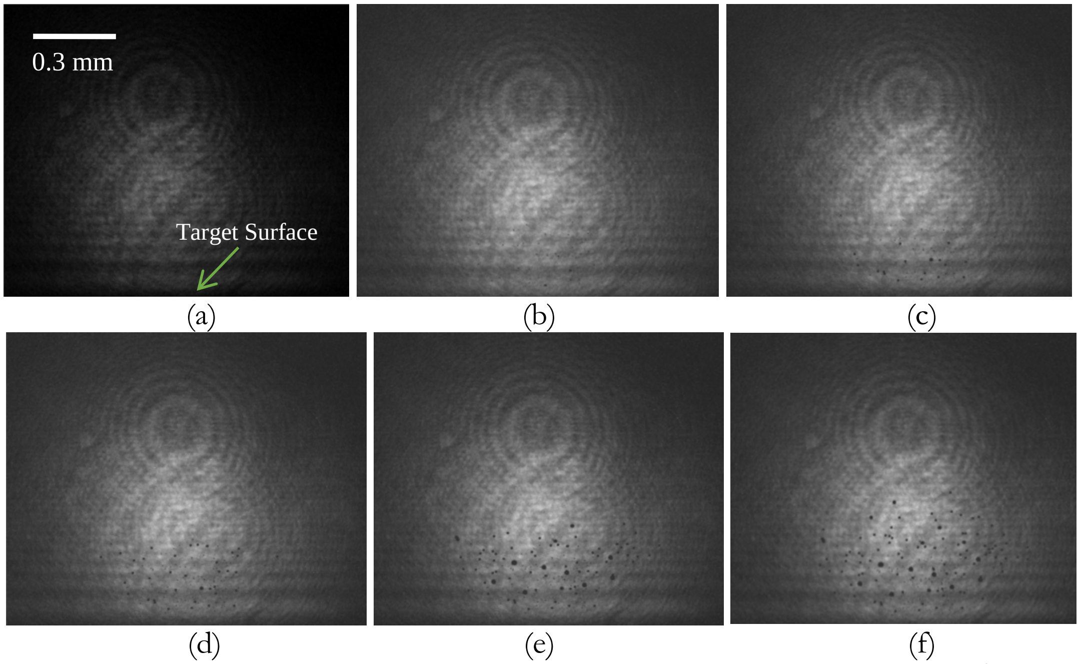

Figure 3.11. Experimental observation of melt ejection under laser fluence 12 J/cm^2 (a) 60 ns (b) 65 ns (c) 70 ns (d) 75 ns (e) 80 ns (f) 85 ns (laser beam coming from the top of the image, pulse duration 6 ns, 1064 nm, beam diameter 200 μm).

Case B: Laser Fluence at 24 J/cm^2

In this test case, the laser fluence is 24 J/cm^2. Phase explosion will occur in this case. Figure 3.12 shows the calculation results of the melt ejection from t = 66 ns to t = 84 ns. Figure 3.13 shows the experimental observation under the same condition.

Similar to the previous case, the particle ejection starts at around t = 70 ns in both the model prediction and experimental observation. Due to the higher laser fluence than that in Case A, stronger ejection can be observed at the later stage in this case. Both the model prediction and the experimental observation indicate that the particles move up first and then expand to the radial direction later. Also, the model prediction shows that more particles are ejected from the melt pool than that in the experimental observation, especially in the later stage. This observation will be further analyzed in the next section.

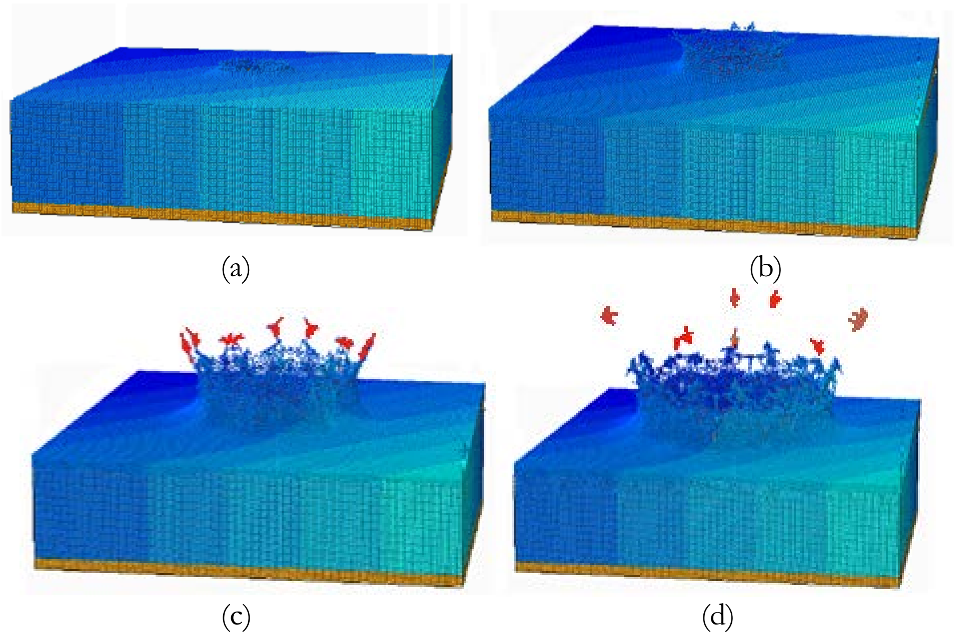
(a) (b) (c) (d)

Figure 3.12. Modeling results of melt ejection after laser ablation (a) 66 ns (b) 72 ns (c) 78 ns (d) 84 ns (laser fluence 24 J/cm^2, pulse duration 6 ns, 1064 nm, beam diameter 200 μm).

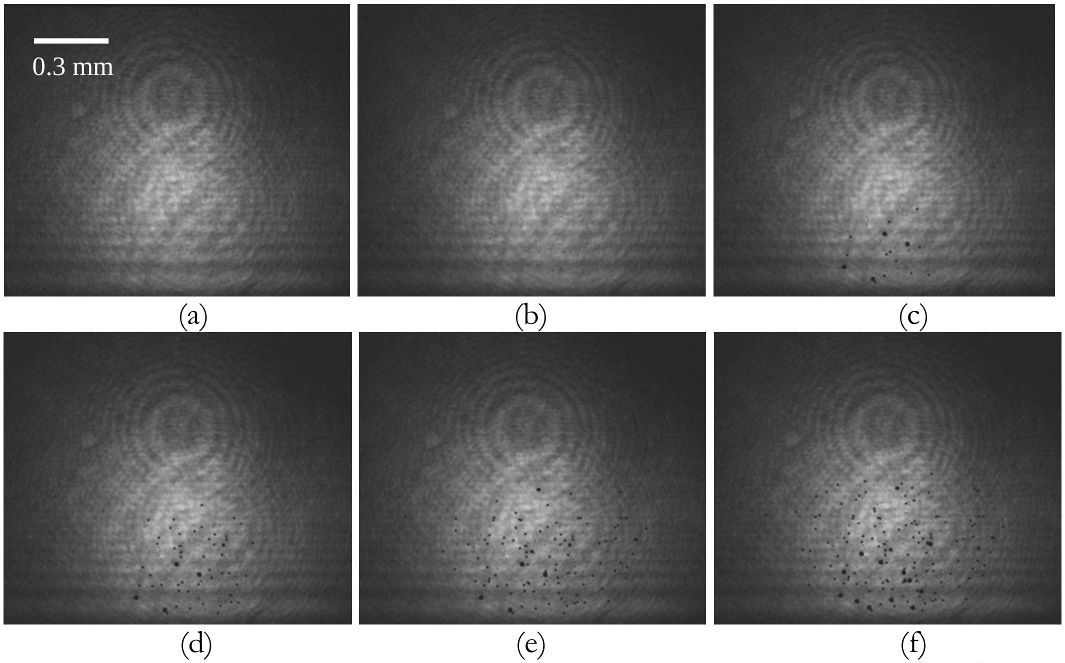

Figure 3.13. Experimental observation of melt ejection under laser fluence 24 J/cm^2 (a) 60 ns (b) 65 ns (c) 70 ns (d) 75 ns (e) 80 ns (f) 85 ns (laser beam coming from the top of the image,pulse duration 6 ns, 1064 nm, beam diameter 200 μm).

Case C: Laser Fluence at 36 J/cm^2

Figure 3.14 shows the melt ejection predicted by the SPH calculation under laser fluence of 36 J/cm^2. Figure 3.15 shows the experimental observation under the same condition. With the highest laser fluence, much stronger particle ejection can be observed in this case. The average particle size is also larger than the previous two cases. The ejection starting time is a little earlier this case, which is around t = 65 ns. The ejected particles move up first in the vertical direction and then expand to the radial direction at the later stage.

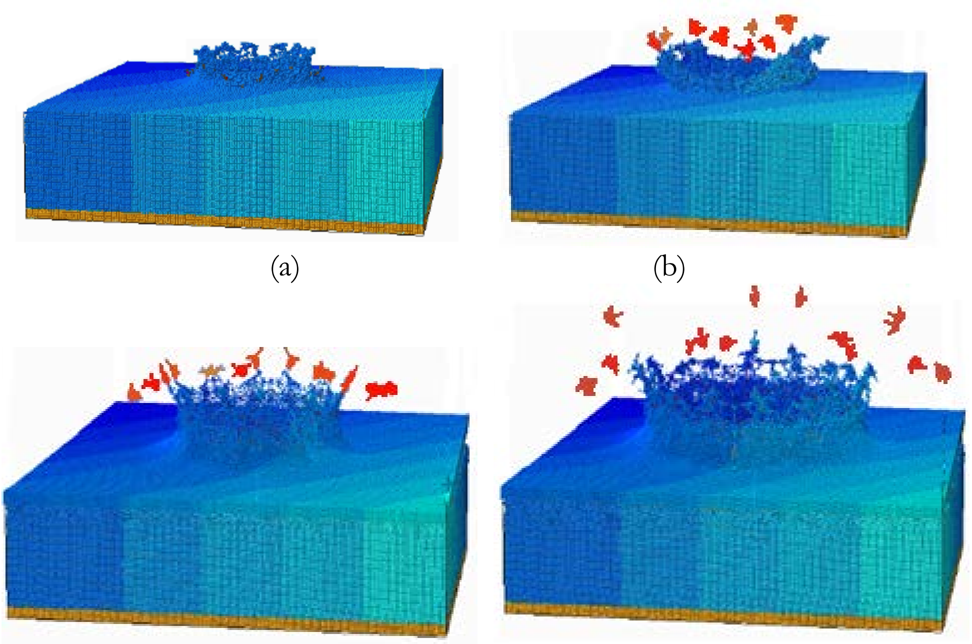
(a) (b)

(c) (d)

Figure 3.14. Modeling results of melt ejection after laser ablation (a) 66 ns (b) 72 ns (c) 78 ns (d) 84 ns (laser fluence 36 J/cm^2, pulse duration 6 ns, 1064 nm, beam diameter 200 μm).

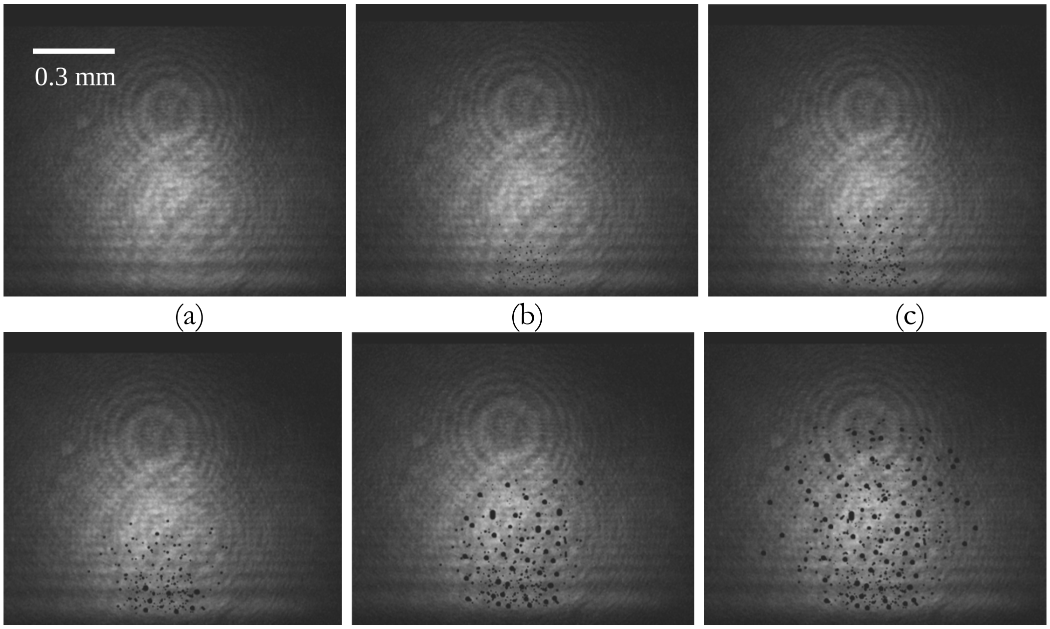

(a) (b) (c)

(d) (e) (f)

Figure 3.15. Melt ejection under laser fluence 36 J/cm^2 (a) 60 ns (b) 65 ns (c) 70 ns (d) 75 ns (e) 80 ns (f) 85 ns (laser beam coming from the top of the image,pulse duration 6 ns, 1064 nm, beam diameter 200 μm).

In all three cases, the particle movement can be clearly seen in the figures, expanding vertically first and then radially in the later stage in both simulation and experimental observation. With the increase of the laser fluence, more particles could be observed with the CCD camera and also in the simulation. The average particle size tends to be larger in the case of higher laser fluence as well, due to the stronger laser-matter interaction at the high fluence.

To quantitatively compare the simulation results with the experimental observation, the particle size distributions are extracted from both figures under the laser fluence of 36 J/cm^2. Figure 3.16 shows the comparison of particle size distributions at different time in a three-dimensional waterfall plot. It can be seen in Figure 3.16 that both the distributions show a bi-modal shape at different time, especially at the later stage. Also with the increase of the time, the particle size tends to increase in both plots. Overall the two distributions are very close.

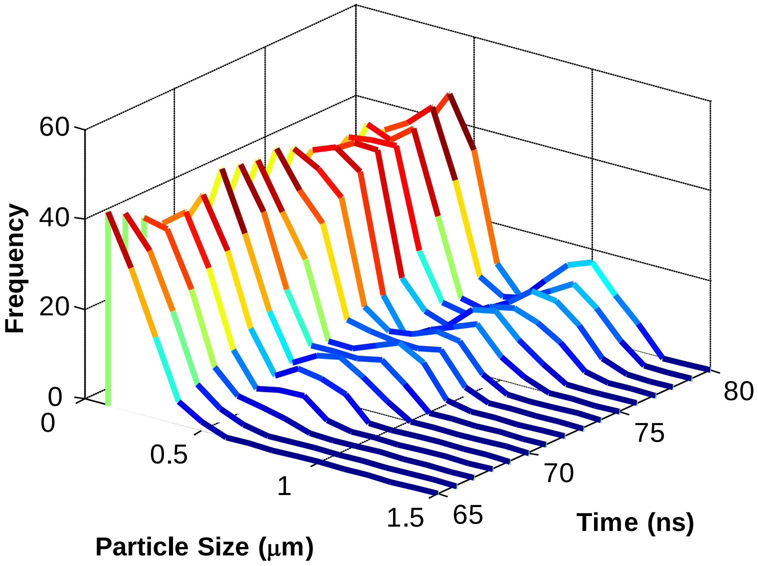

(a)

Figure 3.16. Particle distribution from (a) simulation (b) experiment and (c) mass removal at different time (laser fluence 36 J/cm^2, pulse duration 6 ns, 1064 nm, beam diameter 200 μm).

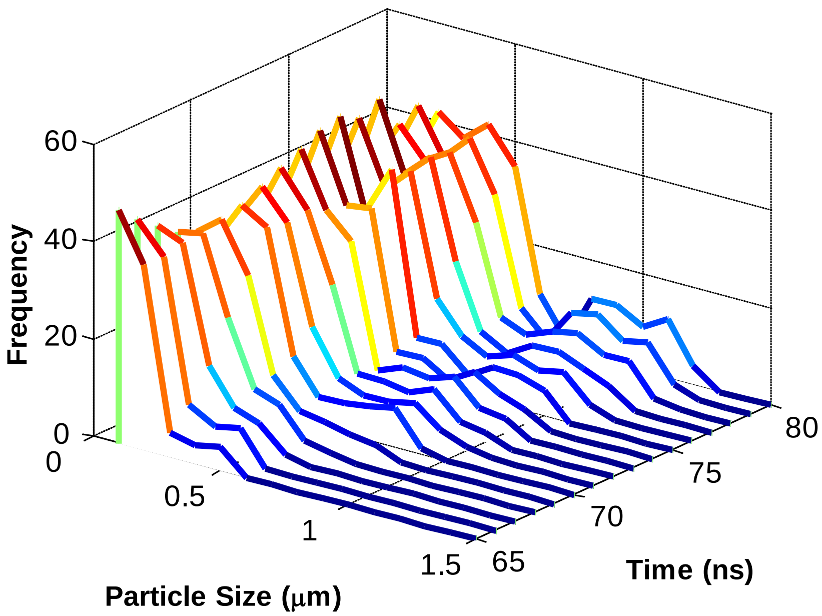

(b)

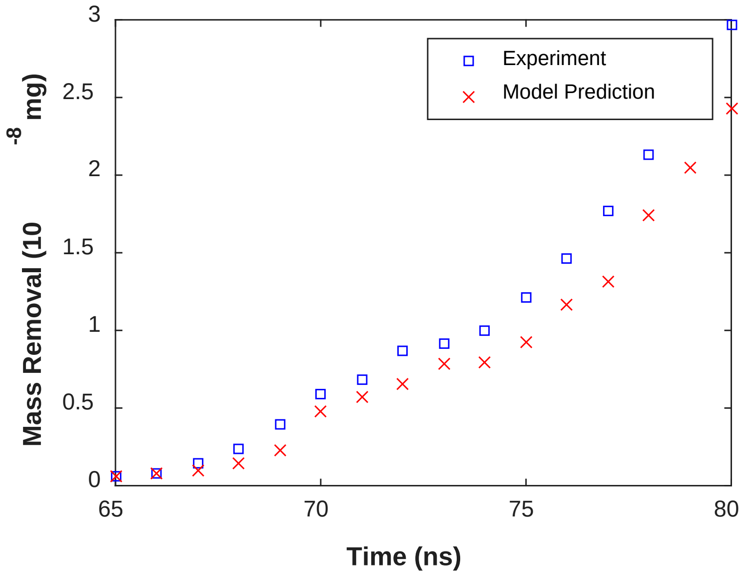

(c)

Figure 3.16. Continued.

The mass removal at different time instants is also plotted in Figure 3.16 for both experimental data and the model prediction, which clearly indicates that the mass removal rate increases rapidly in the later stage due to the presence of the larger particle.

To further understand the mechanism of the phase explosion, the temperature distribution inside the melt pool at different time is carefully investigated. Figure 3.17 shows the initial temperature and subsequent temperature distributions inside the aluminum target at different time instants. The high temperature region inside the melt pool generally propagates into the deeper region with time. The temperature information at 65 ns indicates that the temperature at the bottom of the crater (around -4 μm) is around 5500 K, which is close to the 0.9 T_c value for aluminum (around 5600 K). The prediction of the ablation depth from the HD model using the 0.9 T_c criterion is also around 4 μm. This confirms that the 0.9 T_c criterion is reasonable for predicting ablation depth with the occurrence of phase explosion in the HD calculation for aluminum.

Since the critical temperature is very important in the current work, its value is further analyzed with MD simulation following the method developed in Cheng and Xu's work (2007). By calculating multiple isotherms near the critical point, as seen in Figure 3.18, the critical temperature is predicted to be around 5950 ± 20 K, which is close to the value (6200 K) used here for aluminum. The literature reported values for the critical temperature of aluminum are in the range of 5400-9500 K (Morel et al., 2009). However, recent estimates of the value are in the low end of the range, for example, 6700 ± 800 K (Morel et al., 2009), 6300 K (Bhatt et al., 2006). Therefore the value used in this work (6200 K) is in the reasonable range.

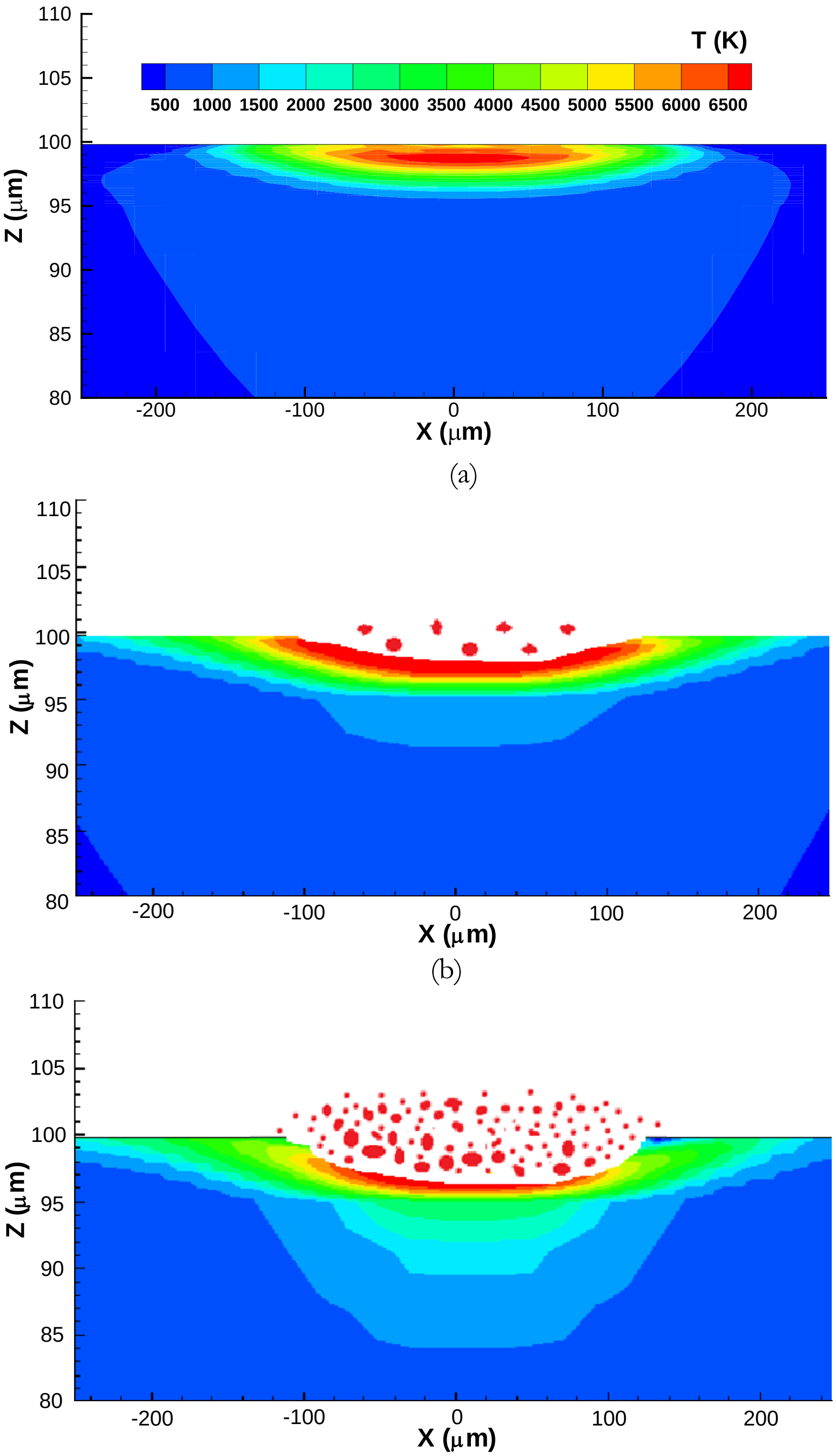

(a)

(b)

(c)

Figure 3.17. Temperature distribution inside the aluminum target at different time (a) Initial temperature distibution at t = 35 ns for SPH calcualtion (b) t = 50 ns (c) t = 65 ns (laser fluence 36 J/cm^2, pulse duration 6 ns, 1064 nm, beam diameter 200 μm).

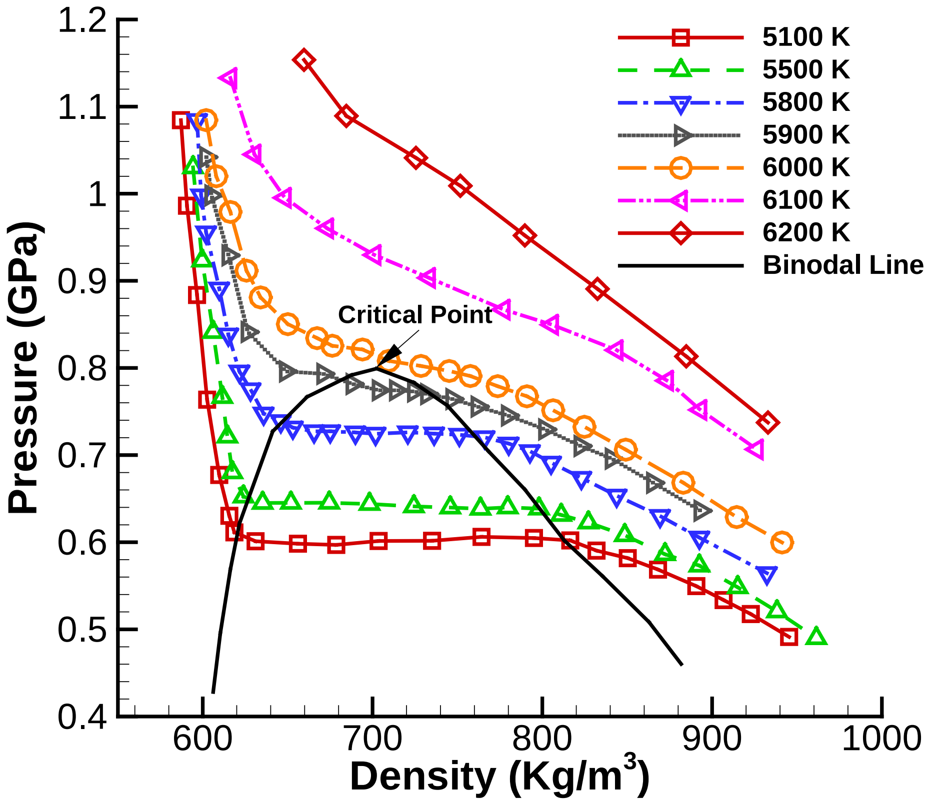

Figure 3.18. Calculated isotherms from MD simulation for aluminum near the critical point.

The thermodynamic trajectories of the different aluminum particles at different regions are further analyzed and shown in Figure 3.19. In this figure, the spinodal and binodal curves are marked as well as the super-heated liquid (SHL) region. The numbers marked along the thermodynamic trajectory are the time instants (in ns) in the calculation. Clearly, the aluminum particles at 4.0 microns below the original surface will enter the unstable zone and go through the spinodal decomposition process (Sokolowski-Tinten et al., 1998). As a result, these particles will be ejected from the melt pool, as observed in both the model prediction and experimental observation in Case C. The particles in the deeper zone will solidify back to the bulk solid state as indicated by the thermodynamic trajectories in Figure 3.19.

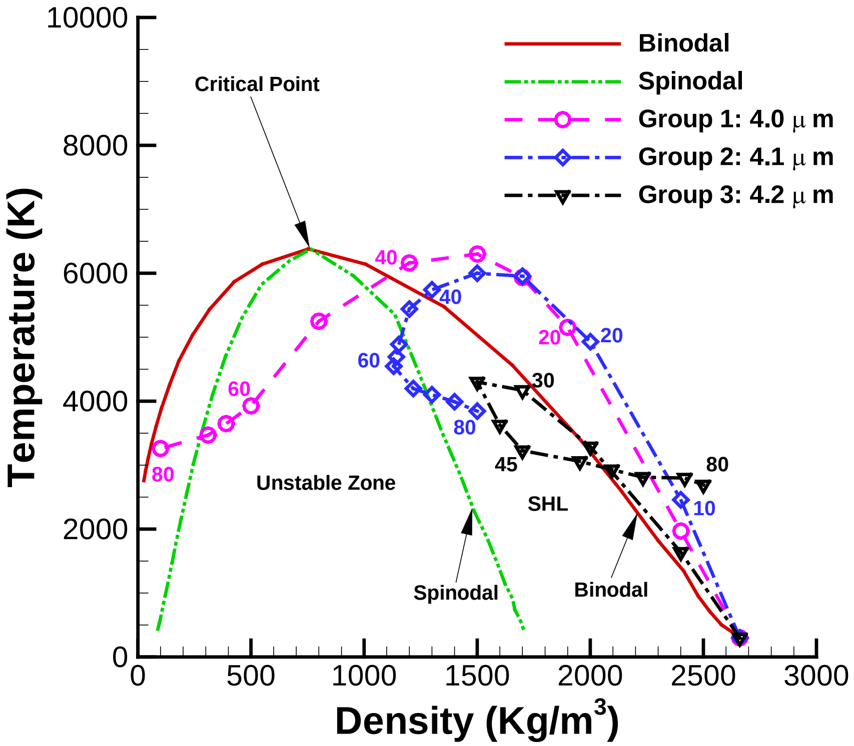

Figure 3.19. Thermodynamic trajectory of the aluminum inside the melt pool (laser fluence 36 J/cm^2, pulse duration 6 ns, 1064 nm, beam diameter 200 μm).

3.4.2 Laser Ablation of Copper

To evaluate the validity of 0.9 Tc criterion during phase explosion, laser ablation of copper is also investigated numerically with the MD/SPH model under different laser fluences and experimentally with the experimental setup shown in Figure 3.8. According to Tavassoli and Khaaji (2008) and Liu et al. (2004), phase explosion should occur when the laser fluence is greater than 30 J/cm^2 for copper for a nanosecond laser operating at 1064 nm and a pulse duration of 6 ns. In this experiment, the laser fluences are chosen to be 36 J/cm^2 or higher to make sure that the phase explosion could be observed by the CCD camera. Figure 3.20 and Figure 3.21 show the experimental observation at different delay time under laser fluence of 36 and 48 J/cm^2, respectively.

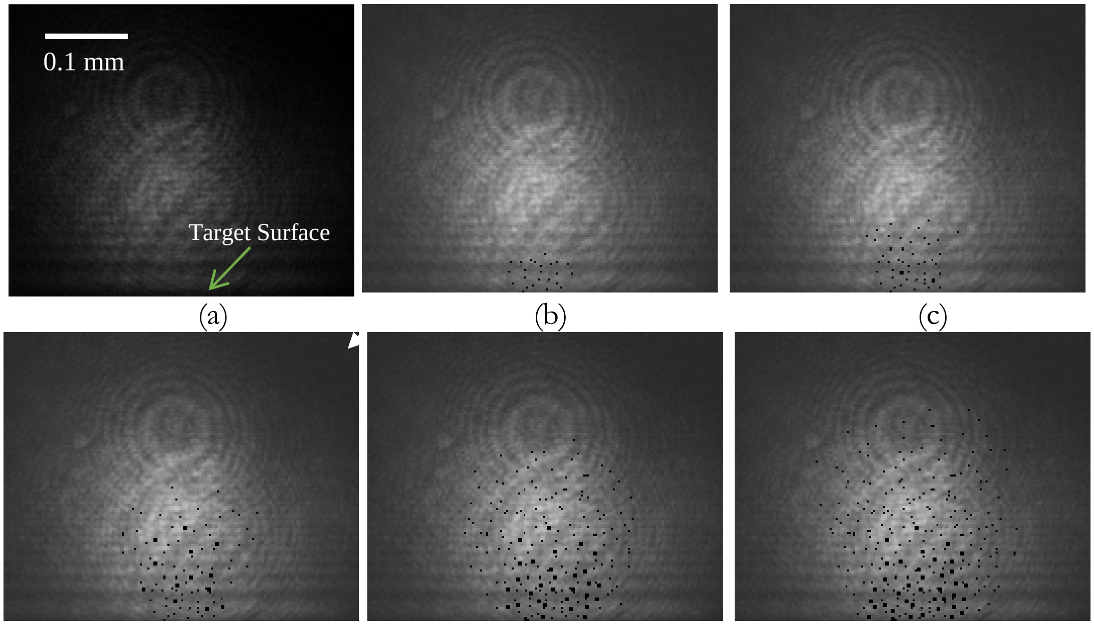

(a) (b) (c)

(d) (e) (f)

Figure 3.20. Experimental observation of melt ejection under laser fluence 36 J/cm^2 (a) t = 50 ns (b) t = 55 ns (c) t = 60 ns (d) t = 65 ns (e) t = 70 ns (f) t = 75 ns (copper target, laser beam coming from the top of the image, pulse duration 6 ns, 1064 nm, beam diameter 100 µm).

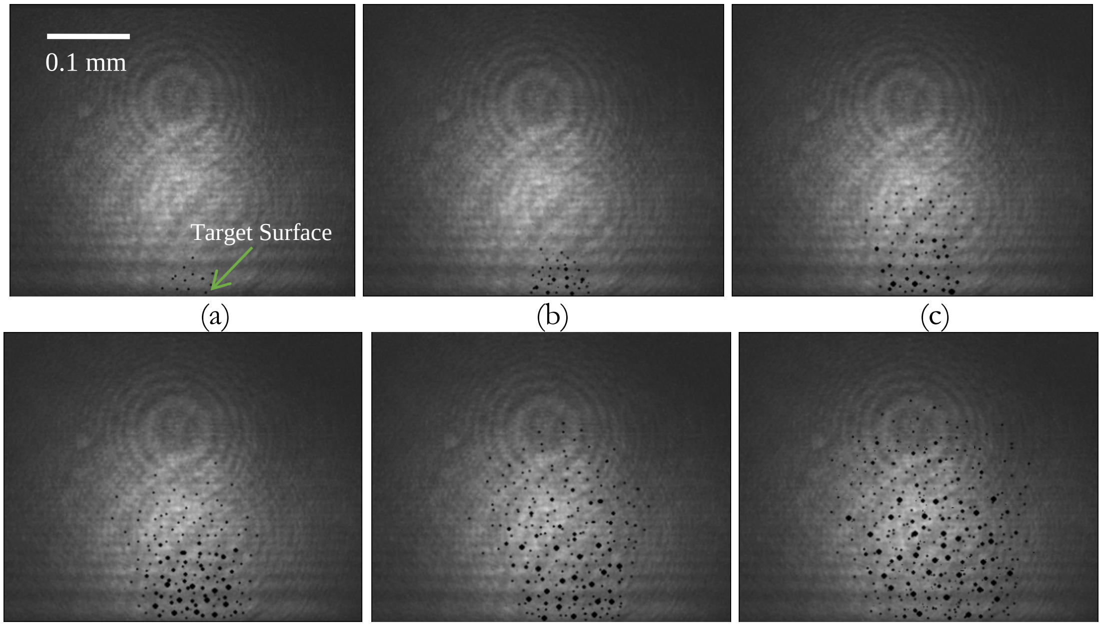

(a) (b) (c)

(d) (e) (f)

Figure 3.21. Experimental observation of melt ejection under laser fluence 48 J/cm^2 (a) t = 50 ns (b) t = 55 ns (c) t = 60 ns (d) t = 65 ns (e) t = 70 ns (f) t = 75 ns (copper target, laser beam coming from the top of the image, pulse duration 6 ns, 1064 nm, beam diameter 100 µm).

Similar to the case of aluminum, the melt ejection starts at around 50 to 55 ns under both laser fluences. The ejected particles move upwards first and then expand to the radial direction. With the increase of time, some larger particles can be observed in the CCD images, mostly residing in the region close to the target surface. Also stronger melt ejection can be observed in the higher laser flucnece case, as seen in Figure 3.21. The major difference between the aluminum and copper case is that a smaller beam diameter (100 μm vs. 200 μm) was used in the copper case. According to the experimental observation, the average particle size in the copper case is a bit smaller than that in the aluminum case. Based on the kinetic theory (Lu, 2003; Yoo et al., 2000; Lu et al., 2002), phase explosion occurs when the vapor bubbles generated in the superheated liquid grow to a critical radius and expand spontaneously, which depends on the surface tension, critical temperature, pressure of superheated liquid, etc. The critical radius is estimated to be 0.5 μm for copper and 0.7 μm for aluminum. If one can assume that the ejected particle size is closely related to the critical radius of vapor bubble, this might explain the smaller particle observation seen in Figure 3.20. Considering a relatively larger amount of ejected particles in the same volume, one can expect a higher ablation depth in the copper case. The ablation profile is then measured with an optical 3D surface profilometer (KLA-Tencor, MicroXAM-100), as seen in Figure 3.22. Based on the ablation profile, the ablation depth is estimated to be around 5.0 μm under laser fluence of 36 J/cm^2, which is indeed higher than that for aluminum (4.0 μm) under the same laser fluence.

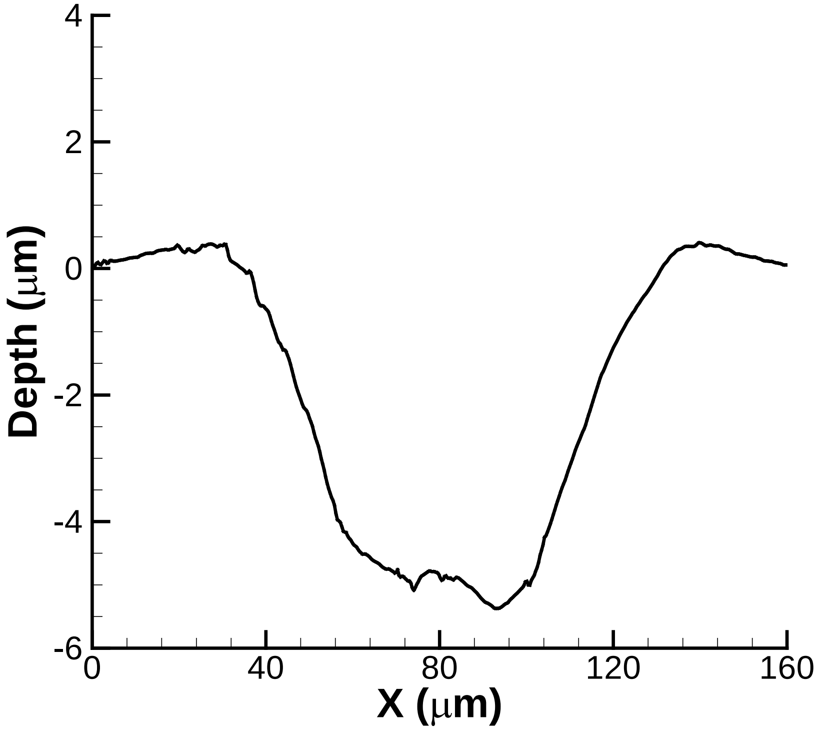

Figure 3.22. Ablation profile for copper under laser fluence 36 J/cm^2 (laser beam pulse duration 6 ns, 1064 nm, beam diameter 100 μm).

With the MD/SPH model, the liquid ejection from the melt pool could be predicted, as shown in Figure 3.23. It can be clearly seen that the melt ejection starts at around 50 ns and reaches its peak at around 80 ns, which agrees well with the experimental observation shown in Figure 3.20. The temperature evolution inside the melt pool and the ejected particle is also shown in Figure 3.23. The ablation depth is predicted to be around 4.6 μm with this MD/SPH model, which again agrees well with the experimental data.

More experimental observations and MD/SPH predictions are listed in the Appendix section.

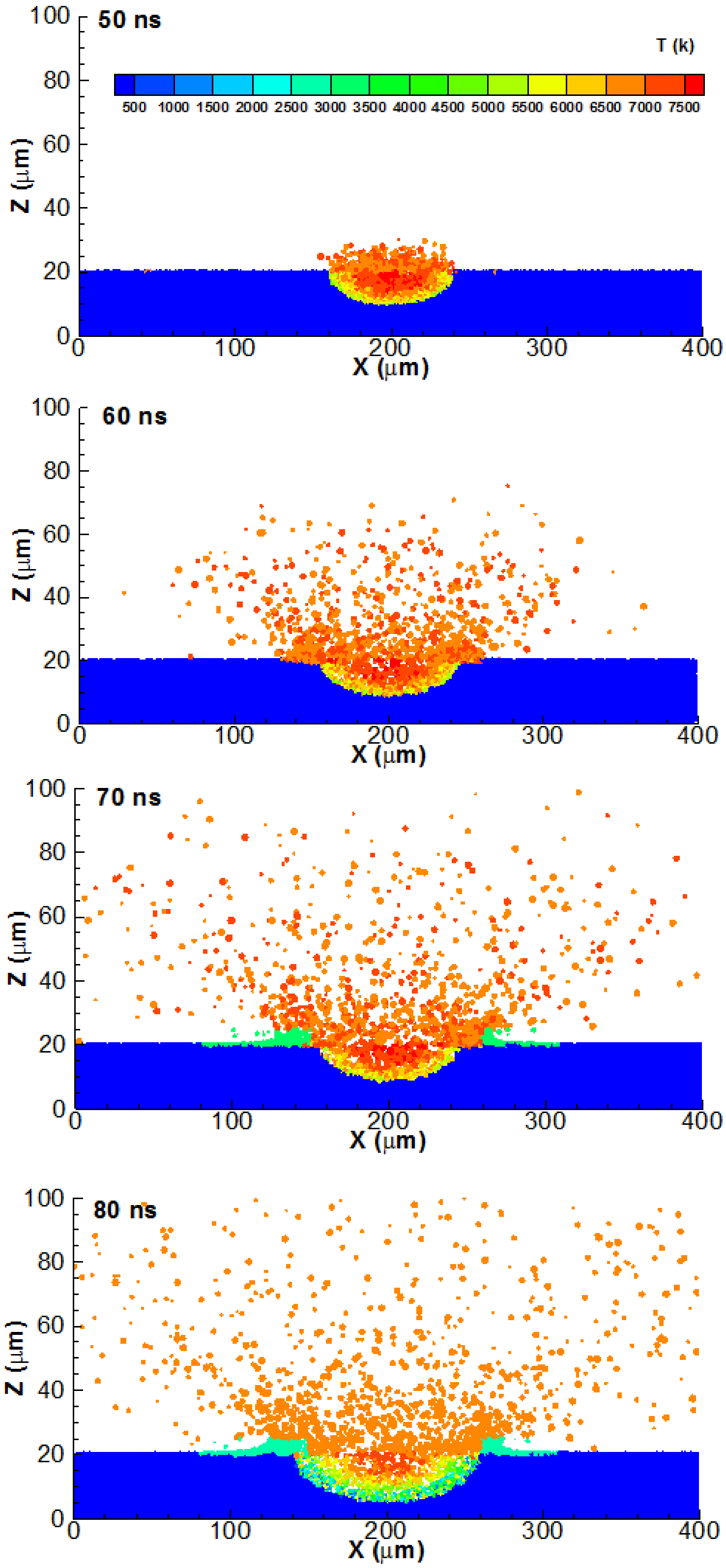

Figure 3.23. SPH calculation results showing the melt ejection for copper (laser fluence 36 J/cm^2, wavelength 1064 nm, pulse duration 6 ns, beam diameter 100 μm).

The critical point temperature for copper reported in literature is around 8280 K (Tavassoli and Khalaji, 2008; efunda.com), 8000 K (Autrique et al., 2012), and 7800 K (Sugioka and Cheng, 2013), 7625 K (Young and Alder, 1971), 8900 ± 900 K (Cahill and Kirshenbaum, 1962), 5330 K (Martynyuk, 1977a), 5450 K (Martynyuk, 1977b), 5400 ~ 6000 K (Kelly and Miotello, 1996; Martynyuk, 1983), 5890 K (Martynyuk, 1992), 7696 K (Hess, 1998), and 8650 K (Singh et al., 2006). It should be noted that all the reported values lower than 6000 K are estimated by Martynyuk (1977 to 1992), which are based on the extrapolation of measurement data for discharging a copper wire until electrical explosion. The measurements were made at the initial point of melting and the initial point of electrical explosion. And then the values above normal boiling point were extrapolated. As acknowledged by Martynyuk (1992), the error of this estimation could be as high as 15%. All the other reported values are in the range of 7600 to 8900 K. Due to this large discrepancy between the two groups of values, it is imperative to determine which group of the value should be used for this work. Similar to the aluminum case, the critical temperature for copper is also predicted by the MD simulation to be 7900 ± 30 K. Based on this calculation, the critical temperature of copper should be in the group with higher values. In this work, T_c value is taken to be 8000 K since it is in the middle of the reported values and also close to the predicted value by MD calculation. If 0.9 T_c is used as the criterion for the ablation depth prediction for this phase explosion process, the ablation depth should be around 3.0 μm based on the calculation from the HD model, which is almost 40% lower than the experimental measurement. A further investigation indicates that the predicted ablation depth would increase to around 5.0 μm if 0.8 T_c is used instead as the criterion.

More cases with different laser flucences are also tested. The melt ejection is calculated with MD/SPH model and compared with the HD model prediction and experimental data, as seen in Figure 3.24. In all the cases shown in Figure 3.24, the MD/SPH prediction show better agreement with the experimental data than the HD prediction based on 0.9 T_c as the criterion for the ablation depth prediction. Also if 0.8 T_c is used as the ablation depth prediction criterion, the HD prediction is closer to the experimental data. If 0.75 T_c is used as the ablation depth prediction criterion, the HD prediction is overestimating the ablation depth. Another comparison to the literature data (Fishburn et al., 2000) is shown in Figure 3.25. Similarly, the HD prediction based on 0.8 T_c criterion shows better agreement with the experimental data and MD/SPH prediction than the 0.9 T_c does.

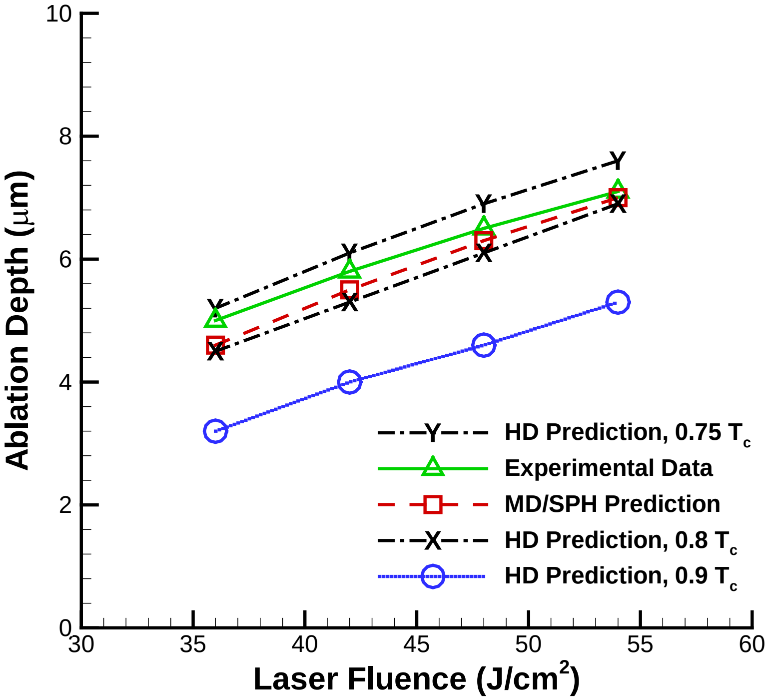

Figure 3.24. Comparison of ablation depth under different laser fluences for copper. Simulation data are from the HD model (laser wavelength 1064 nm, pulse duration 6 ns, beam diameter 100.0 μm, single shot laser ablation).

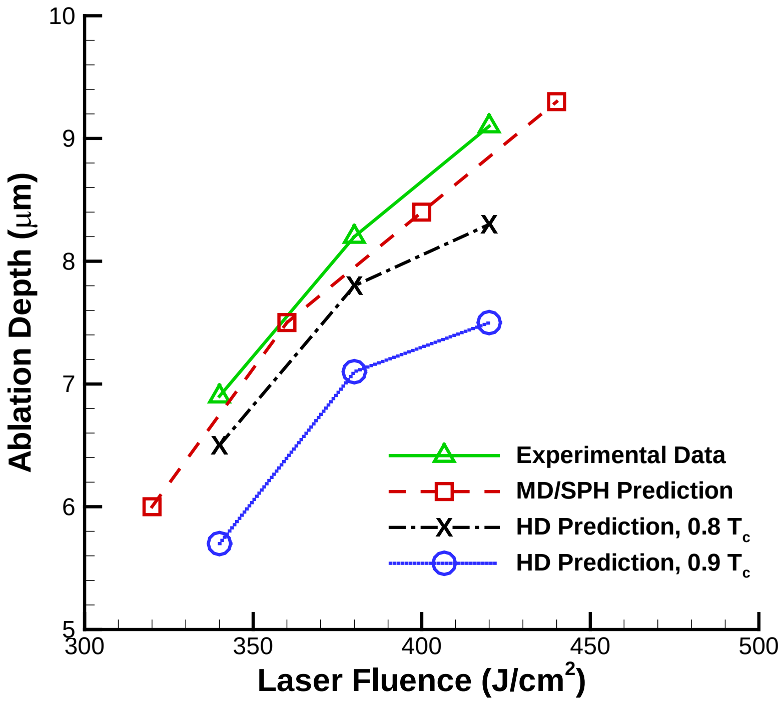

Figure 3.25 Comparison of ablation depth under different laser fluences for copper. Experimental data are from Fishburn et al. (2000), simulation data are from the HD model (40.0 ns, 532 nm, beam diameter 150.0 μm, Gaussian beam, single shot laser ablation).

Therefore, these comparisons further confirm that the 0.9 T_c criterion doesn't always work for all materials. At least for copper, 0.75 to 0.8 T_c might be more appropriate to be used as the ablation depth prediction criterion for the HD model in the cases considered in this work. On the other hand, the MD/SPH model could predict the ablation depth and the associated ablation behavior well.

Due to the uncertainty of the critical temperature of copper, it is better to investigate the effect of the picked value. If Martynyuk's estimated value (around 5800 K) is used in this work, 0.9 T_c would yield a temperature of 5220 K and the ablation depth prediction would be over 10 μm, which would significantly overestimate the copper ablation even under the highest laser fluence shown in Fig. 25. As a result, 0.9 T_c criterion would not work in all the cases investigated in this work. Similarly, if a much higher value (more than 8500 K) is used, the ablation depth would be significantly underestimated. This simple analysis indicates that both Martnyuk's estimation and the higher values reported by Cahill and Kirshenbaum, (1962) and Singh et al. (2006) are not applicable for the laser ablation of copper when phase explosion occurs. Based on the value used in this work (8000 K), 0.9 T_c yields a temperature of 6300 K. To make the 0.9 T_c criterion work in this temperature, one would need a critical temperature of 7100 K for copper. To the best knowledge of the author, there is no critical value reported in this range in the literature. This again verifies that the value used in this work is reasonable for the analysis of phase explosion for copper.

3.5 Summary

Nanosecond laser ablation of aluminum and copper with phase explosion was investigated through a multi-scale model and experimental verification. The model prediction of the melt ejection behavior agrees well with the experimental observation in terms of the phase explosion starting time, particle expansion characteristics, and ablation depth. The commonly used ablation depth prediction criterion of 0.9 T_c is found to be not correct for copper when phase explosion is involved, while it is reasonable for aluminum. In the cases considered in this work, 0.75 ~ 0.8 T_c is found to be a better criterion for copper. The model developed in this work has been shown to provide better capability of predicting the ablation depth and the associated ablation behavior with phase explosion.

CHAPTER 4. MECHANICAL EFFECT OF CONFINED PLASMA

The mechanical effect of confined plasma is investigated in this chapter, including the target surface integrity change and induced residual stresses in the Laser shock peening (LSP) process and shock wave propagation and spallation behavior in LSP.

4.1 Single Shot and Overlapping Laser Shock Peening

4.1.1 Introduction

As reviewed in Chapter 1, despite the extensive experimental and theoretical work on laser shock peening (LSP), rather little work has been reported on the change of target surface integrity and residual stresses by single shot and overlapping LSP while taking into account of the accurate laser-induced plasma pressure with strict physics-based theories. The objective of this work is to explore LSP potential on various metal samples through predictive modeling and experimental studies, especially in the target surface integrity change and induced residual stresses in terms of laser parameters and overlapping ratio.

4.1.2. Experimental Setup and Procedure

The same experimental setup shown in Figure 2.1 is used in this study. A frequency-doubled Nd-YAG laser (wavelength 532 nm) is used to generate a laser beam, which passes through a half-wave plate, polarizer, three high reflecting mirrors and a focus lens, and finally focuses on the surface of workpiece. The workpiece is placed into a water tank to produce a water-confinement regime. The movement of workpiece in X and Y direction is controlled by two linear motion stages. With this setup, the laser power density can be easily adjusted by fine-tuning the orientation of the half-wave plate. The laser beam diameter focused on the workpiece surface can also be changed by varying the distance between the focus lens and the surface of the workpiece. The beam profile used in this work is shown in Figure 4.1, which is nearly top-flat spatially.

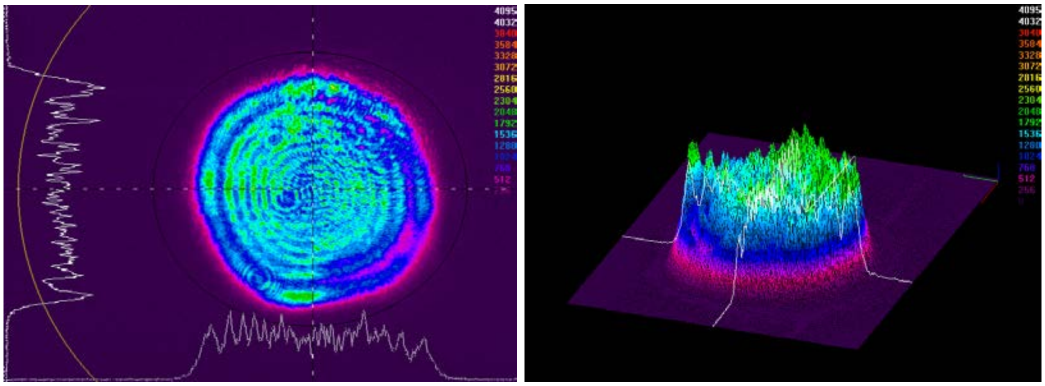

(a) (b)

Figure 4.1. Measured beam profile (a) 2-D (b) 3-D.

To fully explore the LSP potential on different substrate materials, different sets of LSP conditions were designed for the investigation of target surface integrity change and induced residual stresses in LSP, as listed in Table 4.1. The substrate materials used in this work include 4140 steel, 12 Cr stainless steel, 316L steel, and Ti-6Al-4V (Ti64). Black paint, aluminum tape, and vinyl tape of prescribed thickness were applied as coating materials on the sample surface under different LSP tests.

Table 4.1. LSP conditions used in this work.

Substrate Material	Coating Material	Coating Thickness (μm)	Pulse Duration (ns)	Beam Diameter (mm)	Power Density (GW/cm^2)	Laser Wavelength
4140 steel	Black Paint	38 ~ 100	6	0.3	3 ~ 7	532
	Vinyl Tape	100	20	5.0	7	1064
12 Cr stainless steel*	Al Tape	70	3	6.0	10	1064
316L steel*	Al Tape	70	10	6.0	7	1064
Ti64	Black Paint	100	6	1.2	4, 7	1064

Note: * LSP conditions taken from Peyre et al., 2007.

Single shot LSP was chosen as the starting point because it is easy to implement both in experimental and modeling work. In the experiment, a single pulse laser beam irradiates a specific position of the workpiece surface. An indentation is generated with this method and can be measured after removing the coating material from the substrate. Different levels of laser power density and coating thickness were used to investigate the effect of these parameters on the residual stresses and indentation generated in this process.

Single-track overlapping LSP experiments were also performed on the 4140 steel substrate with black paint coating. Figure 4.2 (a) shows the schematic of single-track overlapping LSP. By controlling the distance between two consecutive laser shots, the overlapping ratio can be precisely controlled.

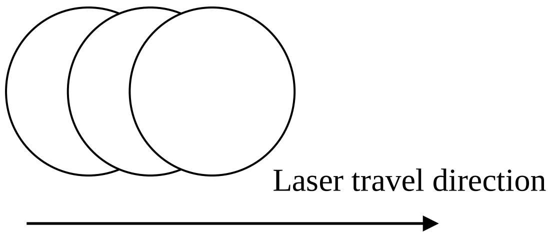

(a) Single-track

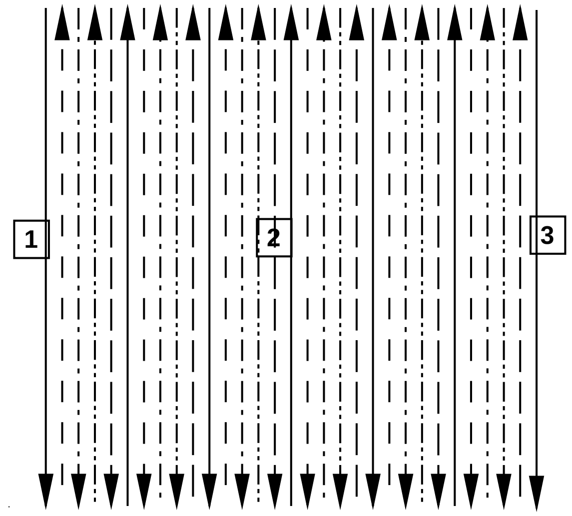

(b) Multi-track

Figure 4.2. Schematic of Laser traveling scheme for overlapping LSP.

To generate a larger area with nearly uniform residual stresses on the sample surface, multi-track overlapping LSP was used. The laser traveling scheme is shown in Figure 4.2 (b) for the multi-track LSP. Laser travels along the solid line from left to right, and the arrow shows the direction of laser traveling along each track. Once finishing traveling along all the solid lines, the laser moves back to the leftmost position and travels along the dashed line, and then in the order of dashdot line, dashdotdot line, and long dashed line to generate a multi-track pattern on the coating surface. By using this scheme, the possibility of coating cracking could be minimized. The number in the scheme with a box indicates the different regions of the shock peened area, where measurements of indentation profile and residual stresses were taken after the experiment.

To reduce the effect of pre-existing residual stresses, the sample was carefully prepared with the following procedures: the sample was first polished with sand papers (360 grit and 600 grit). Then it was heat treated to relieve the residual stress generated by the previous cutting and/or machining process. The sample was then gently polished with diamond tape and alumina. Finally the sample surface was etched to further reduce the residual stress to be very close to 0. After the above procedures, the effect of pre-existing residual stresses is significantly minimized and the sample preparation process will not induce further residual stresses on the sample.

4.1.3. Theoretical Model

4.1.3.1. Confined Plasma Model

The confined plasma model developed earlier by Wu and Shin (2005) can be used to calculate the plasma pressure generated during LSP in a water confinement regime. In their model, the plasma expansion was treated as a one-dimensional phenomenon because the two-dimensional effects are important only when the laser beam diameter is very small. Wu and Shin (2007b) further demonstrated that the 1-D assumption is valid when the laser beam diameter is equal or larger than 300 μm. Since the laser beam diameter used in this work is at least 300 μm, it is sufficient to use this 1-D model in this work to describe the confined plasma behavior under water.

The major energy transport processes related to confined plasma in LSP are shown in Figure 4.3. Since water is transparent to laser and plasma radiation, the water-plasma-coating system gains energy through absorbing the incoming laser beam by plasma and coating surface. Part of laser energy is reflected at water-plasma interface. The confined plasma is formed through the ionization of coating and water vapor. The evaporation and ionization of coating layer is attributed to the laser energy reaching the coating surface directly, and the energy conducted and radiated from the plasma. The energy conducted from the plasma to the water is the main energy source for water evaporation. The plasma gains energy mainly by absorbing the laser beam passing through it and loses energy due to its spatial expansion and through thermal conduction and radiation to water and coating surface. The vaporized water and coating will also bring their internal energy into the plasma.

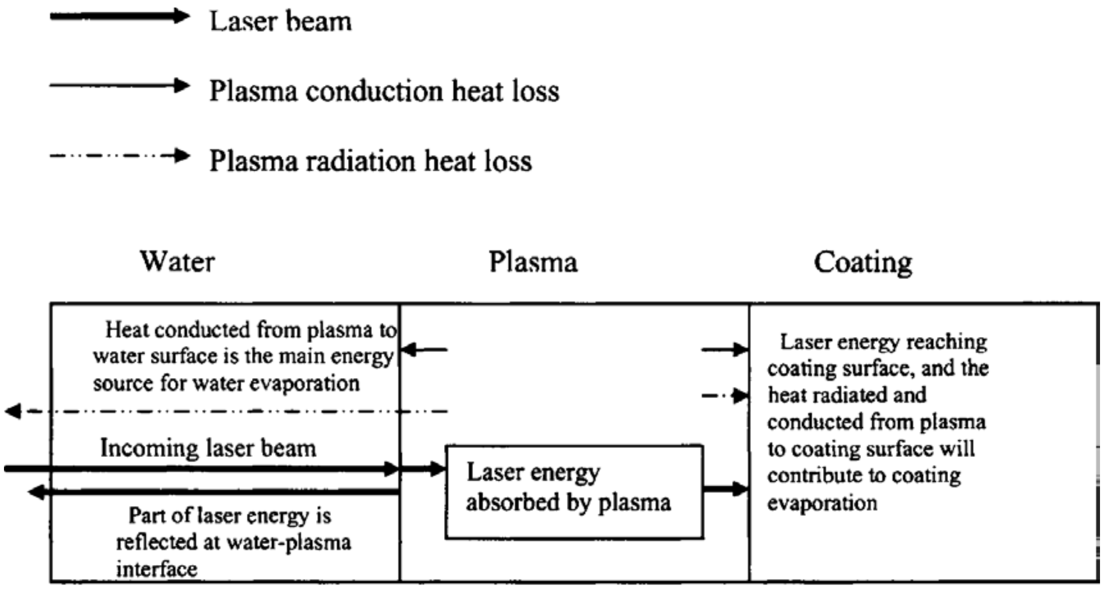

Figure 4.3. Major energy transport processes related to confined plasma in LSP (Wu and Shin, 2005).

In this model, the reflectivity at the water-plasma interface was calculated through Drude model. The total absorption coefficient of plasma was the sum of the electron-ion and electron-atom inverse-bremsstrahlung absorption coefficient and of photo-ionization absorption coefficient. The electron number density was connected to the electron temperature through Saha equation. This model considered most of the important physical processes of LSP, including the laser ablation of the coating layer, water evaporation, plasma ionization and expansion, energy loss of plasma through radiation and electron conduction, laser absorption by plasma through inverse bremsstrahlung effect and photo-ionization, reflection of laser beam at the air-water interface and plasma-water interface, etc. Solving this confined plasma model, one can obtain the plasma pressure history in LSP applications. This model was validated successfully against the available experimental results in literature (Wu and Shin, 2005). The code used in this part of the work is taken from Wu and Shin (2005).

Figure 4.4 shows the plasma pressure predicted by this model for the laser beam of 6 ns FWHM with 50 μm black paint on the 4140 steel substrate. Generally, maximum plasma pressure increases with the laser power density. The pulse duration for pressure wave is about two times the laser pulse duration (FWHM).

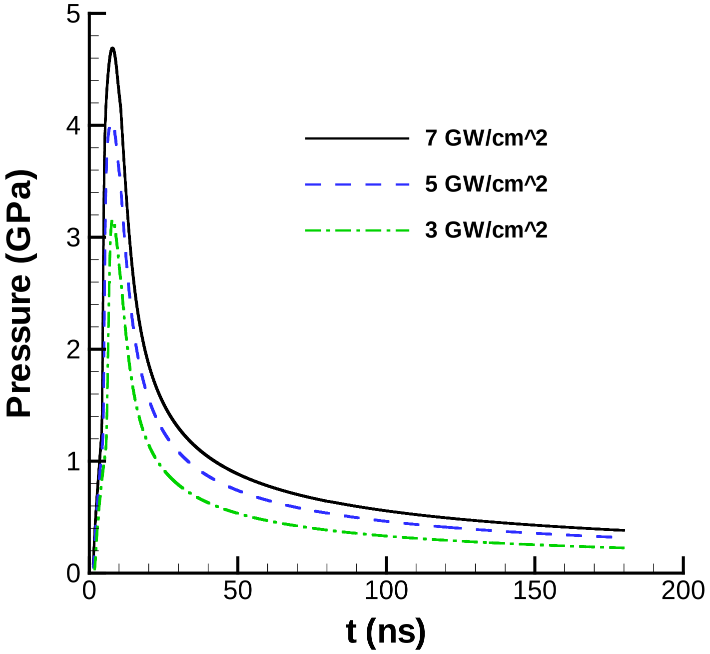

Figure 4.4. Plasma pressure history for laser shock peening of 4140 steel (laser wavelength 532 nm, FWHM 6 ns, 50 μm black paint).

4.1.3.2. 3-D Finite Element Model

A 3-D finite element model (FEM), as shown in Figure 4.5, has been developed to calculate the shock wave propagation and the resultant residual stresses on the target material with the confined plasma pressure as input. The load shown in Figure 4.5 is modeled as a distributed pressure in ABAQUS and its distribution is controlled by a user subroutine VDLOAD. The bottom surface of the sample (XY plane) is considered to be fixed.

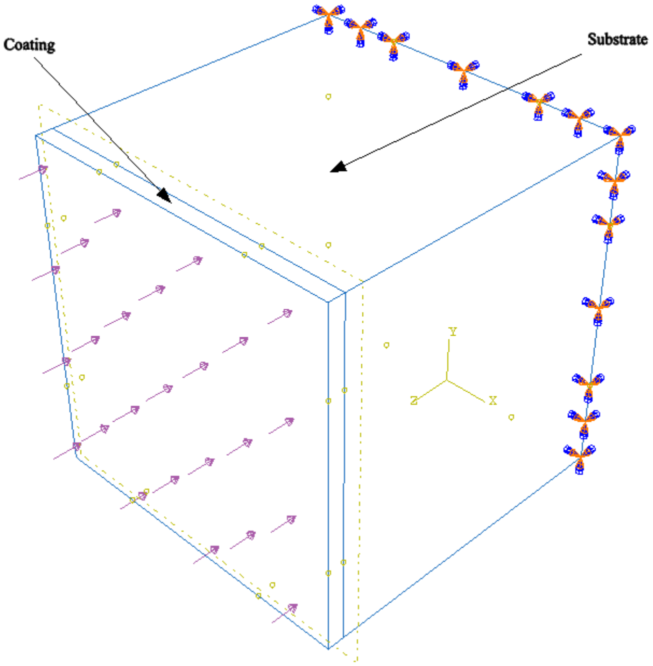

Figure 4.5. Scheme of 3-D FEM model.

The structural coupling between the coating layer shock wave pressures and the substrate structural displacements at their common surfaces (the interface) was accomplished with the TIE constraint option in ABAQUS (ABAQUS Documentation, 2006). With this constraint, the displacements of the nodes in load direction (Z direction in Figure 4.5) on slave surface (coating layer) will be kept the same as that of the closest nodes on the master surface (substrate).

It should be noted that the dynamic behavior of substrate material plays an important role in the development of residual stress. In the LSP process, the typical strain rate is as high as 10^7 s^{-1}. Thus, the dynamic yield strength of substrate material is significantly increased due to the work hardening and strain rate hardening effect. In this work, the dynamic behavior of substrate material was described by Johnson-Cook model (Johnson and Cook, 1983):

$$\sigma = (A + B\varepsilon^n)\left[1 + Cln\left(\frac{\dot{\varepsilon}}{\dot{\varepsilon_0}}\right)\right], \text{ where } \dot{\varepsilon_0}=1 \text{ s}^{-1} \tag{3}$$

where $\dot{\varepsilon}$ represents strain rate and ε is strain, A, B, C, and n are constants. Due to the use of coating material as a thermal protection layer, the increase of temperature in the substrate material is negligible and thus the temperature softening effect in Johnson-Cook model is not considered. The Johnson-Cook model constants for all the four substrate materials used in this work are listed in Table 4.2.

Table 4.2. Johnson-Cook model constants for substrate materials.

	A (MPa)	B (MPa)	C	n	Reference
4140 Steel	792	510	0.014	0.26	Johnson and Cook, 1983
12 Cr	870	400	0.015	0.4	Peyre et al., 2007
316L	300	600	0.045	0.35	Peyre et al., 2007
Ti64	840	550	0.064	0.812	Meyer, 2006

For the coating material, black paint is treated as pure carbon since the major component of black paint is carbon. The coating layer is assumed to be elastic-perfectly plastic material. The mechanical and physical properties of all the materials can be obtained from reference (matweb.com; Urech et al., 2007; Borsenberger and Weiss, 1998).

To obtain the indentation depth information on the substrate surface and in-depth residual stress, two paths are defined in ABAQUS as shown in Figure 4.6. Path 1 represents the interface between the coating material and substrate material. Path 2 extends from the surface of substrate to the depth of several mm.

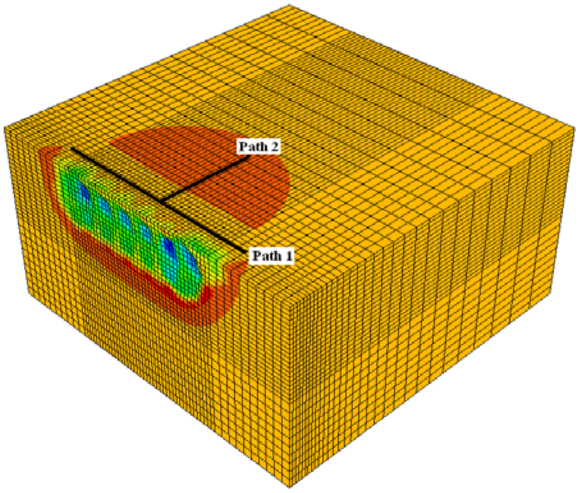

Figure 4.6. Path definition in 3-D FEM model.

4.1.3.3. Calculation Procedure

The FEM calculation procedure is shown in Figure 4.7. With this procedure, both single shot and overlapping LSP can be handled successfully. The computational cost will also be reduced significantly by combining ABAQUS/Explicit and ABAQUS/Standard (Braisted and Brockman, 1999).

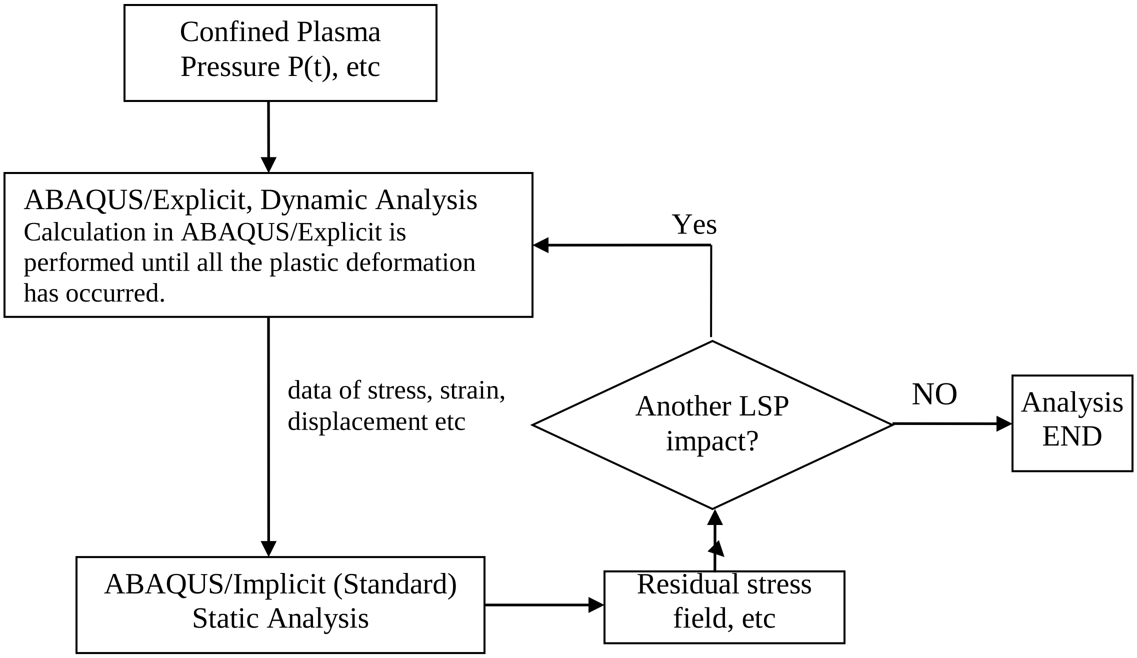

Figure 4.7. FEM calculation procedure (Wu and Shin, 2007c).

4.1.4. Results and Discussion

4.1.4.1. Single Shot LSP

A. Indentation Profile

The effects of coating thickness and laser power density on the indentation profile and residual stresses were investigated with single shot laser shock peening. In this case, the substrate material was 4140 steel and the coating material was black paint. As mentioned in Table 4.2, the laser power density varied from 3 to 7 GW/cm^2 and the coating thickness varied from around 35 to 70 μm. The laser beam used in this experiment had the pulse duration of 6 ns and wavelength of 532 nm. The laser beam diameter was around 300 μm.

By using an optical profilometer, the indentation profile after LSP was measured. Following the calculation procedures in Section 4.1.3.3, the indentation profile after LSP can be calculated along path 1 as defined in Figure 4.6. Figure 4.8 shows the comparison of indentation depth from simulation results and experimental data with the coating thickness of 50.8 μm. A reasonable agreement can be observed between the predicted and measured indentation depths under several laser power densities.

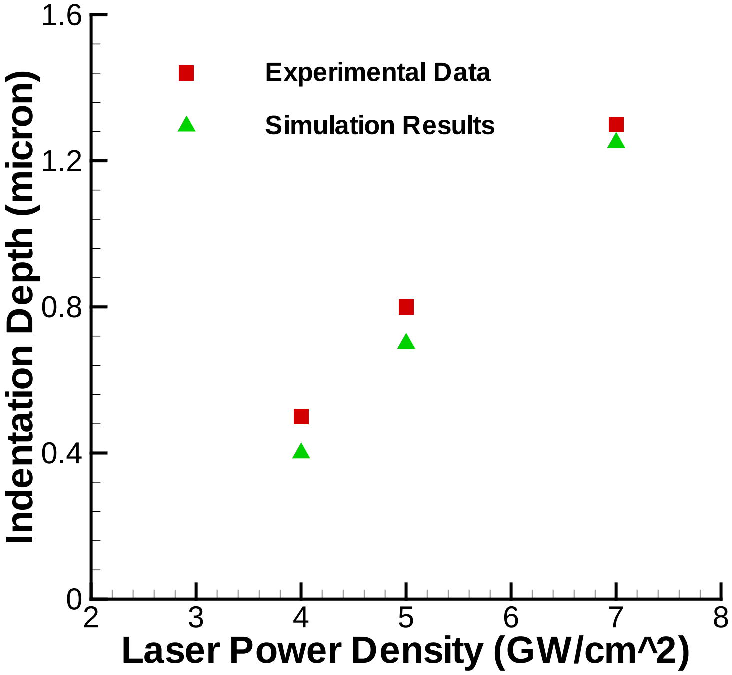

Figure 4.8. Comparison of indentation depth under different laser power densities (substrate: 4140 steel, coating: black paint, coating thickness 50.8 μm).

The variation of indentation depth of three samples with the coating thickness of 38.1, 50.8, and 66.0 μm under different laser power densities are shown in Figure 4.9. It can be seen from Figure 4.9 that the indentation depth increases with laser power density nearly linearly. A larger indentation depth is expected if a higher laser power density is used. However, water breakdown may occur in the higher power density range (Wu and Shin, 2006b). Thus, the highest power density used in this work was chosen to be less than 8 GW/cm^2. Under this limit, no water breakdown was observed during the experiments. The indentation depth also decreases with coating thickness as seen in Figure 4.9, which is caused by the dissipation of energy into the coating layer when the pressure wave propagates into the coating/substrate system. With thicker coating, more energy dissipates into coating and less energy can be used to generate the indentation on the substrate surface.

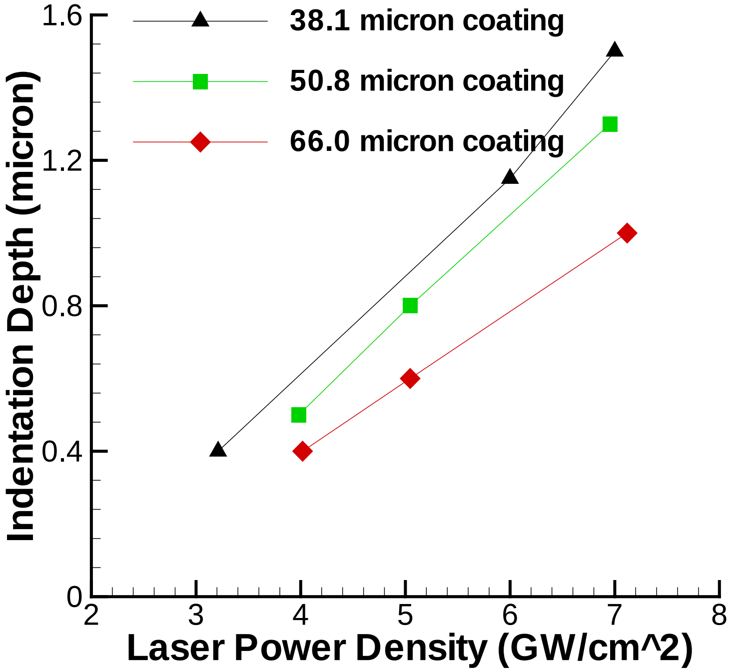

Figure 4.9. Indentation depth under different LSP conditions.

B. Validation of Residual Stress

To validate the residual stress prediction, two benchmark cases for which experimental data are available in literature were calculated using the aforementioned LSP model. The LSP conditions of the two benchmark cases are summarized in Table 4.1. For the first case, the material used in the process was 12 Cr steel (Peyre et al., 2007). The laser beam used in the work had pulse duration of 3 ns and diameter of 6 mm. The laser power density was 10 GW/cm^2. The protective layer was 70 μm aluminum coating. The material used in the second case was 316 L steel (Peyre et al., 2007). The laser pulse duration was 10 ns and the power density was 7 GW/cm^2 in this case. The beam diameter and coating material were kept same as in the first case. The dynamic behavior of both materials under very high strain rate was modeled by Johnson-Cook model (Peyre et al., 2007).

The simulation results and comparison with experimental data are shown in Figure 4.10. It can be seen from Figure 4.10 (a) that the simulation results from the current model is closer to the experimental data in the region of depth less than 0.4 mm compared with Peyre et al.'s results (Peyre et al., 2007). The residual stress prediction in the second case is also very close to the experimental data, as shown in Figure 4.10 (b). This is attributed to the more accurate pressure history input that is obtained from the confined plasma model in the FEM calculation. Overall, reasonable predictions of residual stresses were obtained in both cases, which validated the efficacy of the aforementioned model.

C. Prediction of Residual Stress for 4140 Steel

After the validation of indentation depth and residual stress, it is expected that the current model can predict residual stresses reasonably well for 4140 steel under typical LSP conditions. Figure 4.11 (a) shows the in-depth residual stress distribution for 4140 steel under different laser power densities. As the power density increases from 3 GW/cm^2 to 7 GW/cm^2, the maximum compressive residual stress also increases from about 250 MPa to 600 MPa. In all of these cases, the maximum residual stress occurs at the region around 50 μm below the substrate surface.

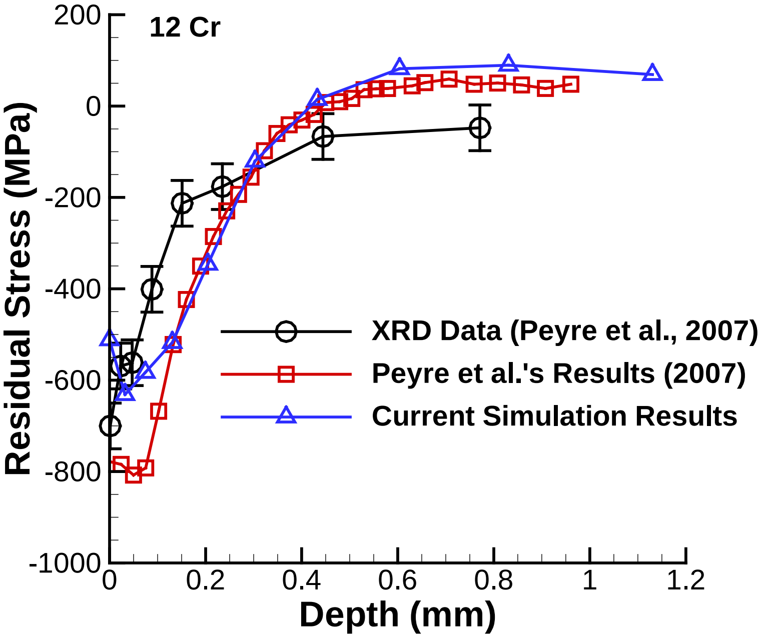

(a)

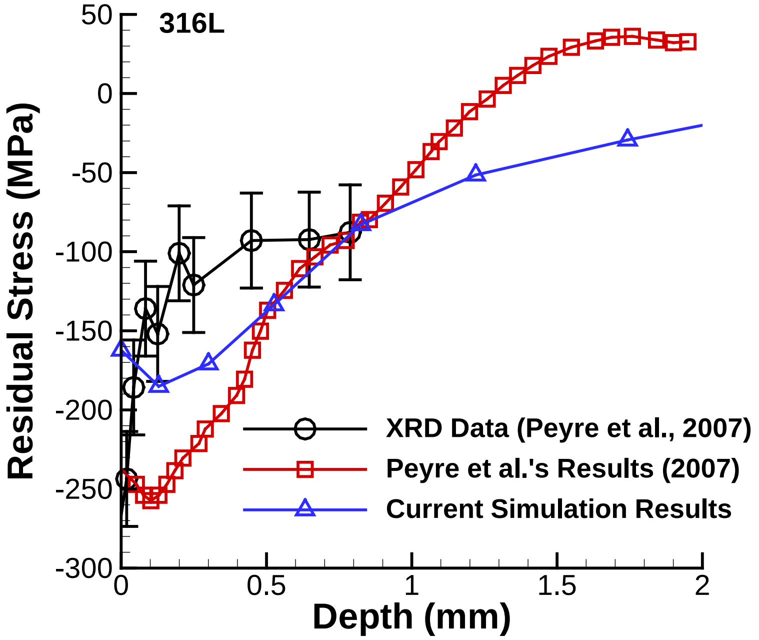

(b)

Figure 4.10. In-depth residual stress distribution of benchmark cases (a) 12 Cr, laser power density 10 GW/cm^2, pulse duration 3 ns, Al coating (b) 316L steel, laser power density 7 GW/cm^2, pulse duration 10 ns, Al coating.

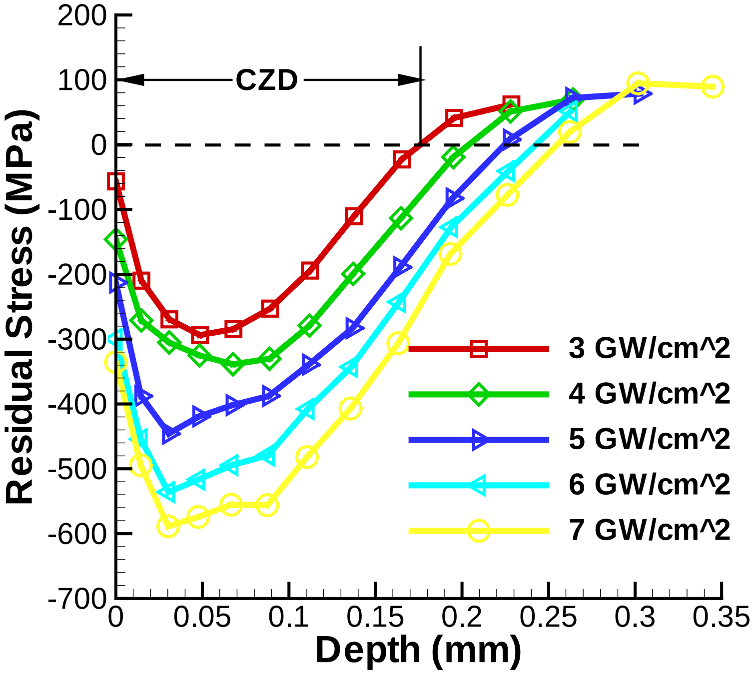

(a)

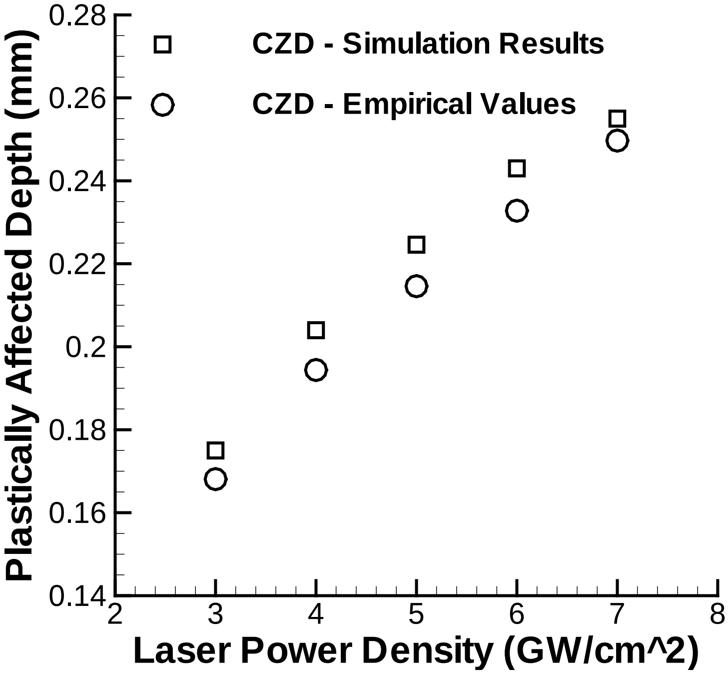

(b)

Figure 4.11. Prediction of in-depth residual stress for 4140 steel (a) In-depth residual stress distribution (b) Comparison of compressive zone depth after LSP (Laser pulse duration 6 ns, beam diameter 300 μm, coating thickness 50 μm).

The compressive zone depth (CZD) is defined as the depth of the region which has compressive residual stresses after LSP. Peyre et al. (1998) proposed an empirical equation of CZD given by

$$CZD = \frac{P_{\max}}{2HEL}\left(\frac{C_{el}C_{pl}}{C_{el} - C_{pl}}\tau\right) \tag{4}$$

where P_{max} is the laser-induced peak pressure; HEL is Hugoniot elastic limit of the substrate material; C_{el} and C_{pl} are elastic and plastic wave velocity in the substrate material, respectively (6000 m/s and 4500 m/s for 4140 steel); τ is the pressure wave duration (FWHM, about 12 ns for a 6 ns laser pulse). The CZD values obtained from Figure 4.11 (a) are compared with the values calculated from the above empirical expression, as shown in Figure 4.11 (b). A reasonably good agreement was obtained for the conditions investigated in this work.

4.1.4.2. Single-Track Overlapping LSP

A. Experimental Results

Several overlapping ratios and laser power densities were chosen to investigate the single-track overlapping LSP. The substrate material was still 4140 steel and the coating material was black paint. The coating thickness used in this section was chosen to be 65 μm to sustain multiple impacts in the overlapping region. The shock peened samples were measured by using an optical profilometer and the 3-D indentation profiles along laser traveling direction are shown in Figure 4.12.

With the power density of 6 GW/cm^2 and overlapping ratio of 38%, the indentation profile shown in Figure 4.12 (a) is not uniform along the laser traveling direction. From the 3-D profile, the variation of indentation depth can be clearly seen. When the overlapping ratio is increased to 58%, the indentation depth becomes more uniform along the laser traveling direction, as shown in Figure 4.12 (b), and hence more uniform surface residual stress can result.

For the power density of 5 GW/cm^2, two overlapping ratios were used in the experiments. Nearly uniform indentation depth can be observed in both cases, as shown in Figure 4.12 (c) and (d). Clearly the indentation depth is more uniform in the higher overlapping ratio case (68%) than in the lower overlapping ratio case (58%). Under the same overlapping ratio (58%), higher laser power density can generate more uniform indentation depth along laser traveling direction, which can be seen from Figure 4.12 (b) and (c). Thus, to generate uniform indentation depth on the substrate, it is preferable to use higher laser power density and larger overlapping ratio. However, as mentioned previously, too higher laser power density can lead to water breakdown (Wu and Shin, 2006b) and also may initiate cracks in the coating layer (Chai, 2003). The crack of coating layer was observed in this single-track overlapping experiment when the laser power density is 6 GW/cm^2 with the overlapping ratio 68%. Therefore, an optimum value should be used under a certain coating condition to avoid both water breakdown and coating layer crack.

B. Simulation Results of Indentation Profile

The indentation profile along laser traveling direction can be calculated by the 3-D FEM model. The comparison of average indentation depth is shown in Table 4.3, which shows some degree of discrepancy between experimental results and calculated values. It's attributed to the substrate surface roughness and non-uniformity of coating thickness.

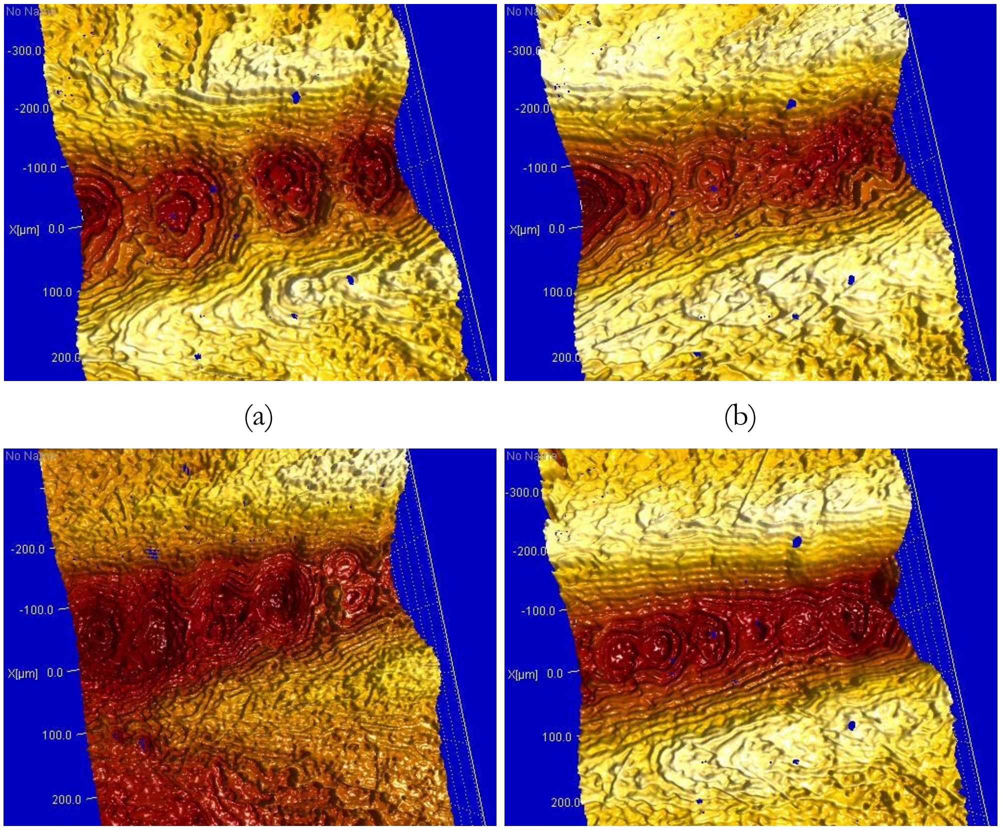

(a) (b)

(c) (d)

Figure 4.12. Indentation profile of single-track overlapping LSP on 4140 steel (a) overlapping ratio 38%, 6 GW/cm^2 (b) overlapping ratio 58%, 6 GW/cm^2 (c) overlapping ratio 58%, 5 GW/cm^2 (d) overlapping ratio 68%, 5 GW/cm^2 (65 µm black paint coating, beam diameter 300 µm, pulse duration 6 ns, wavelength 532 nm).

Table 4.3. Comparison of average indentation depth.

	Overlapping ratio 58%		Overlapping ratio 68%	
	Exp (µm)	Cal (µm)	Exp (µm)	Cal (µm)
6 GW/cm^2	1.5	2.2	N/A	N/A
5 GW/cm^2	1.1	1.6	1.5	2.1

C. Prediction of Residual Stress

The residual stresses on the substrate surface and depth directions can also be calculated from the 3-D FEM model, as seen in Figure 4.13. The residual stress on the substrate surface was taken along the center line of the laser track. The in-depth residual stress was obtained at the position directly under the 4th laser shot, which is at the center of the 7 shots simulated in the calculation. Under the same laser power density, the residual stresses on the substrate surface in larger overlapping ratio (68%) case are a little higher than that in the case of 58% overlapping ratio, while the in-depth residual stresses are greater in the subsurface region for the case with smaller overlapping ratio. Under the same overlapping ratio, both the residual stresses on the substrate surface and depth directions in higher power density (6 GW/cm^2) case are a little higher than those in the case of 5 GW/cm^2 power density.

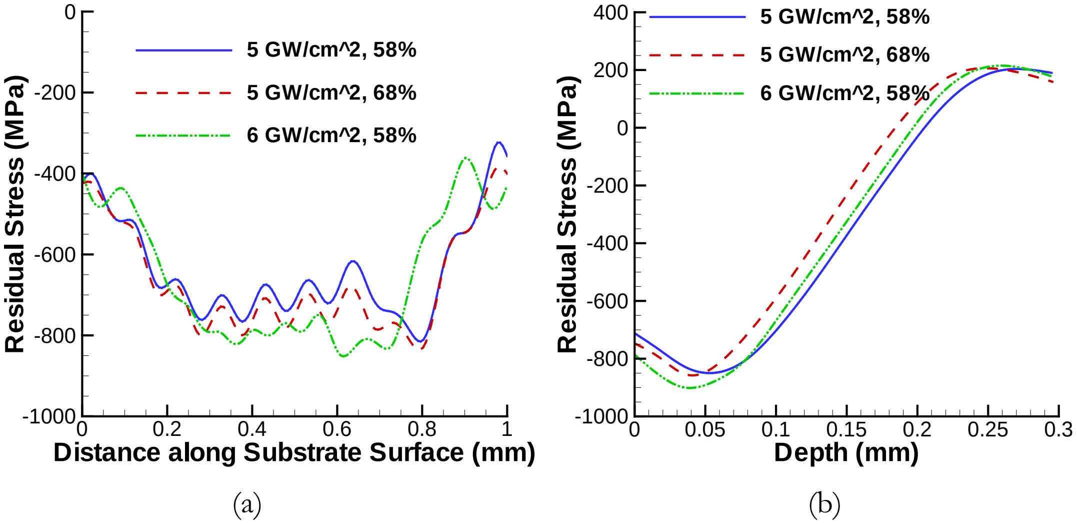

Figure 4.13. Residual stress profile after single-track overlapping LSP on 4140 steel with different laser power densities and overlapping ratios (a) residual stress on substrate surface (b) in-depth residual stress (65 μm black paint coating, beam diameter 300 μm, pulse duration 6 ns, wavelength 532 nm).

It should be noted that the peak residual stress is significantly increased from around -500 MPa to -800 MPa compared to the single shot case, as shown in Figure 4.11, which is mostly due to the overlapping effect. The compressive zone depth is kept at around 0.2 mm because the same coating material and laser parameters were used in both cases. This indicates that the overlapping ratio has almost no effect on the compressive zone depth.

Another effect of overlapping is shown in Figure 4.14. The number (1 to 7) in the figure shows how many laser shots have been applied. It can be seen from Figure 4.14 that the peak residual stress increased through laser shot 1 to 5. However, it decreased considerably after shots 6 and 7 were applied, which indicates that there is a stress relaxation effect in the overlapping LSP process. The shock waves generated by laser shots 6 and 7 significantly altered the existing stress state by pushing the peak residual stress to a deeper location and relaxing the peak residual stress to a smaller value.

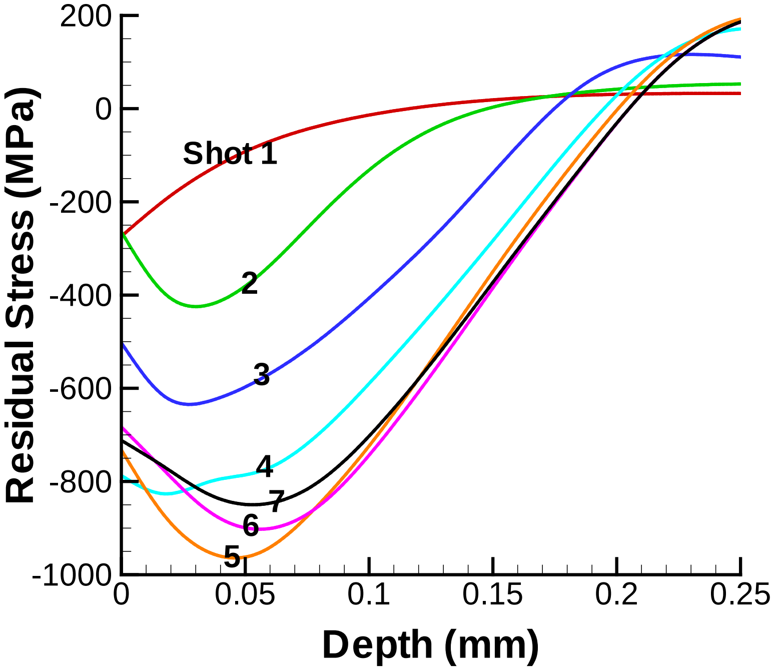

Figure 4.14. In-depth residual stress after single-track overlapping LSP on 4140 steel (65 μm black paint coating, beam diameter 300 μm, pulse duration 6 ns, wavelength 532 nm, overlapping ratio 58%, laser power density 5 GW/cm^2).

4.1.4.3. Multi-Track Overlapping LSP

Two substrate materials (4140 steel and Ti64) and two coatings (black paint and vinyl tape) were used for multi-track overlapping LSP. A system of 4140 steel and black paint was first employed to investigate the indentation profiles generated by multi-track overlapping LSP. Then two pairs of substrate/coating systems (4140 steel/vinyl tape, and Ti64/black paint) were used to study the residual stresses induced in multi-track LSP.

A. Indentation Profile

For the multi-track overlapping LSP, the coating layer has to sustain higher impacts from multiple overlapping shots compared with the single shot and single-track LSP applications. Thus, to avoid the cracks of coating layer and generate observable indentation on the substrate material, the coating thickness was chosen to be 100 μm in all the cases. For the 4140 steel/black paint system, the laser power density used in the experiment was 5.8 GW/cm^2. The laser beam diameter was around 300 μm and the overlapping ratio was 39%.

To consider the repeatability of the multi-track LSP on 4140 steel, 5 samples were shock peened under the same conditions. The indentation depth at the left edge were measured and shown in Figure 4.15. It can be seen that the indentation depth is around 0.4 to 0.5 μm in all the cases, which proves the repeatability of this process.

The indentation profile after multi-track LSP was also calculated using the model developed in this work. To reduce the computation cost, only 3 tracks were calculated. There are 7 shots along each track. The indentation profile along path 1 as defined in Figure 4.7 is shown in Figure 4.16. The average indentation depth is around 0.55 μm, which is close to the experimental value of 0.4-0.5 μm.

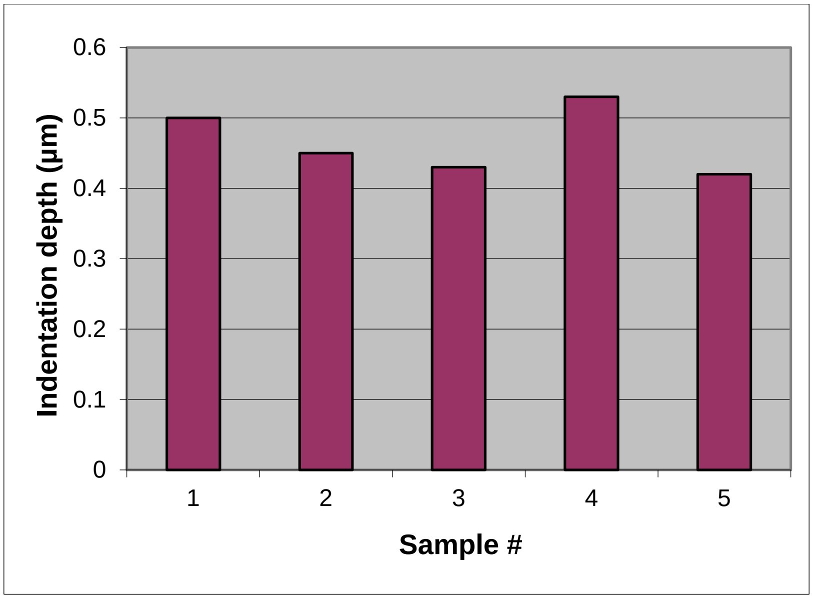

Figure 4.15. Indentation depth of different sample under same LSP conditions (All indentation depths are measured at left edge of shock peened area. black paint coating thickness 100 µm, overlapping ratio 39%, power density 5.8 GW/cm^2, beam diameter 300 µm, pulse duration 6 ns, wavelength 532 nm).

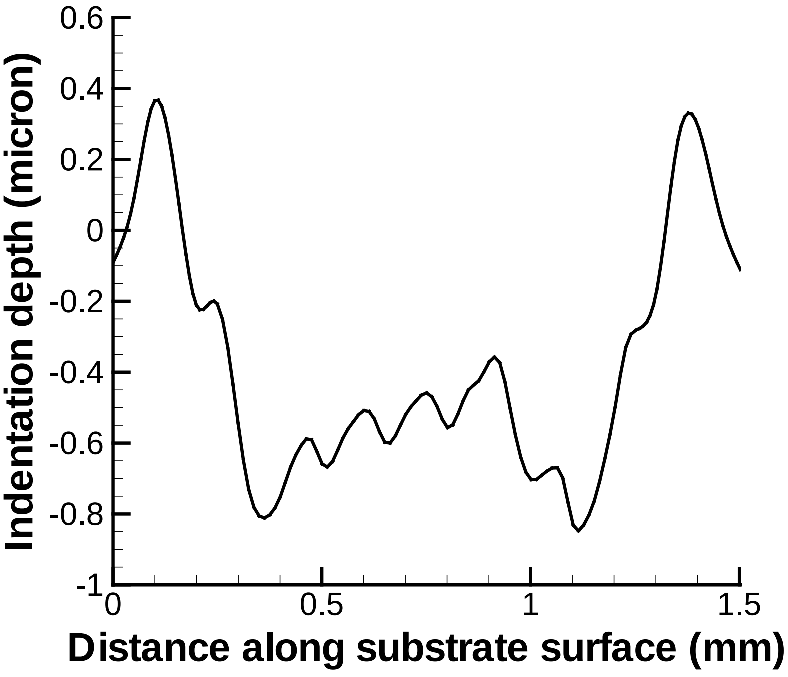

Figure 4.16. Indentation profile on 4140 steel surface (black paint coating thickness 100 µm, overlapping ratio 39%, power density 5.8 GW/cm^2, beam diameter 300 µm, pulse duration 6 ns, wavelength 532 nm).

B. Prediction of Residual Stress for Multi-track LSP

To investigate the residual stress induced in multi-track overlapping LSP, several 4140 steel samples were shock peened by Laser Shock Peening Technology (LSPT) under different conditions. Then the residual stresses distribution after LSP were calculated using the model developed in this work and compared with the XRD measurement data.

The coating material used at LSPT was standard black polyvinyl tape with thickness of 100 μm. In all the cases, the laser beam diameter was 5.0 mm and the laser beam pulse was 20 ns. The laser beam wavelength was 1064 nm. The actual laser beam spatial profile is shown in Figure 4.17. Since the majority of the beam profile is uniform and the overall average is 7 GW/cm^2, it is valid to assume the profile to be uniform (flat-top). Therefore, the calculation of plasma pressure using 1D confined plasma model is justified.

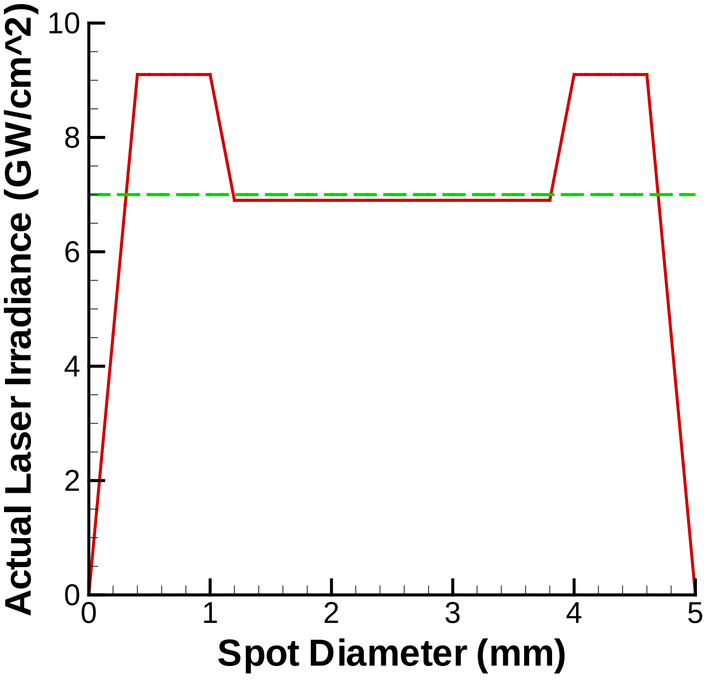

Figure 4.17. Beam profile of LSPT laser.

By utilizing a chemical etching technique (ASM Handbook, 2004), the residual stresses of a LSPT sample in the depth direction were measured to the depth of more than 1 mm below the original surface using Cr Kα radiation source. The residual stresses after each etching were measured and shown in Figure 4.18 (a). It can be seen that the measured residual stress near the surface is close to the simulation results. In the subsurface region, the compressive residual stress becomes smaller first and then gets larger till around 0.5 mm below the surface. After 0.5 mm, the residual stress decreases with the depth. The measured data for another steel sample with overlapping ratio of 50% are also shown in Figure 4.18 (b). In both cases, the simulation results agree reasonably well with the measured XRD data, which serves as a validation of our complete LSP model.

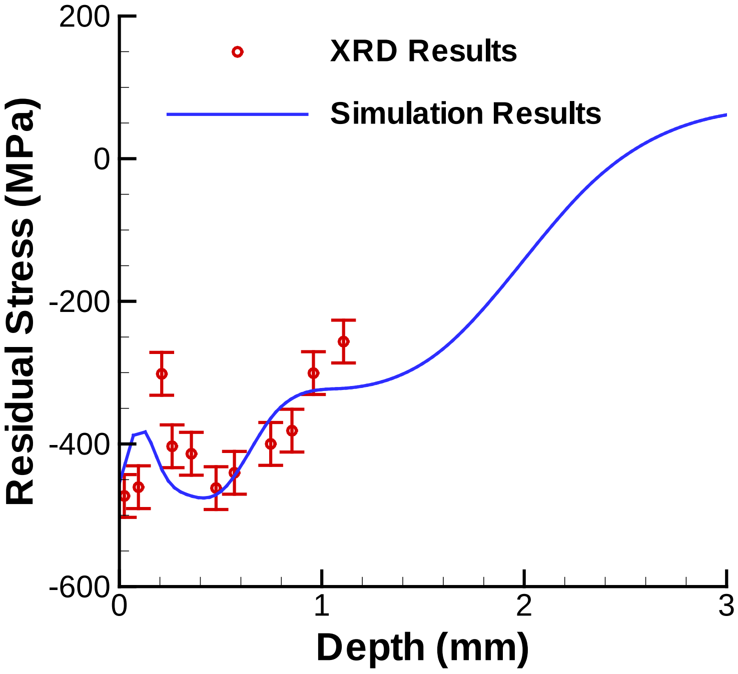

(a)

Figure 4.18. Comparison of measured XRD results and simulation results for multi-track LSPT 4140 steel samples with different overlapping ratio (a) Overlapping ratio 40% (b) Overlapping ratio 50% (laser power density 7 GW/cm^2, beam diameter 5 mm, pulse duration 20 ns, wavelength 1064 nm, vinyl tape coating).

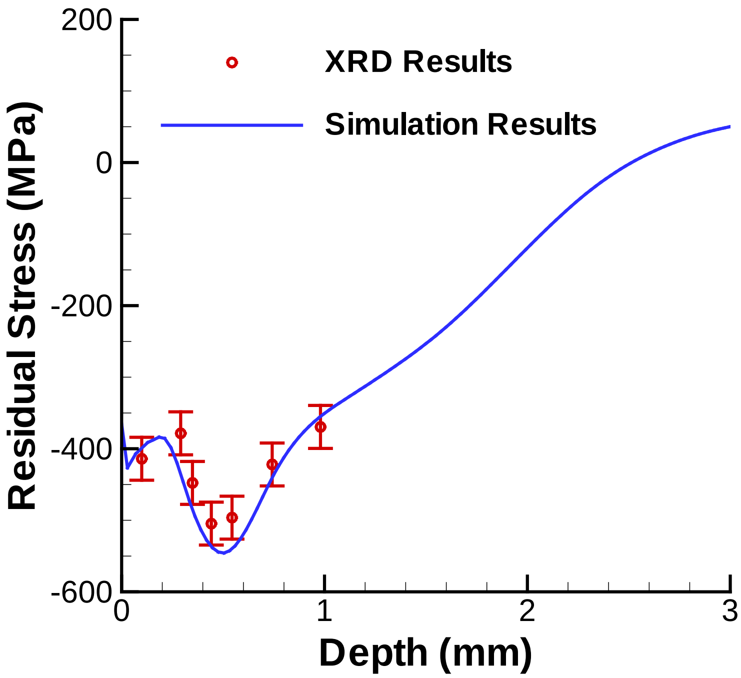

(b)

Figure 4.18. Continued.

The compressive zone depth in this multi-track LSP case is more than 2 mm, which is much higher than those in the single shot and single-track LSP case due to the longer laser pulse (20 ns v.s. 6 ns) according to Eq. (2). Certainly, the peak plasma pressure and coating material properties also contribute to this large increase in the compressive zone depth. The peak residual stress is also larger with higher overlapping ratio as indicated in Figure 4.18, which is similar to the single-track LSP case.

It should also be noted that the peak residual stress in this multi-track case is less than -600 MPa while it is around -800 MPa in single-track case as shown in Figure 4.13. One possible reason is that smaller overlapping ratios are employed in this case (40~50% v.s. 58~68%). It may also due to the stress relaxation effect as discussed in single-track case. More neighboring shots are applied in this multi-track case compared with single-track LSP. Therefore, the stress relaxation may play a more important role in this case.

Further residual stress prediction was carried out on a Ti64 sample. In this case, the coating material was black paint with thickness of 100 μm. The laser beam diameter was 1.2 mm and the laser beam pulse was 6 ns. The laser beam wavelength was 1064 nm. The residual stresses of the laser treated Ti64 sample was measured using conventional XRD with Cu Kα radiation source. The depth characterization of residual stress was obtained by chemical etching method similarly as in previous 4140 steel case (ASM Handbook, 2004).

Figure 4.19 shows the simulation results and experimental data for residual stress distribution in the depth direction for Ti64 under different laser power densities. In both cases, the current 3D FEM model can accurately predict the residual stress distribution in subsurface region with slight difference in some locations. Overall, reasonable good agreements were obtained for both cases. As in the single shot case, higher laser power density can increase not only the peak residual stress but compressive zone depth.

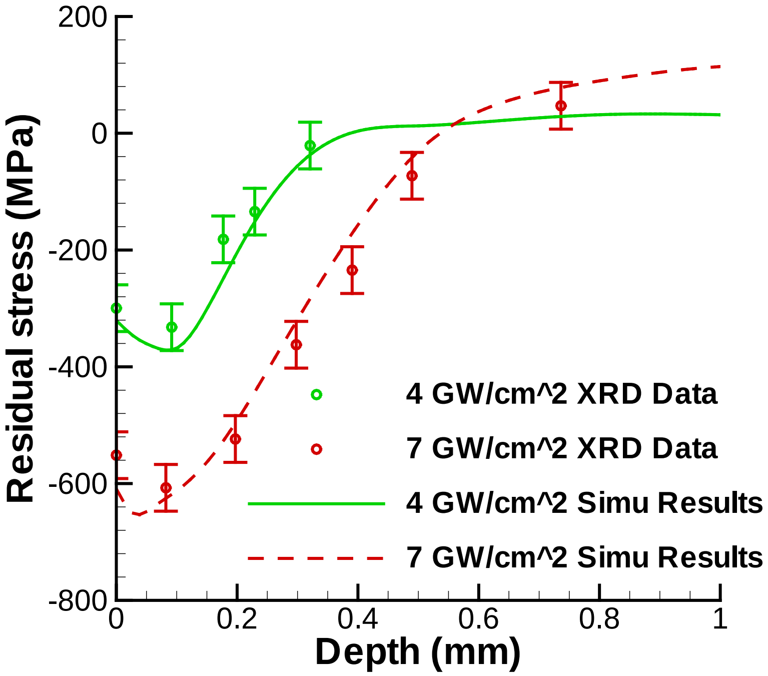

Figure 4.19. Residual stress distribution for laser shock peening on Ti64 under different laser power densities (beam diameter: 1.2 mm, pulse duration 6 ns, wavelength 1064 nm, coating: 100 μm black paint, overlapping ratio: 50%).

4.1.5. Summary

A 3-D finite element model with a confined plasma model has been developed and used to simulate the LSP process. By using these combined models, the indentation depth and residual stresses could be accurately calculated under different LSP conditions. Single shot, single-track overlapping, multi-track overlapping LSP experiments have been performed on various metals under different LSP conditions. The model prediction of indentation profiles and residual stresses in the depth direction provided good agreement with experimental data. It was found that higher laser power density can increase not only the peak residual stress but compressive zone depth. The overlapping ratio contributed to the peak residual stress while showing almost no effect on the compressive zone depth. Longer laser pulse resulted in larger compressive zone depths. Stress relaxation effect was also observed in overlapping LSP process.

4.2 Shock Wave Propagation and Spallation

4.2.1 Introduction

In the laser shock peening (LSP) process, high energy laser irradiated on the target surface can generate high-pressure plasma in the water confinement regime (Berthe et al., 1997; Wu and Shin, 2005). When the pressure wave propagates into the substrate material as a shock wave, compressive residual stresses can be imparted into the surface region (Braisted and Brockman, 1999). If the shock wave amplitude and the duration of this shock wave are sufficient, spallation will take place at the interface or inside the bulk material. The objective of this work is to develop a complete and general model for the shock wave propagation and spallation in the laser shock peening process.

4.2.2. Theoretical Model

4.2.2.1. Pressure Wave Prediction Model

The confined plasma model developed earlier by Wu and Shin (2005) can be used to calculate the plasma pressure wave generated during LSP in a water confinement regime. The details of this model have been discussed in Section 4.1.3.1.

4.2.2.2. Shock Wave Propagation in Solids

Based on the pressure pulse loading amplitude, the shock wave propagation in the solid requires the assumption that the solid body deforms either elastically or loses its rigidity and behaves like a liquid. Correspondingly, there are two model frameworks that can be used to simulate the above two conditions: the elasticity theory and the hydrodynamic theory.

In the elastic regime, the pressure pulse loading amplitude is less than the elastic limit of the solid material. If the pressure pulse loading amplitude is much higher than the elastic limit of the solid material, as is the case in LSP, the solid material will behave as a fluid. Under this regime, the shock wave propagation can be described by a hydrodynamics model.

The Lagrangian form of the conservation equations leads to Lagrangian codes in which the mesh is determined by the material and deforms with it, whereas the Eulerian mesh is fixed in space (Meyers, 1994). Lagrangian codes are much more efficient to run (less computational time) and the interface of two materials can be easily defined. The disadvantage of Lagrangian code is that the mesh becomes excessively distorted after a critical plastic strain and the predictions can be inaccurate (Meyers, 1994). Eulerian codes can handle large deformations very well but present unique problems when two different materials are present in the computational domain. Since the two materials have different constitutive equations, the same element will have different materials at different time, and thus it is difficult to track the material interfaces.

For the spallation process, it is important to track the interface of two different materials. Since the plastic strain is also not high enough to reach the critical state, it is more convenient to use Lagrangian mesh to model the spallation process.

In Lagrangian coordinate system, the hydrodynamic equations are given by (Meyers, 1994; Miklowitz, 1969; Kanel et al., 2004; Peikrishvili et al., 2000; Davidson, 2008; Antoun et al., 2003)

$$\text{Conservation of mass: } \frac{D\rho}{Dt} + \rho\nabla \bullet U = 0 \tag{5}$$

$$\text{Conservation of momentum: } \frac{\rho DU}{Dt} = -\nabla P \tag{6}$$

$$\text{Conservation of energy: } \frac{dE}{dt} + P\frac{dV}{dt} = 0 \tag{7}$$

where ρ is the density, U the particle velocity, E the internal energy, and P the pressure. In the energy equation, V is the specific volume ($V=1/\rho$).

In the above three equations, there are four unknown variables (ρ, U, E, and P), and thus an additional equation is needed to solve the problem. This additional equation is the constitutive relation for the material, which relates the stress to kinematic and thermodynamic variables. There are two conditions to consider depending on the material strength effects.

i). Strength effects are neglected

If the strength effects are negligible, the constitutive relation is simply the equation of state (EOS) of the material. Under shock loading, the Mie-Gruneisen EOS is most widely used, which is valid for shock loading pressure up to a few hundred GPa (Meyers, 1994). In the shock regime, the Mie-Gruneisen EOS relates a (P, V, E) state to the pressure and internal energy at 0 K as follows:

$$P - P_0 = \frac{\gamma}{V}(E - E_0) \tag{8}$$

where γ is the Gruneisen constant and V is the specific volume. It can also be related to another reference state, like a point on the Hugoniot plot. In this case

$$P - P_H = \frac{\gamma}{V}(E - E_H) \tag{9}$$

Under the adiabatic shock loading condition, the internal energy in Mie- Gruneisen EOS is the sum of potential energy and vibration energy of atoms. The vibration energy of atoms will change during the shock wave propagation due to the vibrational frequency change, which occurs with the volume change of the solid material.

ii). Strength effects are important

When strength effects are significant, the stress-tensor components are divided into a hydrostatic pressure and a deviatoric stress component (Fan et al., 2005):

$$\sigma_{ij} = -P_h + S_{ij} \tag{10}$$

In this condition, the equation of state for hydrostatic pressure P_h is supplemented with a constitutive relation for the yield strength, which is related to deviatoric stress S_{ij}. According to von Mises yield condition, the material starts to yield and exhibits plastic behavior if the following relationship holds (Fortov and Kostin, 1991):

$$\sum S_{ij}^2 + 2S_{12}^2 \geq \frac{2}{3}Y \quad (11)$$

where Y is the dynamic yield strength. The dynamic yield strength depends on strain, strain-rate, and loading history. The constitutive relation can take a strain, strain-rate hardening form such as Johnson-Cook or others:

$$Y = f(\varepsilon, \dot{\varepsilon}, P) \quad (12)$$

4.2.2.3. Shock Wave Interaction at Interface of Different Media

For a double-layered target, the shock wave propagation becomes much more complicated due to the presence of an interface between the two media. This case is especially important because the substrate/coating system has to be treated as a double-layered target in the laser shock peening process.

When a shock wave propagates from medium A to medium B, a change in pressure, wave velocity, and density will take place. Figure 4.20 shows the schematic of shock wave propagation and the relevant quantities. The subscripts used in Figure 4.20 indicate different stage of shock wave propagation: *I* for incident wave, *R* for reflected wave, and *T* for transmitted wave. At the interface, the equilibrium of pressure exists such that

$$P_I - P_R = P_T \quad (13)$$

Also, the continuity condition at the interface (no gaps can be created and matters can't superimpose each other) yields

$$U_{PI} + U_{PR} = U_{PT} \quad (14)$$

where U_{PI}, U_{PR}, and U_{PT} are the particle velocities as shown in Figure 4.20.

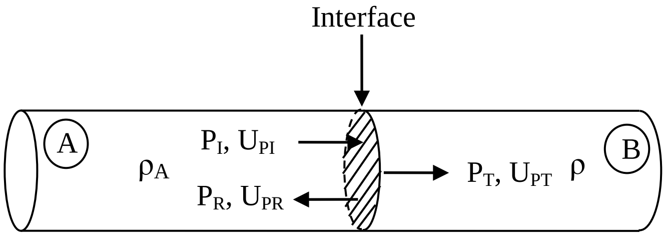

Figure 4.20. Scheme of shock wave propagation in two different media.

In addition, the following relationships exist between the above quantities (Meyers, 1994):

$$P_I = \rho_A U_{SI} U_{PI} \tag{15}$$

$$P_R = \rho_A U_{SR} U_{PR} \tag{16}$$

$$P_T = \rho_B U_{ST} U_{PT} \tag{17}$$

$$U_{SI} = C_{0A} + S_A U_{PI} \tag{18}$$

$$U_{SR} = C_{0A} + S_A U_{PR} \tag{19}$$

$$U_{ST} = C_{0B} + S_B U_{PT} \tag{20}$$

where U_{SI}, U_{SR}, and U_{ST} are the shock velocities corresponding to particle velocities U_{PI}, U_{PR}, and U_{PT}, respectively; and C_{0A}, S_A, C_{0B}, S_B are material constants for shock wave propagation. Eqs. (15) to (17) represent conservation of momentum for the incident shock wave, reflected shock wave, and transmitted shock wave, respectively. Eqs. (18) to (20) are often known as the equation of state (EOS) of a material, where S_A and S_B are empirical parameters and C_{0A} and C_{0B} are the sound velocity in material A and B at zero pressure. In the above equations, P_I, C_0, and S are known variables. Therefore, the 8 unknowns can be determined by solving the 8 equations simultaneously.

4.2.2.4. Spallation Prediction

For the failure mechanism used to predict the spallation, several models have been proposed in literature. The simplest one is based on an assumption that spallation will take place when the tensile stress is higher than a constant threshold value (Cottet and Boustie, 1989). While spallation takes place, the stress in the damaged area will be zero. Therefore, the simple model can only predict the initiation of spallation, but can't predict the growth of the damage area. Also, the stress relaxation is not considered in the simple model. There are more physically accurate models that consider the nucleation and growth of the voids and cracks in the damaged area. The continuous kinetic model of spallation is the most widely used (Fortov and Kostin, 1991; Meyers, 1994; Antoun et al., 2003). In this model, the kinetic equation relates crack growth rate to the volume of cracks formed and effective stress (Fortov and Kostin, 1991):

$$\frac{dV_t}{dt} = \begin{cases} -k \bullet sign(P) \bullet (\sigma_{\max} - \sigma_e) \bullet (V_t + V_{t1}), & |\sigma_{\max}| \geq \sigma_e \\ 0, & |\sigma_{\max}| < \sigma_e \end{cases}$$
$$\sigma_e = \sigma_0 \frac{V_{t1}}{V_t + V_{t1}} \tag{21}$$

where V_t is the volume percentage of cracks inside the target, k is a constant depending on the viscosity, V_{t1} is the critical value of V_t, and σ_0 is the initial threshold strength. When the maximum tensile stress reaches the threshold value σ_0, then the voids start to grow in the material. If the volume V_t exceeds the critical value V_{t1}, the growth rate of voids accelerates. The stress relaxation in the cracks is taken into account by corrections of yield strength and shear modulus (Fortov and Kostin, 1991):

$$Y = Y_0 \frac{V_{t1}}{V_t + V_{t1}}, G = G_0 \frac{V_{t1}}{V_t + V_{t1}} \tag{22}$$

4.2.3. Numerical Method

4.2.3.1. Finite Difference of Conservation Equations

As discussed in Section 4.2.2.2, Eulerian codes have a poor resolution of interface tracking when two different materials are present in the computational domain. Since it is very important to track the interface in spallation prediction, a Lagrangian coordinate system is thus employed.

To solve the governing partial differential equations, either the finite-difference or finite-element formulations can be used as the numerical algorithms. It is generally accepted that the finite-element and finite-difference methods give identical algorithms (Meyers, 1994) because the methods used in these two formulations to update the stress, shock viscosity, and energy calculations are virtually identical. The finite-difference method is chosen in this work since it is more straightforward conceptually.

To simplify the problem, the following assumptions are made to reduce the multi-dimensional equations describing shock wave propagation into one-dimensional equations solved in this work:

1. The particle velocity directs along and depends on the one-dimensional coordinate.
2. Adiabatic conditions are assumed throughout the problem.
3. An artificial viscosity is introduced to spread out the pressure and energy discontinuities that develop at the shock front.
4. There is no body force.

In a Lagrangian coordinate system, the mass of each cell remains fixed. The cell boundary position will change with time. The density of a cell at time *t* is given by (Meyers, 1994):

$$\rho = \rho_0 \frac{\partial x_0}{\partial x} \tag{23}$$

where x_0 and ρ_0 are the initial position and density, respectively. In one-dimensional case, the conservation equations become:

$$\begin{aligned} &\frac{\partial V}{\partial t} + \frac{1}{\rho_0}\frac{\partial u}{\partial x} = 0 \\ &\frac{\partial u}{\partial t} + \frac{1}{\rho_0}\frac{\partial P}{\partial x} = 0 \\ &\frac{\partial E}{\partial t} + P\frac{\partial V}{\partial t} = 0 \end{aligned} \tag{24}$$

where V is the specific volume.

The finite difference form of the conservation equations is:

$$\begin{aligned} &\frac{V_i^{n+1} - V_i^n}{\Delta t} = -\frac{1}{\rho_0}\frac{u_{i+1}^n - u_{i-1}^n}{2\Delta x} \\ &\frac{u_i^{n+1} - u_i^n}{\Delta t} = -\frac{1}{\rho_0}\frac{P_{i+1}^n - P_{i-1}^n}{2\Delta x} \\ &E_i^{n+1} - E_i^n = -\frac{P_i^{n+1} + P_i^n}{2}\left(V_i^{n+1} - V_i^n\right) \end{aligned} \tag{25}$$

In the energy equation of Eq. (24), the energy at time t_{n+1} involves the pressure at t_{n+1}, which is a function of the energy at t_{n+1}. The equation is therefore implicit and must be solved numerically with an additional constitutive relation of the material, as discussed in Section 4.2.2.2.

At the shock front, there is a discontinuity in pressure (*P*) and energy (*E*), and the finite-difference method will break down. To overcome this deficiency and make the computation stable, an artificial viscosity is introduced (Meyers, 1994; Peikrishvili et al., 2000) assume a finite thickness of the shock wave, which is about 10-100 μm according to

(Thoma et al., 2005). This is done by adding a term to the pressure so that the pressure change is spread out over a few cells instead of occurring discontinuously. The viscosity term has the form (Meyers, 1994):

$$Q = -\left[\frac{\left(c_Q \Delta x\right)^2}{V} \frac{\partial u}{\partial x} \left| \frac{\partial u}{\partial x} \right| + \frac{c_L \Delta x}{V} \frac{\partial u}{\partial x} \right] \tag{26}$$

where c_Q, c_L are constants and typical values for them are 1.5 and 0.06, respectively. It should be noted that *Q* is large only when there is a sharp change in particle velocity *u*. When *u* is a constant, *Q* vanishes. Therefore, *Q* acts only on the shock front. The conservation of mass and energy equations need to be changed accordingly with the addition of the artificial viscosity:

$$\begin{aligned} &\frac{\partial u}{\partial t} + \frac{1}{\rho_0} \frac{\partial (P+Q)}{\partial x} = 0 \\ &\frac{\partial E}{\partial t} + (P+Q) \frac{\partial V}{\partial t} = 0 \end{aligned} \tag{27}$$

In finite-difference form,

$$\begin{aligned} &\frac{u_i^{n+1} - u_i^n}{\Delta t} = -\frac{1}{\rho_0} \frac{P_{i+1}^n + Q_{i+1}^n - P_{i-1}^n - Q_{i-1}^n}{2\Delta x} \\ &E_i^{n+1} - E_i^n = -\frac{P_i^{n+1} + Q_i^{n+1} + P_i^n + Q_i^n}{2} \left(V_i^{n+1} - V_i^n\right) \end{aligned} \tag{28}$$

For a double-layered target, the shock wave propagation through the media interface is handled with the model presented in Section 4.2.2.3. When the maximum tensile stress reaches the threshold value in some region at certain moment, the continuous kinetic spallation model will take over and the voids will begin to grow in this damage zone.

4.2.3.2. Stability Analysis

To make the computation stable, the time step should meet several requirements. First, the CFL number should be less than or equal to 1 (Bolis et al., 2007):

$$CFL = \frac{C_A \Delta t}{\Delta x} \leq 1 \tag{29}$$

where C_A is the local adiabatic sound speed. For a solid, the adiabatic sound speed is given by (Peters, 1978)

$$\begin{aligned} C_A &= \sqrt{\frac{c^2 V_0 (V_i^n)^2 (S+1) - c^2 V_0^{\,2} V_i^n S}{\left[V_0 - S(V_0 - V_i^n)\right]^3} + 2S V_i^n P_i^n} \\ S &= \frac{\gamma + 1}{2} \end{aligned} \tag{30}$$

where c is the normal density speed of sound in the material.

To avoid the overlapping of cell boundaries in one time step, the following condition should also be met (Peters, 1978):

$$\left(u_{i+1}^n - u_i^n\right)\Delta t < \frac{1}{2}\left(x_{i+1}^n - x_i^n\right) \tag{31}$$

The time step is calculated at the beginning of each iteration for all the cells in the computation domain. The smallest time step value is chosen for all mesh point calculations during the same iteration.

4.2.4. Results and Discussion

4.2.4.1. Shock Wave Propagation in a Single Solid

The accuracy of the numerical model was tested for the shock wave propagation in a single solid. As shown in Figure 4.21, a compressive pressure wave was applied on the right side of the computation domain. Before time t_1, there is no external load and the load is released at time t_2. t_1 and t_2 are set to be 5 ns and 15 ns in the calculation, respectively, to be consistent with the experimental condition used in (Mitchell and Nellis, 1981). The left side of the computational domain was fixed. In this testing case, the strength effect was neglected and the Mie-Gruneisen EOS for aluminum was used.

The comparison of simulation results with experimental data (Mitchell and Nellis, 1981) for aluminum compression under different shock pressures is shown in Figure 4.22. Good agreements were obtained in all the three quantities of shock velocity, shock density, and particle velocity, thus validating the numerical model prediction for shock wave propagation in single solid.

Single layer aluminum and copper films were also chosen to test the prediction accuracy of the shock wave propagation by the numerical model. A Gaussian pressure wave with peak P_{max} was applied on the front surface of the film with the pulse duration (FWHM) of 25 ns. The material properties of Al and Cu are listed in Table 4.4 (Tollier et al., 1998; Bolis et al., 2007).

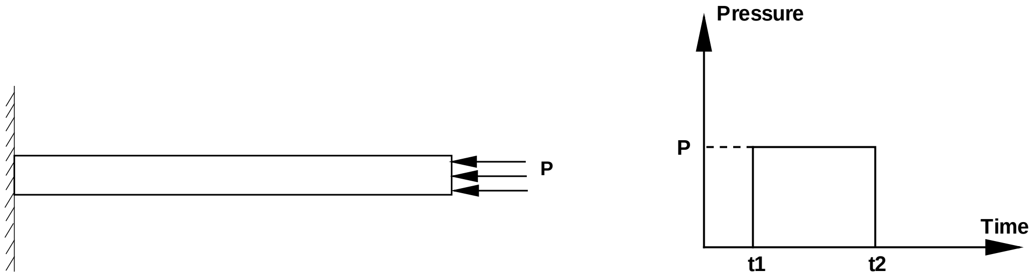

(a) (b)

Figure 4.21. (a) Scheme of shock compression of aluminum bar and (b) pressure input.

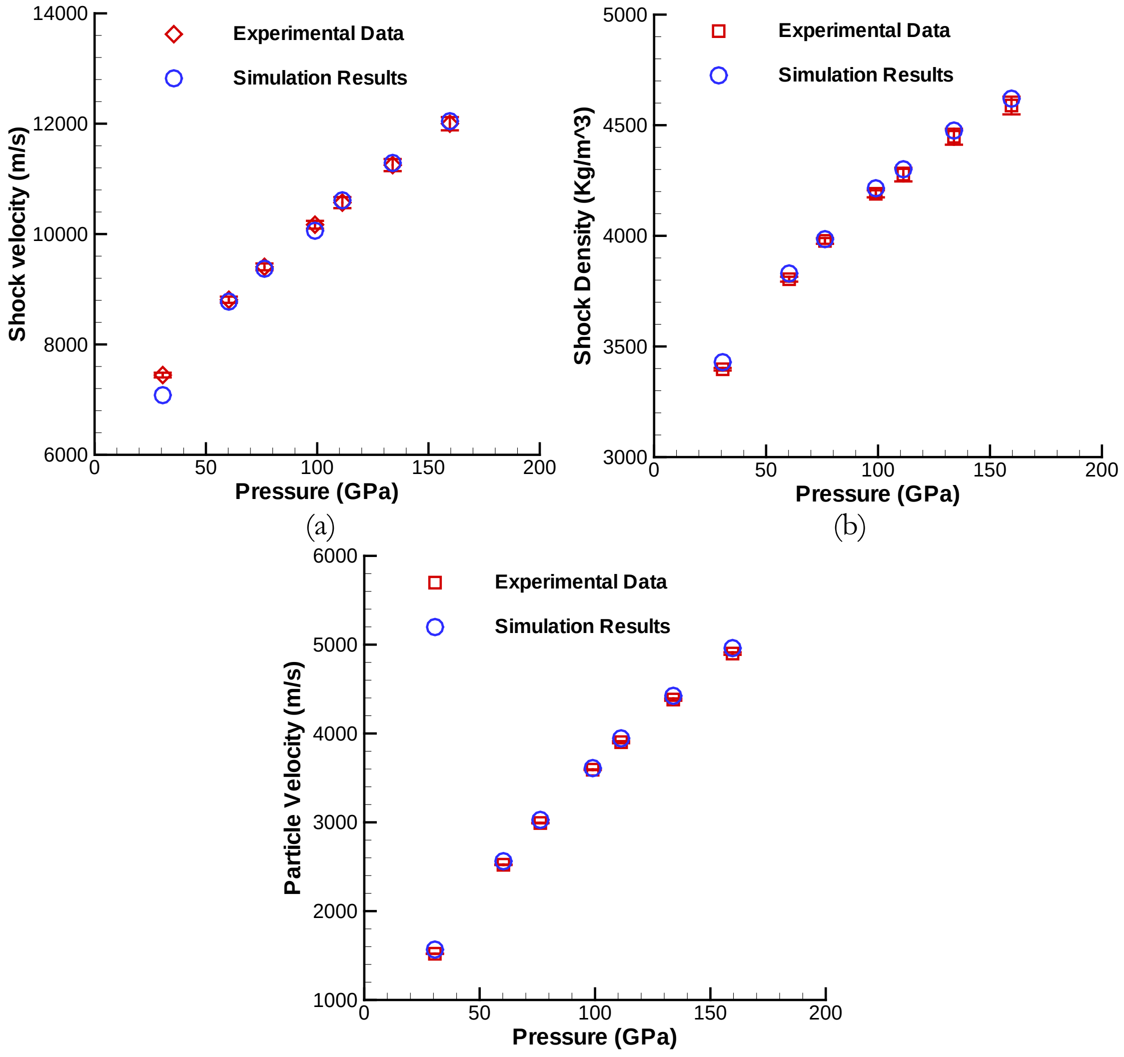

(a) (b)

(c)

Figure 4.22. Comparison of simulation results and experimental data (Mitchell and Nellis, 1981) for shock compression of aluminum (a) shock velocity (b) shock density (c) particle velocity $(\rho_0 = 2705\ \mathrm{kg}/m^3, \gamma = 1.678, c = 5386\ m/s)$.

For an aluminum film with thickness of 250 μm, the rear free surface velocity was calculated and shown in Figure 4.23. In this simulation, the peak pressure used is 2.0 GPa, which is a little higher than the spall strength for aluminum (1.6 GPa, Tollier et al., 1998). The experimental measurement of rear free surface velocity by VISAR (Tollier et al., 1998) is also shown in Figure 4.23. A very good agreement was obtained between the experimental data and simulation results in this case.

Table 4.4. Material properties of Al, Cu, and Ni (Tollier et al., 1998; Bolis et al., 2007).

Material	Al	Cu	Ni
ϱ_0 (kg/m^3)	2700	8930	8200
Y_0 (MPa)	300	120	1078
G (GPa)	26.2	46.8	79.2
γ	1.68	1.99	1.88
C_0	5386	3940	4119
S	1.34	1.49	1.8

The shock wave propagation in a 150-μm copper film was also calculated. In this case, the peak pressure applied is 4.3 GPa, which is much higher than the spall strength (2.6 GPa, Tollier et al., 1998). Therefore, a pull-back velocity peak can be observed in the plot (shown by a circle), which is an indication of spallation. The experimental measurement by Tollier et al. (Tollier et al., 1998) is also plotted in Figure 4.24, which shows a similar pull-back velocity peak. A very good agreement was also obtained between the experimental and simulation results in this case.

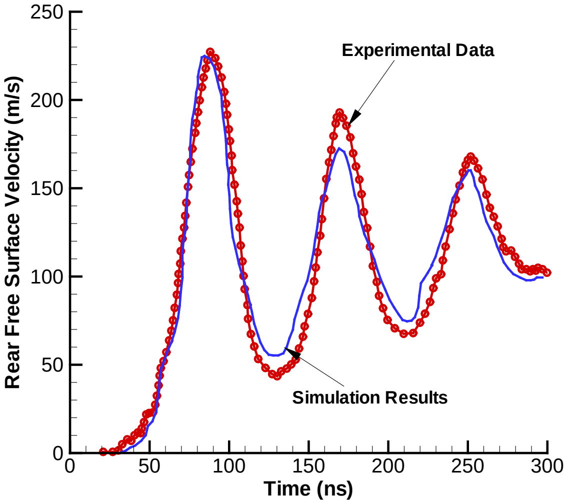

Figure 4.23. Comparison between experimental data (Tollier et al., 1998) and simulation results (250 μm Al foil, Gaussian pressure wave, P_{max} = 2.0 GPa, pulse duration 25 ns).

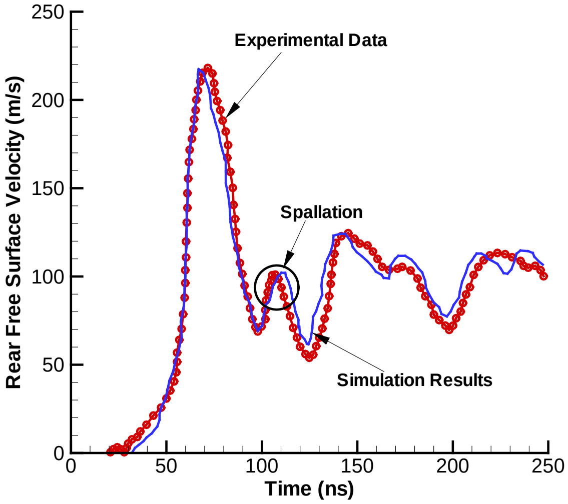

Figure 4.24. Comparison between experimental data (Tollier et al., 1998) and simulation results (150 μm Cu foil, Gaussian pressure wave, P_{max} = 4.3 GPa, pulse duration 25 ns).

4.2.4.2. Shock Wave Propagation in Double-Layered Target

Following the results shown in Bolis et al.'s (2007) work, a Cu/Ni system is chosen to calculate the stress evolution at the interface. The material properties used in the calculation are listed in Table 4.4. The thickness of the Cu layer and Ni layer is 119 and 88 μm, respectively. The pressure pulse used in the calculation is shown in Figure 4.25 and the peak pressure is 1.45 GPa. This pressure wave input is comparable to the pressure input used in (Bolis et al., 2007), which is generated by a laser power density of 79 GW/cm^2 in a direct regime.

The stress history at the Cu/Ni interface was calculated and shown in Figure 4.26. The simulation results by Bolis et al. (2007) were also shown in the plot for comparison. It can be seen that the incident shock wave and reflected shock wave from free surface were successfully captured by the current model. This case also demonstrates that the water confinement regime has the significant advantage over direct regime because it requires much less energy than the direct regime. The peak stress amplitude, however, shows some discrepancy, which is mostly due to the difference of the pressure input.

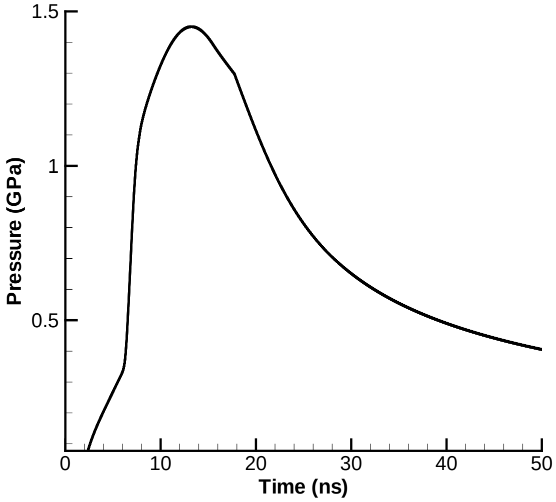

Figure 4.25. Pressure pulse history (Laser pulse duration 10 ns, wavelength 1064 nm, power density 1.1 GW/cm^2).

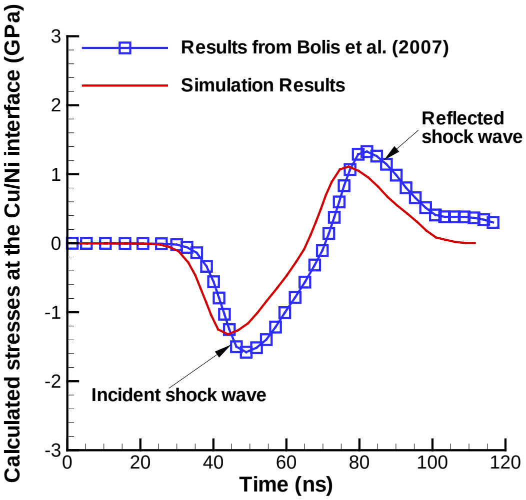

Figure 4.26. Calculated stress history at Cu/Ni interface.

4.2.4.3. Spallation Prediction

Case 1: Monolithic Aluminum Film

The void distribution can be calculated by using the continuous kinetic model presented in Section 4.2.2.4. Figure 4.27 (a) shows the void distribution of an Aluminum foil after a shock loading. The peak pressure of the shock wave is 2.8 GPa and the pulse duration is 25 ns. The calculation results indicate that the voids mainly form at the depth of around 150 μm. The maximum volume percentage of voids is only 2.2%, which is an indication of low level damage inside the foil. These predictions are consistent with the metallographical analysis conducted by Tollier et al. (1998) under the same conditions, as shown in Figure 4.27 (b).

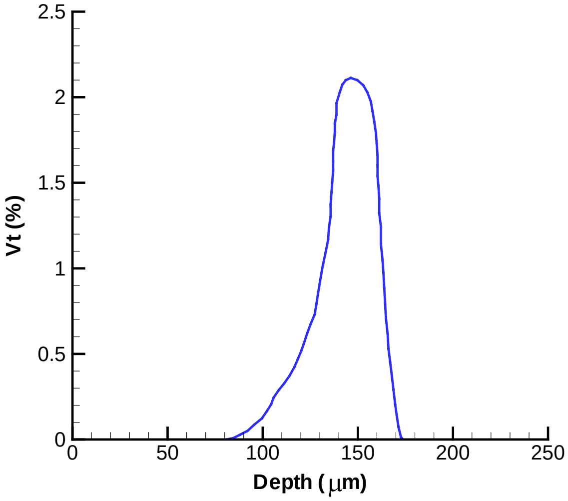

(a)

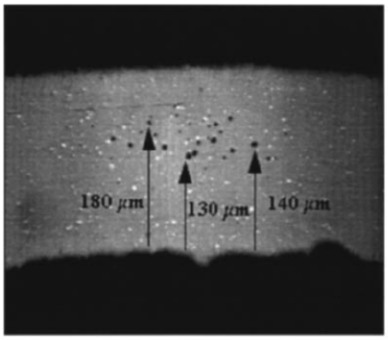

(b)

Figure 4.27. Comparison of experimental and simulation results on voids distribution (a) Simulation of voids distribution Metallographical analysis of 250-μm Al foil (Tollier et al., 1998) (250-μm Al foil, Gaussian pressure wave, P_{max} = 2.8 GPa, pulse duration 25 ns).

Case 2: Cu/Ni System with Low Pressure Loading

For a Cu/Ni system, the thickness of copper and nickel layer is 120 μm and 90 μm, respectively. The pressure loading is a Gaussian pressure wave with peak pressure 1.4 GPa, and the pulse duration of the pressure wave is 10 ns. Bolis et al.'s experiments (2007) with the above shock loading present almost no spallation either at the interface or inside the bulk material, as shown in Figure 4.28 (a).

The void distribution was calculated by using the continuous kinetic model with the yield strength effect considered by the Johnson-Cook constitutive equations. Figure 4.28 (b) shows the void distribution of a Cu/Ni (substrate/coating) system after the shock loading. It can be seen that the maximum volume percentage of voids is only 0.18%, which is an indication of negligible damage inside the substrate/coating system. Also the voids appear mainly around the depth of 90 μm, which is the interface location. Both of these predictions are confirmed again in the metallographical analysis, as seen in Figure 4.28 (a), which validates the numerical model developed in this work for shock wave propagation and spallation.

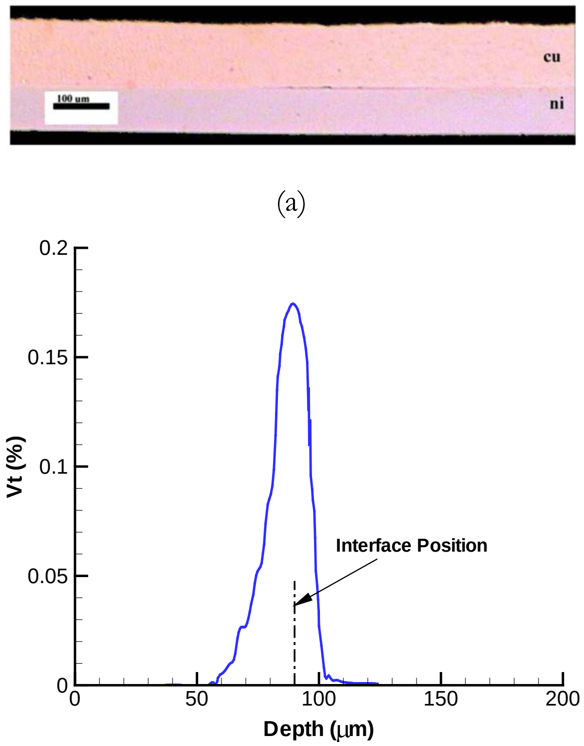

(a)

(b)

Figure 4.28. Comparison of experimental and simulation results on voids distribution (a) Experiment results after shock loading (Bolis et al., 2007) (b) Simulated void distribution in the depth direction (Cu/Ni system, Gaussian pressure wave, P_{max} = 1.4 GPa, pulse duration 10 ns).

Case 3: Cu/Ni System with High Pressure Loading

In this case, the pressure loading is still a Gaussian pressure wave but the peak pressure is increased to 3.7 GPa, and the pulse duration of the pressure wave is kept same as in the previous case. The thickness of copper and nickel layer is 180 μm and 90 μm, respectively. The cross-sectional image of the Cu/Ni system after the shock loading is shown in Figure 4.29 (a), where a spallation can be observed near the interface position.

The void distribution was also calculated and shown in Figure 4.29 (b). In this case, the maximum volume percentage of voids is as high as 7.5%, which is an indication of higher level of damage inside the substrate/coating system. The location of interface position is also shown in Figure 4.29 (b). The left side of the interface location is nickel layer with thickness of 90 μm, while the right side copper layer. It can be seen from Figure 4.29 (b) that the voids are mainly present around the interface position with more voids located in the copper layer, thus showing an excellent agreement with the experimental result. This case validates again the numerical model developed in this work.

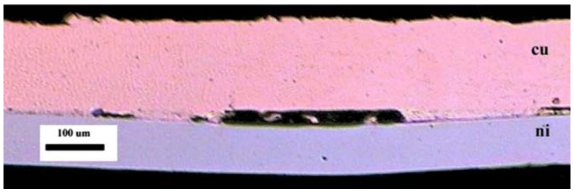

(a)

Figure 4.29. Comparison of experimental and simulation results on voids distribution (a) Experiment results after shock loading (Bolis et al., 2007) (b) Simulated void distribution in the depth direction (Cu/Ni system, Gaussian pressure wave, P_{max} = 3.7 GPa, pulse duration 10 ns).

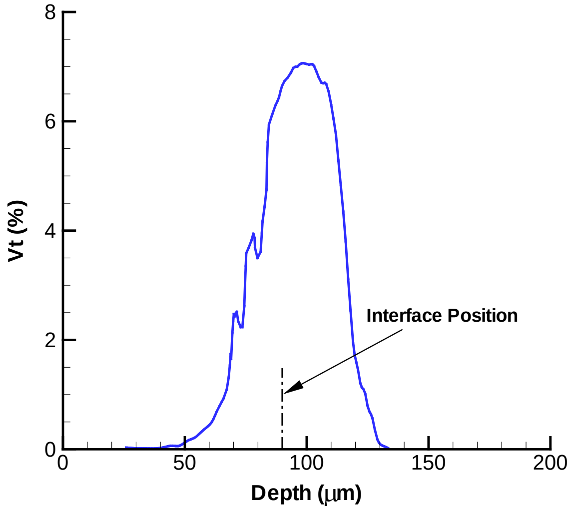

(b)

Figure 4.29. Continued.

4.2.5. Summary

This work presented a model that offers a more complete and general solution for shock wave propagation and spallation in the laser shock peening process. In addition to the pressure shock wave and its propagation inside the solid materials, the model is also capable of calculating the transient stress history at the interface and the rear free surface velocity. The spallation threshold and damage zone location were also calculated for aluminum film and Cu/Ni system with different thickness of foils and various laser shock peening parameters. Single layer aluminum film showed low level spallation inside the film under a Gaussian pressure wave with the magnitude of 2.8 GPa and the pulse duration of 25 ns. Cu/Ni system presented negligible and substantial spallation near the interface region under low (1.4 GPa) and high pressure (3.7 GPa) loading, respectively. Good agreement was obtained between experimental and simulation results for the void distribution for both single layer and double-layer targets.

CHAPTER 5. ETCHING BY NANOSECOND LASER INDUCED WATER BREAKDOWN PLASMA

5.1 Introduction

The thermal effects of plasma is investigated in this work. As reviewed in Chapter 1, direct laser ablation in low fluence range can also be used to ablate the polymer material only (Wolynski et al., 2011) by properly controlling the laser fluence. However, the laser beam could be blocked by the carbon fiber significantly in the direct ablation mode. As a result, only a very thin layer of polymer can be ablated. If high laser fluence were used by direct laser ablation, both the polymer matrix and the carbon fibers could be completely removed, which will significantly affect the material strength since the fibers were broken. Therefore, the thermal effects of laser-induced water breakdown plasma for selective etching of the polymer from the composite material are investigated.

The dependence of the etching depth on the laser power density, laser focus position, and the number of shots are also investigated in this work to obtain a maximum possible etching depth.

5.2 Experimental Procedures

The experimental setup used in this study is shown in Figure 5.1. A frequency-doubled Nd:YAG laser (wavelength of 532 nm) is used to generate a laser beam, which passes through a half-wave plate, polarizer, three high reflecting mirrors and a focus lens, and finally irradiates on the surface of workpiece. The laser beam profile is top-hat in spatial distribution and Gaussian in temporal distribution. The plano-convex focus lens has a focal length of 100 mm and a numerical aperture of 0.25. The laser beam is around 0.3 mm when in focus. The composite workpiece is placed into a water tank to produce a water-confinement regime, as shown in Figure 5.2. The water layer depth is around 10 mm above the surface of the workpiece, which is maintained in this level during the experiment. The movement of the workpiece in X and Y directions is controlled by two linear motion stages. The distance between the focus point and the surface of the workpiece can also be changed by vertically varying the position of the focal lens. With this setup, the laser power density can be easily adjusted by fine tuning the orientation of the half-wave plate.

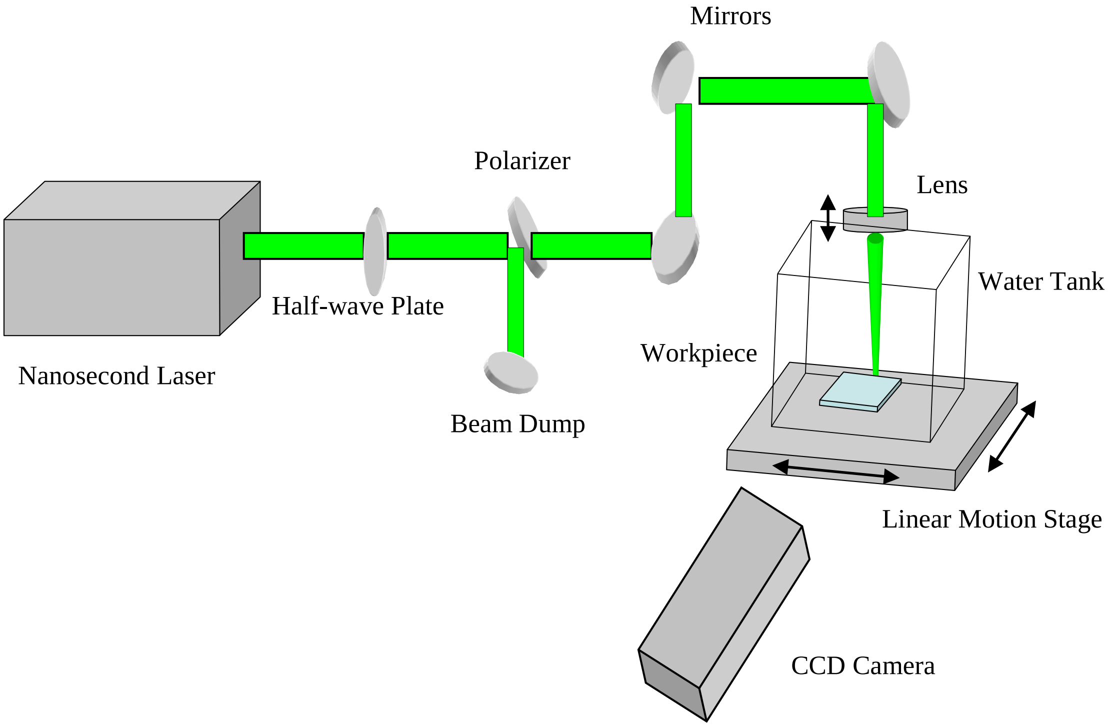

Figure 5.1. Experimental setup for plasma etching.

The laser induced water breakdown plasma is captured by the CCD camera. It should be noted that the plasma initially forms at the laser focal spot (dashed ellipse in Figure 5.2) if the laser power density at the focal spot just exceeds the breakdown threshold. If the laser power density is much higher than the water breakdown threshold, the laser power density at the air–water interface may be high enough to breakdown the water at the air–water interface. Therefore, the water breakdown plasma could be observed in any region from the focal spot (dashed ellipse in Figure 5.2) to the air–water interface (solid ellipse in Figure 5.2) depending on the laser power density.

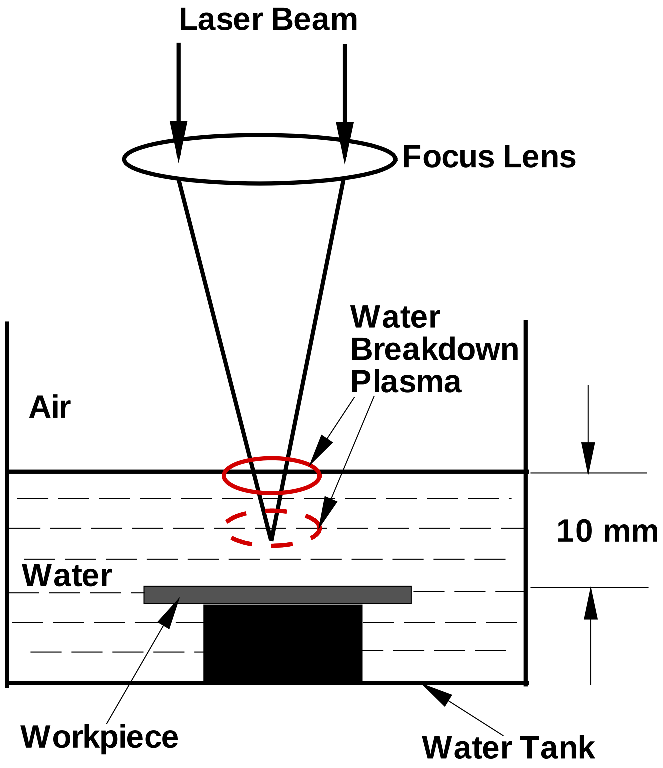

Figure 5.2. Close-up view of the air–water–workpiece system.

The composite sample used in this study is preimpregnated ("pre-preg") material. The polymer is epoxy resin and the carbon fiber is the intermediate modulus IM7. The sample thickness is around 3.4 mm.

A series of experiments of laser induced plasma etching were carried out to systemically investigate the etching behavior under the water breakdown plasma. According to Ref. (Sollier et al., 2001; Wu and Shin, 2006b; Feng et al., 1997), the water breakdown threshold for a 532 nm, 6 ns, around 300 μm laser beam is determined to be less than 30 GW/cm^2. In this work, the laser power density is chosen to be from 30 to 70 GW/cm^2. Therefore, the water breakdown will certainly occur under this condition, which will ensure the laser induced plasma etching operation. The experimental conditions are listed in Table 5.1.

Table 5.1. Experiment conditions for laser induced plasma etching.

	Laser Power Density (GW/cm^2)	Distance from Focus Point to Sample Surface (mm)	Number of Laser Shots
Experiment 1	30.0, 40.0, 50.0, 60.0, 70.0	3.0	1
Experiment 2	70.0	1.0, 3.0, 5.0, 7.0, 9.0	1
Experiment 3	70.0	3.0	1, 2, 10, 20, 50

After the nanosecond laser induced plasma etching operation, a picosecond laser is employed to cut the composite sample on the cross section. The picosecond laser cutting is chosen here because it can significantly reduce the heat affect zone compared with the traditional mechanical cutting and nanosecond laser cutting (Shannugam et al., 2002; Mo Naeem, 2008). A groove of 200 μm (width) × 120 μm (depth) was generated by the picosecond laser cutting near the center line of the etching area.

After the laser cutting, the sample was completely cut by a conventional mechanical cutter and then polished to obtain a relatively flat surface. The sample was further sputter-coated to be analyzed under the SEM. Figure 5.3 shows an SEM image of the center region of the cross-section of the composite sample after 50 laser shots. The carbon fibers can be clearly seen in this image. The polymers between the carbon fibers are completely removed by the water breakdown plasma.

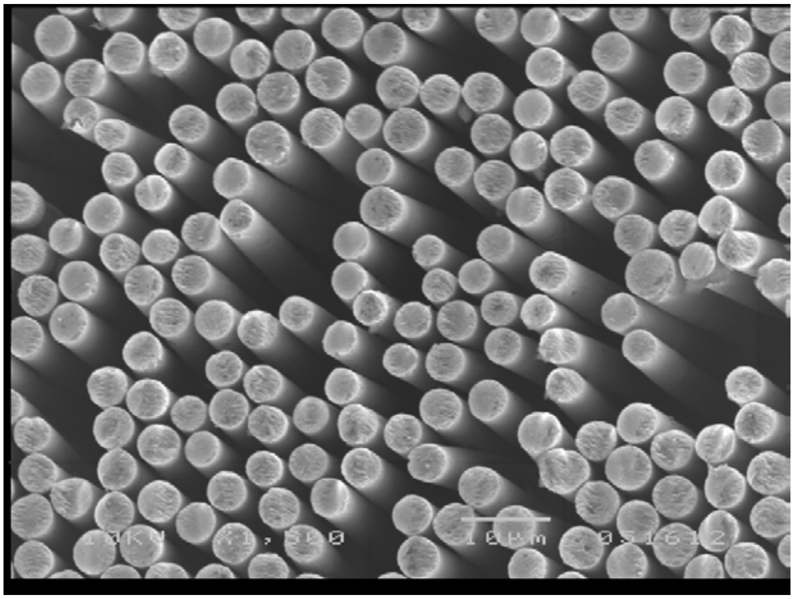

Figure 5.3. SEM image of the center region of the composite sample after 50 laser shots (laser power density 70.0 GW/cm^2, laser focus is 3.0 mm away from the target surface).

5.3 Results and Discussion

5.3.1 CCD Image of Water Breakdown Plasma

The CCD image of the water breakdown plasma was obtained, as shown in Figure 5.4. The laser power density used in this measurement is around 50 GW/cm^2. The water surface is marked with a solid line in Figure 5.4. Initially, air occupies the space above the water surface line while water is filled in the bottom half. It can be seen from Figure 5.4 that the water breakdown plasma occurs at the region close to the water surface. Around a half of the volume of the plasma is under the water. As discussed in Section 5.2, the water breakdown plasma could be observed at the air–water interface if the laser power density is much higher than the water breakdown threshold, which is the condition in this case. This observation was also reported by other researchers for the laser shock peening applications (Berthe et al., 1997).

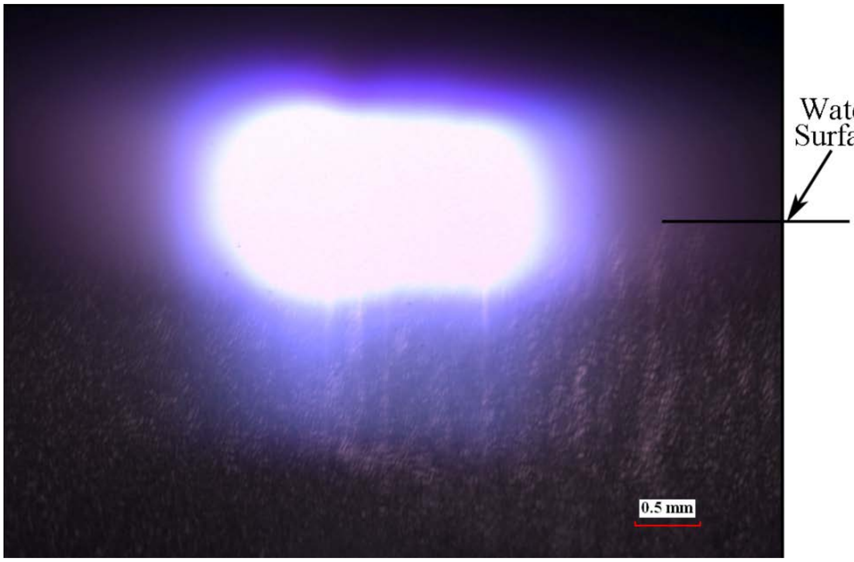

Figure 5.4. Water breakdown plasma observed during laser induced plasma etching operation (laser power density 50 GW/cm^2).

5.3.2 Effect of Laser Power Density

The effect of laser power density was first investigated by changing the laser power input from 30.0 GW/cm^2 to 70.0 GW/cm^2. It should be mentioned here that the experiments in this section were performed in single shots. The cross-sectional view of the crater is shown in Figure 5.5 for two different power densities. The etched layer is determined from the SEM image, where the polymer is completely removed by the laser induced water breakdown plasma while the carbon fibers remain intact. The dependence of the etching depth on the laser power density is plotted in Figure 5.6. Clearly, as shown in Figure 5.6, the etching depth increases linearly with the laser power density.

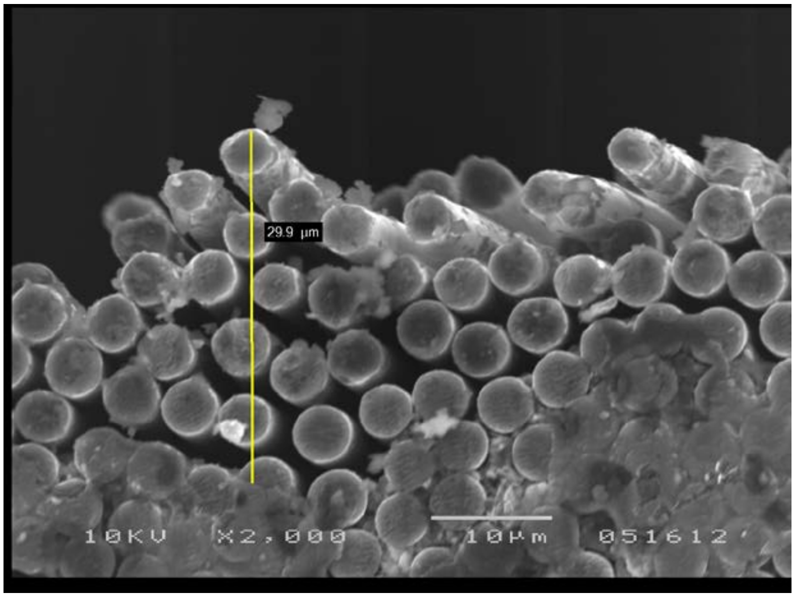

(a)

Figure 5.5. Cross-section view of the crater under different laser power densities (a) 40.0 GW/cm^2 (b) 50.0 GW/cm^2 (distance from the laser focus to the target surface is fixed at 3.0 mm).

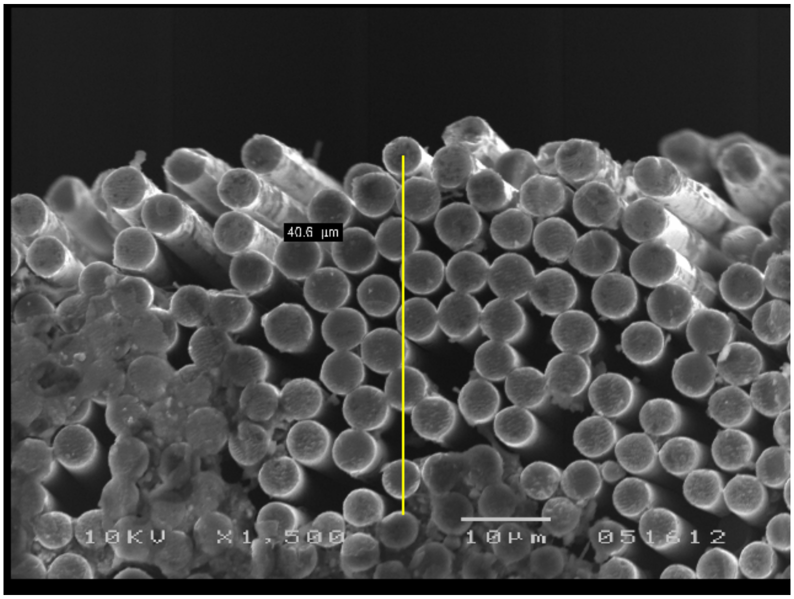

(b)

Figure 5.5. Continued.

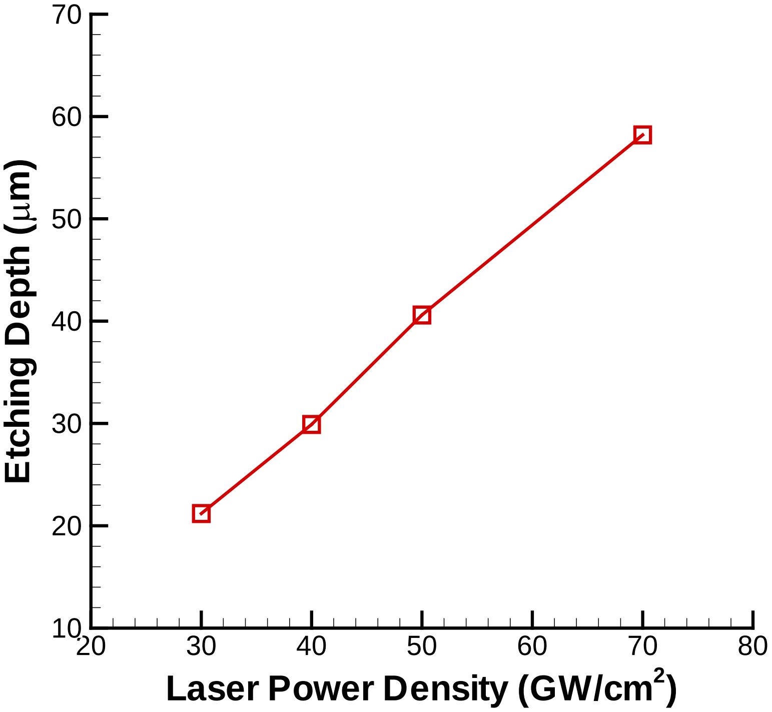

Figure 5.6. Etching depth dependence on the laser power density (laser focus 3.0 mm away from the target surface).

5.3.3 Effect of Laser Focus Position

The effect of laser focus position was also investigated by changing the distance between the laser focus position and the target surface from 1.0 mm to 9.0 mm. According to Figure 5.2, the laser focus position is still inside the water since the water layer depth is 10 mm. Due to the refractive index change at the air/water interface, the actual distance change should be around 1.33 mm to 12.0 mm. As indicated in Section 5.2, the plasma was observed at the air–water interface (solid ellipse in Figure 5.2). In this experiment, the laser power density was fixed at 70.0 GW/cm^2. The cross-sectional view of the crater is shown in Figure 5.6. In this figure, the blurred lower part is the polymer and carbon fiber which are not affected by the single shot laser etching. The blurred part was introduced during the sample polishing process where a small height difference is left between the unaffected region and the laser process region to avoid damaging the carbon fiber. The dependence of the etching depth on the laser focus position is plotted in Figure 5.8.

As expected, the etching depth decreases with the increase of the distance between the laser focus and the target surface. It should be mentioned that there were quite a lot of broken fibers shown in the crater region when the laser focus is 1.0 mm away from the target surface, probably due to the very high energy input to the composite target, which not only evaporates the polymer but also ablates the carbon fiber. The broken fibers can be clearly seen in Figure 5.9. For the distance larger than 3.0 mm, no significant amount of broken fibers appears in the crater. Therefore, in the subsequent multi-shot experiments, the distance between the laser focus and the target surface was maintained at 3.0 mm to obtain the maximum possible crater depth without fiber damage.

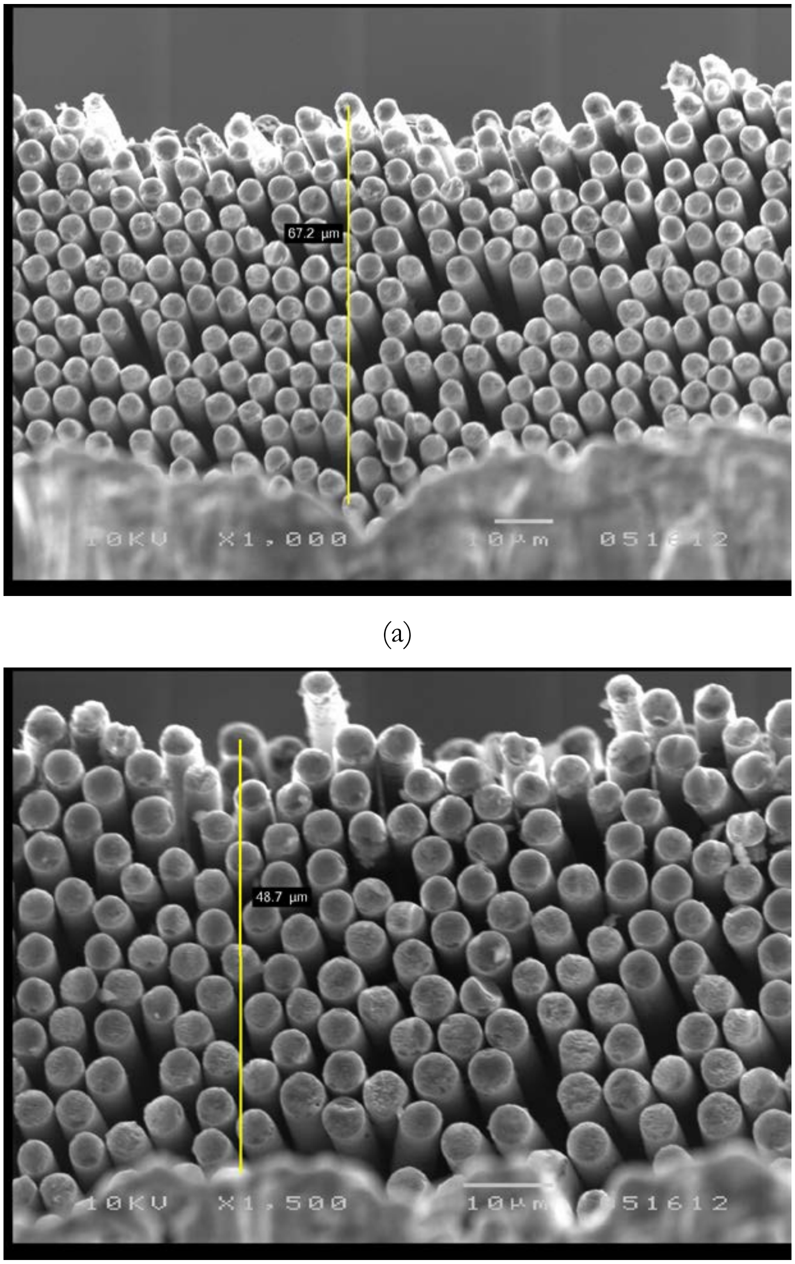

(a)

(b)

Figure 5.7. Cross-section view of crater for different distances from the laser focus to target surface (a) 1.0 mm (b) 5.0 mm (laser power density 70 GW/cm^2).

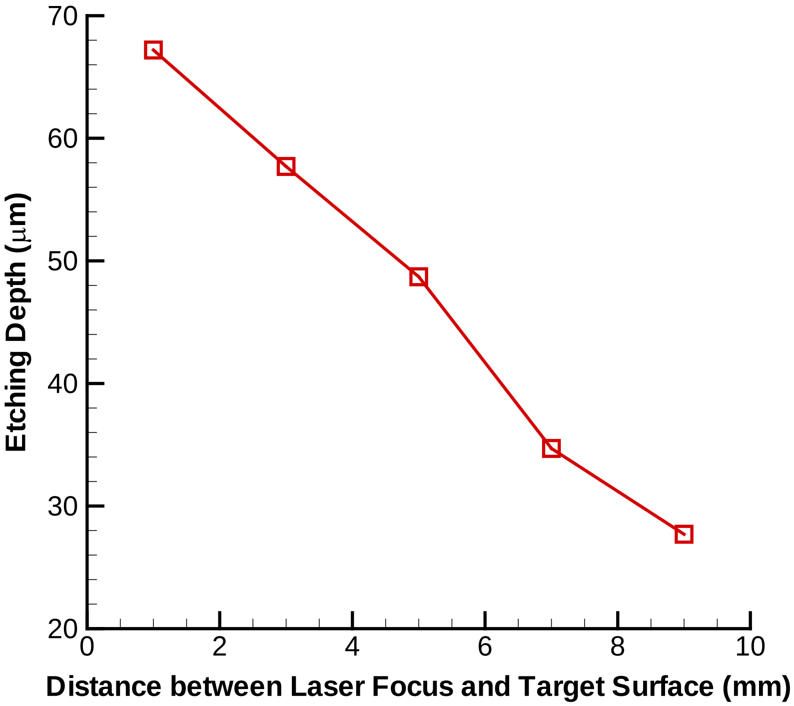

Figure 5.8. Dependence of etching depth on the distance between laser focus and target surface (laser power density 70 GW/cm^2).

Figure 5.9. Broken fibers in the crater region (laser focus 1.0 mm away from target).

5.3.4 Effect of Multi-Shot Etching

Based on the previous two experiments, the best combination of the laser power density and distance between laser focus and target surface is chosen to be 70.0 GW/cm^2 and 3.0 mm in order to obtain maximum possible crater depth. The multi-shot effect was then investigated by irradiating the same spot with different pulse numbers. Figure 5.10 shows the two SEM images of the craters formed by multiple laser shots. The dependence of the etching depth on the pulse number is shown in Figure 5.11.

As expected, the etching depth increases with the pulse number. The maximum depth can be as high as 350 μm with 50 laser shots. Clearly, the increase is not significant with the pulse number increasing from 20 to 50, which indicates that the maximum etching depth is around 350 μm even if more laser shots are employed.

This saturation behavior is due to the fact that there is a limit for the plasma expansion and plasma energy radiation into the composite material. With the increase of the etching depth, more carbon fibers will appear in the plasma expansion path, which will have strong interaction with the plasma and absorb the plasma energy. Therefore, the plasma cannot propagate into the composite material very deep. The maximum etching depth is found to be around 350 μm under the experimental conditions in this work.

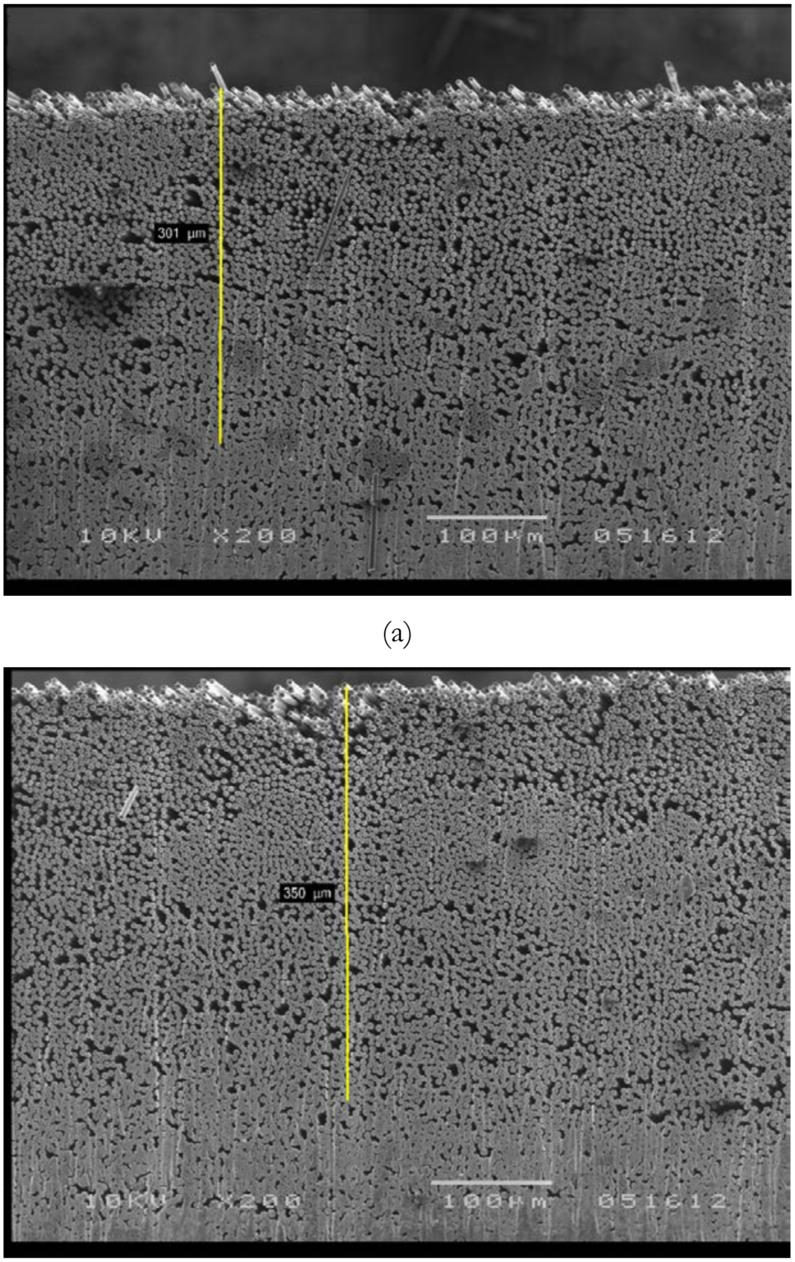

(a)

(b)

Figure 5.10. SEM images of crater after multiple laser shots (a) 20 shots (b) 50 shots (laser power density 70 GW/cm^2, laser focus 3.0 mm away from the target surface).

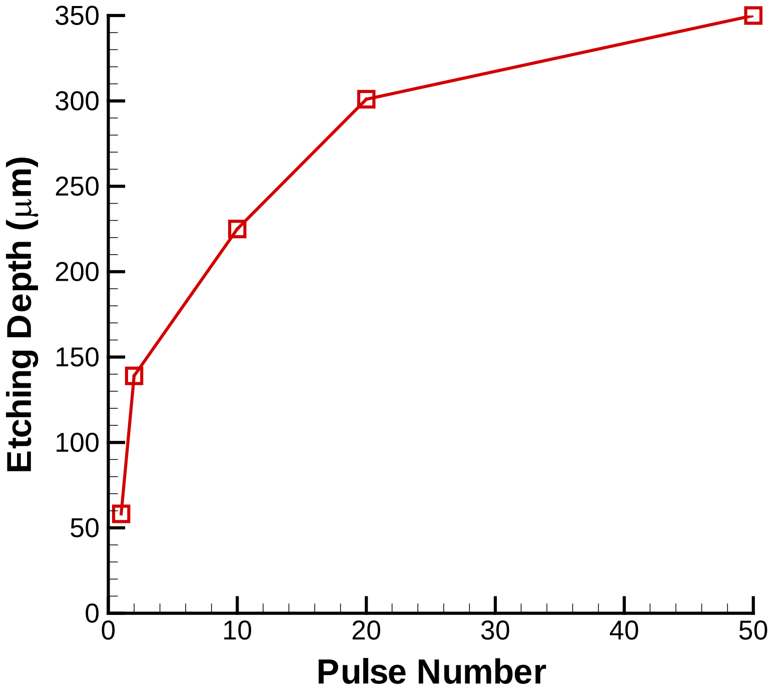

Figure 5.11. Etching depth dependence on the pulse number (laser power density 70 GW/cm^2, laser focus 3.0 mm away from the target surface).

5.4 Summary

Water breakdown plasma was used in this work to etch the surface layer of a carbon fiber reinforced composite sample. It is found that the polymer layer can be effectively removed by the plasma while the carbon fiber remains almost intact. The dependence of the etching depth on the laser power density, laser focus position, and the number of shots were also investigated in this work. The maximum etching depth is around 350 μm with 50 laser shots at laser power density of 70 GW/cm^2.

The etching method proposed in this work could be used in the laser-based repair of composite material. By controlling the laser parameters, layer-by-layer etching of the polymer can be accomplished. This process has great potential in the aerospace industry where more and more composite materials are used.

CHAPTER 6. CONCLUSIONS AND FUTURE WORK

This chapter summarizes the conclusions in this nanosecond laser matter interaction research, as well as proposed future study directions.

6.1 Conclusions

Nanosecond laser ablation of metal targets in air and water was investigated through a self-contained hydrodynamic model under different laser fluences involving no-phase explosion and phase explosion. The predicted ablation depths agreed well with the literature data and experiments. A sharp increase in ablation rate is observed for nanosecond laser ablation of aluminum at around 10 J/cm^2 with the occurrence of phase explosion for a 1064 nm, 10 ns laser pulse. The ablation depth is found to be nearly independent of the laser pulse duration, while it decreases with the increase of laser wavelength. Deeper crater depths in water found in all the conditions studied in this work are due to the high-magnitude shock compression.

Nanosecond laser ablation of aluminum and copper with phase explosion was investigated through a multi-scale model and experimental verification. The model prediction of the melt ejection behavior agrees well with the experimental observation in terms of the phase explosion starting time, particle expansion characteristics, and ablation depth. The commonly used ablation depth prediction criterion of 0.9 T_c is found to be not correct for copper when phase explosion is involved, while it is reasonable for aluminum. In the cases considered in this work, 0.75 ~ 0.8 T_c is found to be a better criterion for copper. The model developed in this work has been shown to provide better capability of predicting the ablation depth and the associated ablation behavior with phase explosion.

A 3-D finite element model with a confined plasma model has been developed and used to simulate the LSP process. By using these combined models, the indentation depth and residual stresses could be accurately calculated under different LSP conditions. Single shot, single-track overlapping, multi-track overlapping LSP experiments have been performed on various metals under different LSP conditions. The model prediction of indentation profiles and residual stresses in the depth direction provided good agreement with experimental data. It was found that higher laser power density can increase not only the peak residual stress but compressive zone depth. The overlapping ratio contributed to the peak residual stress while showing almost no effect on the compressive zone depth. Longer laser pulse resulted in larger compressive zone depths. Stress relaxation effect was also observed in overlapping LSP process.

This work presented a model that offers a more complete and general solution for shock wave propagation and spallation in the laser shock peening process. In addition to the pressure shock wave and its propagation inside the solid materials, the model is also capable of calculating the transient stress history at the interface and the rear free surface velocity. The spallation threshold and damage zone location were also calculated for aluminum film and Cu/Ni system with different thickness of foils and various laser shock peening parameters. Single layer aluminum film showed low level spallation inside the film under a Gaussian pressure wave with the magnitude of 2.8 GPa and the pulse duration of 25 ns.

Cu/Ni system presented negligible and substantial spallation near the interface region under low (1.4 GPa) and high pressure (3.7 GPa) loading, respectively. Good agreement was obtained between experimental and simulation results for the void distribution for both single layer and double-layer targets.

Water breakdown plasma was used in this work to etch the surface layer of a carbon fiber reinforced composite sample. It is found that the polymer layer can be effectively removed by the plasma while the carbon fiber remains almost intact. The dependence of the etching depth on the laser power density, laser focus position, and the number of shots were also investigated in this work. The maximum etching depth is around 350 μm with 50 laser shots at laser power density of 70 GW/cm^2. The etching method proposed in this work could be used in the laser-based repair of composite material. By controlling the laser parameters, layer-by-layer etching of the polymer can be accomplished. This process has great potential in the aerospace industry where more and more composite materials are used.

6.2 Recommendations for Future Work

Based on the current studies, several subjects are proposed for the future work:

1) Multi-shot laser ablation. With the correct prediction of melt ejection behavior in the single shot laser ablation, the structural change introduced by the laser ablation process can be obtained, which could be used to investigate the multi-pulse laser ablation process. This multi-shot ablation process is of significant importance since it can give more insights into the overlapping laser shock peening process discussed in Chapter 3.

2) Theoretical modeling of plasma etching process. As discussed in Chapter 4, the etching by the laser induced water breakdown plasma starts with laser-water interaction and

then becomes a thermal-kinetic process, which can be explained by the plasma-matter interaction (Pallav et al., 2011). Therefore, the plasma etching process can be modeled as a three-stage process: Water breakdown plasma formation; Water breakdown plasma expansion; and then material removal due to plasma-matter interaction. This theoretical model could provide better understanding of the thermal effect of the water breakdown plasma.

3) Double-pulse laser ablation. With the experimental setup discussed in Chapter 5, the nanosecond and picosecond laser beams could be easily combined together to enhance the ablation efficiency. Also due to the localized ablation of picosecond laser, a cleaner, sharper crater could be generated with this double-pulse technique.

LIST OF REFERENCES

LIST OF REFERENCES

ABAQUS documentation, Version 6.6, 2006, Hibbitt, Karlsson & Sorensen, Inc., Pawtucket, RI.

Allen, M.P., and Tildesley, D.J., 1989, Computer Simulation of Liquids, Clarendon Press, New York.

Amoruso, S., Bruzzese, R., Vitiello, M., Nedialkov, N.N., and Atanasov, P.A., 2005, "Experimental and Theoretical Investigations of Femtosecond Laser Ablation of Aluminum in Vacuum", Journal of Applied Physics, 98, 044097.

Ang L.K., Lau Y.Y., Gilgenbach R.M., Spindler H.L., 1997, "Analysis of Laser Absorption on a Rough Metal Surface", Applied Physics Letters, 70 (6), pp. 696-698.

Anisimov, S.I., Bauerle, D., and Luk'yanchuk, B.S., 1993, "Gas Dynamics and Film Profiles in Pulsed-laser Deposition of Materials", Physical Review B, 48(16), pp. 12076-12081.

Anisimov, S.I., Luk'yanchuk, B.S., and Luches, A., 1996, "An Analytical Model for Three Dimensional Laser Plume Expansion into Vacuum in Hydrodynamic Regime", Applied Surface Science, 96-98, pp. 24-32.

Antoun, T., Seaman, L., Curran, D.R., Kanel, G.I., Razorenov, S.V., and Utkin, A.V., 2003, Spall Fracture, Springer-Verlag, New York, Chap. 2, Chap. 6.

Armstrong, K.B., 1997, "Repair of Composite Structures", International Journal for the Joining of Materials, 9 (4), pp. 130-137.

Ashkenasi, D., Lorenz, M., Stoian, R., and Rosenfeld, A., 1999, "Surface Damage Threshold and Structuring of Dielectrics Using Femtosecond Laser Pulses: the Role of Incubation", Applied Surface Science, 150 (1-4), pp. 101-106.

ASM Handbook, Vol. 9, Chemical and Electrolytic Polishing, Metallography and Microstructures, ASM International, 2004, pp. 281-293.

Auroux, E., Boustie, M., Romain, J.P., Bertheau, D., Peyre, P., Berthe, L., Bartnicki, E., 2001, "Debonding Study of Ni-base Substrate/Pt Coatings Interfaces Using Laser Shock Waves: Characterization of the Targets and Experimental Study", Surface and Coatings Technology, 138, pp. 269-277.

Autrique, D., Chen, Z., Alexiades, V., Bogaerts, A., and Rethfeld, B., 2012, "A Multiphase Model for Pulsed ns-laser Ablation of Copper in an Ambient Gas", AIP Conference Proceedings, 1464, pp. 648-659.

Baskes, M.I., 1992, "Modified Embedded-atom Potentials for Cubic Materials and Impurities", Physical Review B, 46, pp. 2727-2742.

Becker, M.F., Brock, J.R., Cai, H., Henneke, D.E., Keto, J.W., Lee, J., Nichols, W.T., Glicksman, H.D., 1998, "Metal Nanoparticles Generated by Laser Ablation", Nanostructured Materials, 10, pp. 853-863.

Benedict, L.X., Klepeis, J.E., and Streitz, F.H., 2005, "Calculation of Optical Absorption in Al across the Solid-to liquid Transition", Physical Review B, 71, 064103.

Bennett, H.E., Bennett, J.M., Ashley, E.J., Motyka, R.H., 1968, "Verification of the Anomalous-Skin-Effect Theory for Silver in the Infrared", Physical Review, 165, pp. 755-765.

Bennett, T.D., Grigoropoulos, C.P., Krajnovich, D.J., 1995, "Near Threshold Laser Sputtering of Gold", Journal of Applied Physics, 77, pp. 849-864.

Bergstrom, D., 2008, "The Absorption of Laser Light by Rough Metal Surfaces", Doctoral Thesis, Lulea University of Technology, Sweden.

Berthe, L., Fabbro, R., Peyre, P., Tollier, L., and Bartnicki, E., 1997, "Shock Waves from A Water-confined Laser-generated Plasma", Journal of Applied Physics, 82 (6), pp. 2826-2832.

Berthe, L., Fabbro, R., Peyre, P., and Bartnicki, E., 1998, "Experimental Study of the Transmission of Breakdown Plasma Generated during Laser Shock Processing", The European Physical Journal Applied Physics, 3, pp. 215-218.

Berthe, L., Fabbro, R., Peyre, P., and Bartnicki, E., 1999, "Wavelength Dependent of Laser Shock-wave Generation in the Water-confinement Regime", Journal of Applied Physics, 85 (11), pp. 7552-7555.

Bhatt, D., Jasper, A.W., Schultz, N.E., Siepmann, J.I., and Truhlar, D.G., 2006, "Critical Properties of Aluminum", Journal of the American Chemical Society, 128, pp. 4224-4225.

Blair, D., Tillack, M., Zaghloul, M., 2001, "Prediction of Particulate Characteristics in An Expanding Laser Plume", SPIE Conference on Micromachining and Microfabrication, San Francisco, CA, October 2001, Vol. 4557, pp. 139-150.

Bogaerts, A., Chen, Z., Gigbels, R., and Vertes, A., 2003, "Laser Ablation for Analytical Sampling: What Can We Learn from Modeling?", Spectrochimica Acta Part B: Atomic Spectroscopy, 58, pp. 1867-1893.

Bolis, C., Berthe, L., Boustie, M., Arrigoni, M., Barradas, S., and Jeandin, M., 2007, "Physical Approach to Adhesion Testing Using Laser-driven Shock Waves", Journal of Physics D: Applied Physics, 40, pp.3155-3163.

Borsenberger, P.M., and Weiss, D.S., 1998, Organic Photoreceptors for Xerography, CRC Press, pp. 437-438.

Brailovsky, A.B., Gaponov, S.V., Luchin, V.I., 1995, "Mechanisms of Melt Droplets and Solid Particle Ejection from A Target Surface by Pulsed Laser Action", Applied Physics A, 61, pp. 81-86.

Braisted, W., and Brockman, R., 1999, "Finite Element Simulation of Laser Shock Peening", International Journal of Fatigue, 21, pp. 719-724.

Cahill, J.A. and Kirshenbaum, A.D., 1962, "The Density of Liquid Copper from Its Melting Point (1356 ºK) to 2500 ºK and an Estimation of Its Critical Constants", Journal of Physical Chemistry, 66 (6), pp. 1080-1082.

Cao, Y., Shin, Y.C. and Wu, B., 2010, "A Parametric Study on Overlapping Laser Shock Peening of 4140 Steel via Modeling and Experiments", Trans. of the ASME, Journal of Manufacturing Science and Engineering, 132 (6), 061010.

Cao, Y., Zhao, X., and Shin, Y.C., 2013, "Analysis of Nanosecond Laser Ablation of Aluminum with and without Phase Explosion in Air and Water", Journal of Laser Applications, 25 (3), 032002.

Chai, H., 2003, "Fracture Mechanics Analysis of Thin Coatings under Plane-strain Indentation", International Journal of Solids and Structures, 40, pp. 591-610.

Charles, S.M., Tao, W., Lin, T., Graham, C., and Mai, Y.W., 2002, "Laser Shock Processing and Its Effect on Microstructure and Properties of Metal Alloys: A Review", International Journal of Fatigue, 24, pp. 1021-1036.

Chen, Z., Bogaerts, A., and Vertes, A., 2006, "Phase Explosion in Atmospheric Pressure Infrared Laser Ablation from Water-rich Targets", Applied Physics Letters, 89, 041503.

Cheng, C. And Xu, X., 2007, "Molecular Dynamics Calculation of Critical Point of Nickel", International Journal of Thermophysics, 28 (1), pp. 9-19.

Colina, M., Molpeceres, C., Morales, M., Allens-Perkins, F., Guadano, G., and Ocana, J.L., 2011, "Laser Ablation Modeling of Aluminum, Silver and Crystalline Silicon for Applications in Photovoltaic Technologies", Surface Engineering, 27 (6), pp. 414-423.

Cottet, F., and Boustie, M., 1989, “Spallation Studies in Aluminum Targets Using Shock Waves Induced in Laser Irradiation at Various Pulse Durations”, Journal of Applied Physics, 66 (9), pp. 4067-4063.

Davison, L., 2008, Fundamentals of Shock Wave Propagation in Solids, Springer-Verlag, Berlin, Chap. 2-4.

Ding, K., and Ye, L., 2003a, “FEM Simulation of Two Sided Laser Shock Peening of Thin Sections of Ti-6Al-4V Alloy,” Surface Engineering, 19 (2), pp. 127-133.

Ding, K., and Ye, L., 2003b, “Three-Dimensional Dynamic Finite Element Analysis of Multiple Laser Shock Peening Processes,” Surface Engineering, 19 (5), pp. 351-358.

Domer, H., Bostanjoglo, O., 2003, “Phase Explosion in Laser-pulsed Metal Films”, Applied Surface Science, 208-209, pp. 442-446.

Dorman, M., Toparli, M.B., Smyth, N., Cini, A., Fitzpatrick, M. E., and Irving, P. E., 2012, “Effect of Laser Shock Peening on Residual Stress and Fatigue Life of Clad 2024 Aluminum Sheet Containing Scribe Defects”, Materials Science and Engineering: A, 548 pp. 142-151.

Dupont, A., Caminat, P., Bournot, P., and Gauchon, J.P., 1995, "Enhancement of Material Ablation Using 248, 308, 532, 1064 nm Laser Pulse with A Water Film on the Treated Surface", Journal of Applied Physics, 78 (3), pp. 2022-2028.

Ehrenreigh, H., Philipp, H.R., and Segall, B., 1963, “Optical Properties of Aluminum”, Physical Review, 132 (5), pp. 1918-1928.

Fabbro, R., Fournier, J., Ballard, P., Devaux, D., and Virmont, J., 1990, “Physical Study of Laser-produced Plasma in Confined Geometry”, Journal of Applied Physics, 68 (2), pp. 775-784.

Fan, Y., Wang, Y., Vukelic, S., and Yao, Y.L., 2005, “Wave-solid Interactions in Laser-shock-Induced Deformation Processes”, Journal of. Applied Physics, 98, 104904.

Feng, Q., Moloney, J.V., Newell, A.C., Wright, E.M., Cook, K., Kennedy, P.K., Hammer, D.X., Rockwell, B.A., and Thompson, C.R., 1997, “Theory and Simulation on the Threshold of Water Breakdown Induced by Focused Ultrashort Laser Pulses”, IEEE Journal of Quantum Electronics, 33 (2), pp. 127-137.

Fishburn, J.M., Mildren, R.P., Kaptian, D., Withford., M.J., Brown, D.J., and Piper, J.A., 2000, “Exploring the Explosive Ablation Regime of Metals in Nanosecond Micromachining”, Proceedings of SPIE, 3885, pp. 453-460.

Fishburn, J.M., Coutts, D.W., Withford, M.J., and Piper, J.A., 2001, "Phase Explosion Thresholds in Metals Ablated under Pulsed Nanosecond Radiation", Proceedings of the Australasian Conference on Optics, Lasers and Spectroscopy, Dec. 3-6, 2001, University of Queensland, Brisbane, Australia, pp. 127.

Fischer, F., Romoli, L., and Kling, R., 2010, "Laser-based Repair of Carbon Fiber Reinforced Plastics", CIRP Annals - Manufacturing Technology, 59, pp. 203-206.

Foiles, S.M., Baskes, M.I., and Daw, M.S., 1986, "Embedded-atom-method Functions for the Fcc Metals Cu, Ag, Au, Ni, Pd, Pt, and Their Alloys", Physical Review B, 33 (12), pp. 7983-7991.

Fortov, V.E., and Kostin, V.V., 1991, "Spallation of Metals under Laser Irradiation", Journal of Applied Physics, 70 (8), pp. 4524-4531.

Ganzenmuller, G.C, Steinhauser, M.O., and Liedekerke, P.V., 2011, "The Implementation of Smoothed Particle Hydrodynamics in LAMMPS", Retrieved from http://lammps.sandia.gov/doc/USER/sph/SPH_LAMMPS_userguide.pdf.

Gnedovets, A.G., Gusarov, A.V., Smurov, I., 1999, "A Model for Nanoparticle Synthesis by Pulsed Laser Evaporation", Journal of Physics D: Applied Physics, 32, pp. 2162-2168.

Gnedovets, A.G., Gusarov, A.V., Smurov, I., 2000, "Submicron Particles Synthesis by Laser Evaporation at Low Power Density: A Numerical Analysis", Applied Surface Science, 154–155, pp. 508-513

Gragossian, A., Tavassoli, S.H., and Shokri, B., 2009, "Laser Ablation of Aluminum from Normal Evaporation to Phase Explosion", Journal of Applied Physics, 105, 103304.

Gristoforetti, G., Legnaioli, S., Palleschi, V., Tognoni, E., and Benedetti, P.A., 2008, "Observation of Different Mass Removal Regimes during the Laser Ablation of an Aluminum Target in Air", Journal of Analytical Atomic Spectrometry, 23, pp. 1518-1528.

Gupta, V., Yuan, J., and Pronin, A., 1994, "Recent Developments in the Laser Spallation Technique to Measure the Interface Strength and Its Relationship to Interface Toughness with Applications to Metal/Ceramic, Ceramic/Ceramic and Ceramic/Polymer Interfaces", Journal of Adhesion Science and Technology, 8 (6), pp. 713-747.

Gusarov, A.V., Gnedovets, A.G., Smurov, I., Flamant, G., 2000, "Simulation of Nanoscale Particles Elaboration in Laser-produced Erosive Flow", Applied Surface Science, 154–155, pp. 331-336.

Gusarov, A.V., and Smurov, I., 2003, "Near-surface Laser-vapour Coupling in Nanosecond Pulsed Laser Ablation", Journal of Physics D: Applied Physics, 36 (23), pp. 2962-2971.

Hergenroder, R., 2006, “Hydrodynamic Sputtering as a Possible Source for Fractionation in LA-ICP-MS”, Journal of Analytical Atomic Spectrometry, 21, pp. 517-524.

Hess, H., 1998, “Critical Data and Vapor Pressures of Aluminum and Copper”, Zeitschrift fur Metallkunde, 89, pp. 388-393.

Hill, M.R., DeWald, A.T., Rankin, J.E., and Lee, M.J., 2005, “Measurement of Laser Peening Residual Stresses”, Material Science and Technology, 21 (1), pp. 3-9.

Horvat, D., Petkowsek, R., and Mozina, J., 2010, “Optodynamic Observation of Double Laser-induced Breakdown at the Water Surface”, Measurement Science and Technology, 21, 035301.

http://lammps.sandia.gov.

http://www.efunda.com/materials/elements/element_info.cfm?Element_ID=Cu.

http://www.matweb.com.

Hu, W., Shin, Y.C., and King, G., 2010, “Energy Transport Analysis in Ultrashort Pulse Laser Ablation through Combined Molecular Dynamics and Monte Carlo Simulation”, Physical Review B, 82, 094111.

Hu, Y. and Yao, Z., 2008, “Overlapping Rate Effect on Laser Shock Processing of 1045 Steel by Small Spots with Nd:YAG Pulsed Laser”, Surface and Coatings Technology, 202 (8), pp. 1517-1525.

Hull, D. and Clyne, T.W., 1996, “An Introduction to Composite Materials”, Cambridge University Press, Chapter 1.

Johnson, G.R., and Cook, W.H., 1983, “A Constitutive Model and Data for Metals Subjected to Large Strains, High Strain Rates and High Temperatures”, Proceedings of 7th International Symposium on Ballistics, Hague, Netherlands, pp. 541-547.

Kanel, G.I., Razorenov, S.V., Fortov, V.E., 2004, Shock-Wave Phenomena and the Properties of Condensed Matter, Springer-Verlag, New York.

Kang, H.W., Lee, H., Chen, S., and Welch, A.J., 2006, “Enhancement of Bovine Bone Ablation Assisted by a Transparent Liquid Layer on a Target Surface”, IEEE Journal of Quantum Electronics, 42 (7), pp. 633-642.

Kang, H.W., Lee, H, and Welch, A.J., 2008, “Laser Ablation in a Liquid-confined Environment Using a Nanosecond Laser Pulse”, Journal of Applied Physics, 103 (8), 083101.

Kar, A. and Mazumder, J., 1994, "Mathematical Model for Laser Ablation to Generate Nanoscale and Submicrometer-size Particles", Physical Review E, 19, pp. 410-419.

Kelly, R. and Miotello, A., 1996, "Comments on Explosive Mechanisms of Laser Sputtering", Applied Surface Science, 96-98, pp. 205-215.

Kim, D. and Lee, H., 2001, "Enhanced Ablation and Photoacoustic Excitation in Near-threshold Laser Ablation of Liquid-coated Surfaces", Journal of Applied Physics, 89 (10), pp. 5703-5706.

Kudryashov, S.I. and Zvorykin, V.D., 2008, "Microscale Nanosecond Laser-induced Optical Breakdown in Water", Physical Review E, 78, 036404.

Laville, S., Vidal, F., Johnston, T.W., Barthelemy, O., Chaker, M., Le Drogoff, B., Margot, J., and Sabsabi, M., 2002, "Fluid Modeling of the Laser Ablation Depth as a Function of the Pulse Duration for Conductors", Physical Review E, 66, 066415.

Linhart, A., Chen, C., Vrabec, J., and Hasse, H., 2005, "Thermal Properties of the Metastable Supersaturated Vapor of the Lennard-Jones Fluid", The Journal of Chemical Physics, 122, 144506.

Liu, C., Mao, X., Mao, S., Zeng, X., Greif, R., and Russo, R.E., 2004, "Nanosecond and Femtosecond Laser Ablation of Brass: Particulate and ICPMS Measurements", Analytical Chemistry, 76 (2), pp. 379-383.

Liu, C., Mao, X., Mao, S., Greif, R., and Russo, R.E., 2005, "Particle Size Dependent Chemistry from Laser Ablation of Brass", Analytical Chemistry, 77 (20), pp. 6687-6691.

Liu, X. and Osher, S., 1998, "Convex ENO High Order Multi-dimensional Schemes without Field by Field Decomposition or Staggered Grids", Journal of Computational Physics, 142 (2), pp. 304-330.

Lu, Q., 2003, "Thermodynamic Evolution of Phase Explosion during High-power Nanosecond Laser Ablation", Physical Review E, 67, 016410.

Lu, Q., Mao, S., Mao, X., and Russo, R.E., 2002, "Delayed Phase Explosion during High-power Nanosecond Laser Ablation of Silicon", Applied Physics Letters, 80, pp. 3072-3074.

Mahdieh, M.H., Nikbakht, M., Moghadam, Z.E., and Sobhani, M., 2010, "Crater Geometry Characterization of Al Targets Irradiated by Single Pulse and Pulse Trains of Nd:YAG Laser in Ambient Air and Water", Applied Surface Science, 256, pp. 1778-1783.

Manenti, A., 2009, "A Smoothed Particle Hydrodynamics: Basics and Applications", Retrieved from http://www-2.unipv.it/compmech/seminars/manenti-pres.pdf.

Mariella, R., Rubenchik, A., Norton, M., Donohue, G., Roberts, K., 2010, "Laser-matter Interaction with Submerged Samples", LLNL Technical Report, 427603.

Martynyuk, M.M., 1977a, "The Critical Parameters of Metals I, Critical Temperature", Russian Journal of Physical Chemistry, 51, 705-706.

Martynyuk, M.M., 1977b, "Phase Explosion of a Metastable Fluid", Combustion, Explosion and Shock Waves, 13 (2), pp. 178-191.

Martyuyuk, M.M., 1983, "Critical Constants of Metals", Russian Journal of Physical Chemistry, 57, pp. 494-501.

Martynyuk, M.M., 1992, "Superheating of Solid and Liquid Metals in the Process of Pulse Heating", Thermochimica Acta, 206, pp. 55-60.

Meyer, H.W., 2006, "A Modified Zerilli-Armstrong Constitutive Model Describing the Strength and Localizing Behavior of Ti-6Al-4V", Army Research Laboratory Report, ARL-CR-0578.

Meyers, M.A., 1994, Dynamic Behavior of Materials, Wiley-Interscience Publication, New York.

Miklowitz, J., 1969, Wave Propagation in Solids, ASME, New York.

Miotello, A. and Kelly, R., 1995, "Critical Assessment of Thermal Models for Laser Sputtering at High Fluences", Applied Physics Letters, 67 (24), pp. 3535-3537.

Miotello, A., and Kelly, R., 1999, "Laser-induced Phase Explosion: New Physical Problems when A Condensed Phase Approaches the Thermodynamic Critical Temperature" Applied Physics A, 69, pp. S67-S73.

Mitchell, A.C., and Nellis, W.J., 1981, "Shock Compression of Aluminum, Copper, and Tantalum", Journal of Applied Physics, 52 (5), pp. 3363-3374.

Mo, Naeem, 2008, "Laser Cutting of Composites and Ceramics", Technical Report, GSI Group, Laser Division.

More, R.M., Warren, K.H., Young, D.A., and Zimmerman, G.B., 1988, "A New Quotidian Equation of State (QEOS) for Hot Dense Matter", Physics Fluids 31 (10), pp. 3059-3078.

Morel, V., Bultel, A., and Cheron, B.G., 2009, "The Critical Temperature of Aluminum", International Journal of Thermophysics, 30, pp. 1853-1863.

Muhammad, N., Rogers, B.D., and Li, L., 2013, “Understanding the Behavior of Pulsed Laser Dry and Wet Micromachining Processes by Multi-phase Smoothed Particle Hydrodynamics (SPH) Modeling”, Journal of Physics D: Applied Physics, 46, 095101.

Nichols, W.T., Sasaki, T., and Koshizaki, N., 2006, “Laser Ablation of a Platinum in Water. I. Ablation Mechanisms”, Journal of Applied Physics, 100, 114911.

Ohara, J., Nagakubo, M., Kawahara, N., Hattori, T., 1997, “High Aspect Ratio Etching by Infrared Laser Induced Micro Bubbles”, Proceedings of the IEEE Tenth Annual International Workshop on Micro Electro Mechanical Systems, New York: IEEE, pp. 175-179.

Ogitsu, T., Benedict, L.X., Schwegler, E., Draeger, E.W., and Prendergast, D., 2009, “First-principles Calculations of Solid and Liquid Aluminum Optical Absorption Spectra near the Melting Curve: Ambient and High-pressure Results", Physical Review B, 80, 214105.

Pallav, K., Han, P., Ramkumar, J., Nagahanumaiah, Ehmann, K.F., 2011, “Comparative Assessment of the Laser Induced Plasma Micro-machining (LIP-MM) and the Micro-EDM Processes”, Proceedings of the ASME 2011 International Manufacturing Science and Engineering Conference, June 13-17, 2011, Corvallis, Oregon.

Peikrishvili, A.B., Japaridze, L.A., Staudhammer, K.P., Marquis, F.S., Chikhradze, N.M., Gobejishvili, T.G., and Bantzuri, E.G., 2000, “Explosive Compaction of Clad Graphite Powders and Obtaining of Coating on Their Base”, Proceedings of EXPLOMET 2000, International Conference on Fundamental Issues and Applications of Shock-Wave and High-Strain-Rate Phenomena, Staudhammer, K.P. et al., eds, Albuquerque, NM, pp. 249-258.

Perez, D., Lewis, L.J., Lorazo, P., and Meunier, M., 2006, “Ablation of Molecular Solids under Nanosecond Laser Pulses: The Role of Inertial Confinement”, Applied Physics Letters, 89, 141907.

Peters, D.J., 1978, “HUFF, a One-Dimensional Hydrodynamics Code for Strong Shocks”, Master Thesis, Air Force Institute of Technology.

Peyre, P., Berthe, L., Scherpereel, X., Fabbro, R., 1998, "Laser-shock Processing of Aluminium-coated 55C1 Steel in Water-confinement Regime, Characterization and Application to High-cycle Fatigue Behavior", Journal of Materials Science, 33, pp. 1421-1429.

Peyre, P., Sollier, A., Chaieb, I., Berthe, L., Bartnicki, E., Braham, C., and Fabbro, R., 2003, “FEM Simulation of Residual Stresses Induced by Laser Peening,” European Physical Journal: Applied Physics, 23 (2), pp. 83-88.

Peyre, P., Chaieb, I., and Braham, C., 2007, "FEM Calculation of Residual Stress Induced by Laser Shock Processing in Stainless Steels", Modeling and Simulation in Materials Science and Engineering, 15, pp. 205-221.

Porneala, C., and Willis, D.A., 2006, "Observation of Nanosecond Laser-induced Phase Explosion in Aluminum", Applied Physics Letters, 89, 211121.

Preuss, S., Demchuk, A., and Stuke, M., 1995, "Sub-picosecond UV Laser Ablation of Metals", Applied Physics A, 61 (1), pp. 33-37.

Puck, A. and Schurmann, H., 2002, "Failure Analysis of FRP Laminates by Means of Physically Based Phenomenological Models", Composites Science and Technology, 62 (12-13), pp. 1633-1662.

Ree, F.H., 1976, Report No. UCRL-52190 (unpublished).

Rubio-González, C., Gomez-Rosas, G., Ocaña, J.L., Molpeceres, C., Banderas, A., Porro, J., Morales, M., 2006, "Effect of an Absorbent Overlay on the Residual Stress Field Induced by Laser Shock Processing on Aluminum Samples", Applied Surface Science, 252, pp. 6201-6205.

Saarela, J.M., Lofqvist, T., Ramser, K., Gren, P., Olson, E., Niemi, J., Sjodahl, M., 2010, "Detection of Laser Induced Dielectric Breakdown in Water using a Laser Doppler Vibrometer", Central European Journal of Physics, 8 (2), pp. 235-241.

Shannugam, D.K., Chen, F.L., Siores, E., Brandt, M., 2002, "Comparative Study of Jetting Machining Technologies over Laser Machining Technology for Cutting Composite Materials", Composite Structures, 57, pp. 289-296.

Singh, J.K., Adhikari, J. and Kwak, S.K., 2006, "Vapor-liquid Phase Coexistence Curves for Morse Fluids", Fluid Phase Equilibria, 248, pp. 1-6.

Sokolowski-Tinten, K., Bialkowski, J., Cavalleri, A., von der Linde, D., Oparin, A., Meyer-terVehn, J., and Ansimov, S.I., 1998, "Transient States of Matter during Short Pulse Laser Ablation", Physical Review Letters, 81, pp. 224-227.

Sollier, A., Berthe, L., and Fabbro, R., 2001, "Numerical Modeling of the Transmission of Breakdown Plasma Generated in Water during Laser Shock Processing", The European Physical Journal Applied Physics, 16, pp. 131-139.

Sollier, A., Berthe, L., Peyre, P., Bartnicki, E., and Fabbro, R., 2003, "Laser-matter Interaction in Laser Shock Processing", Proceedings of SPIE, 4831, pp. 463-467.

Sugioka, K. and Cheng, Y., 2013, Ultrafast Laser Processing: From Micro- to Nanoscale, CRC Press, Boca Raton, FL.

Tavassoli, S.H. and Khalaji, M., 2008, “Laser Ablation of Preheated Copper Samples”, Journal of Applied Physics, 103, 083118.

Thoma, K., Hornemann, U., Sauer, M., and Schneider, E., 2005, “Shock Waves – Phenomenology, Experimental, and Numerical Simulation”, Meteoritics & Planetary Science, 40, pp. 1283-1298.

Tollier, L., Fabbro, R., and Bartnicki, E., 1998, “Study of the Laser-driven Spallation Process by the Velocity Interferometer System for Any Reflector Interferometry Technique. I. Laser-shock Characterization”, Journal of Applied Physics, 83 (3), pp. 1224-1230.

Tong, M., Browne, D.J., 2011, “Smoothed Particle Hydrodynamics Modeling of the Fluid Flow and Heat Transfer in the Weld Pool during Laser Spot Welding”, Materials Science and Engineering, 27, pp. 1-7.

Urech, L., Lippert, T., Phipps, C.R., and Wokaun, A., 2007, “Polymer as Fuel for Laser-based Microthrusters: An Investigation of Thrust, Material, Plasma and Shockwave Properties”, Applied Surface Science, 253 (19), pp. 7646-7650.

Vasu, A. and Grandhi, R.V., 2013, “Effects of Curved Geometry on Residual Stress in Laser Peening”, Surface and Coatings Technology, 218, pp. 71-79.

Vladoiu, I., Stafe, M., Negutu, C., and Popescu, I.M., 2008, “The Dependence of the Ablation Rate of Metals on Nanosecond Laser Fluence and Wavelength”, Journal of Optoelectronics and Advanced Materials, 10 (12), pp. 3177-3181.

Von Allmen, M., 1987, Laser-Beam Interactions with Materials: Physical Principles and Applications, Springer Series in Material Science, Vol. 2, Springer-Verlag, New York.

Voothaluru R., Liu C.R., and Cheng, G.J., 2012, “Finite Element Analysis of the Variation in Residual Stress Distribution in Laser Shock Peening of Steels”, Journal of Manufacture Science and Engineering, 134(6), 061010.

Warren, A.W., Guo, Y.B., Chen, S.C., 2008, “Massive Parallel Laser Shock Peening: Simulation, Analysis, and Validation”, International Journal of Fatigue, 30 (1), pp. 188-197.

Wolynski, A., Herrmann, T., Mucha, P., Haloui, H., and L’huillier, J., 2011, “Laser Ablation of CFRP Using Picosecond Laser Pulses at Different Wavelengths from UV to IR”, Physics Procedia, 12, pp. 292-301.

Wu, B. and Shin, Y.C., 2005, “A Self-closed Thermal Model for Laser Shock Peening under the Water Confinement Regime Configuration and Comparisons to Experiments”, Journal of Applied Physics, 97 (11), 113517.

Wu, B. and Shin, Y.C., 2006a, "Absorption Coefficient of Aluminum near the Critical Point and the Consequences on High-power Nanosecond Laser Ablation", Applied Physics Letters, 89, 111902.

Wu, B. and Shin, Y.C., 2006b, "Laser Pulse Transmission through the Water Breakdown Plasma in Laser Shock Peening", Applied Physics Letters, 88 (4), 041116.

Wu, B. and Shin, Y.C., 2006c, "Modeling of Nanosecond Laser Ablation with Vapor Plasma Formation", Journal of Applied Physics, 99, 084310.

Wu, B. and Shin, Y.C., 2007a, "A One-dimensional Hydrodynamic Model for Pressures near the Coating-water Interface during Laser Shock Peening", Journal of Applied Physics, 101, 023510.

Wu, B. and Shin, Y.C., 2007b, "Two Dimensional Hydrodynamic Simulation of High Pressures Induced by High-power Nanosecond Laser-matter Interactions under Water", Journal of Applied Physics, 101, 103514.

Wu, B. and Shin, Y.C., 2007c, "From Incident Laser Pulse to Residual Stress: A Complete and Self-Closed Model for Laser Shock Peening", Transactions of the ASME, Journal of Manufacturing Science and Engineering, 129, pp. 117-125.

Wu, B. and Shin, Y.C., 2007d, "A Simple Two-stage Model for the Formation and Expansion of the Plasma Induced by High intensity Nanosecond Laser Metal Ablation in Vacuum", Physics Letters A, 371, pp. 128-134.

Wu, B., Shin, Y.C., Pakhal, H., Laurendeau, N.M., and Lucht, R.P., 2007e, "Modeling and Experimental Verification of Plasmas Induced by High-power Nanosecond Laser-aluminum Interactions in Air", Physical Review E, 76, 026405.

Xu, X and Willis, D., 2002, "Non-Equilibrium Phase Change in Metal Induced by Nanosecond Pulsed Laser Ablation", Journal of Heat Transfer, A292, pp. 162-168.

Yoo, J.H., Jeong, S.H., Mao, X.L., Greif, R., and Russo, R.E., 2000, "Evidence for Phase-explosion and Generation of Large Particles during High Power Nanosecond Laser Ablation of Silicon", Applied Physics Letters, 76, pp. 783-785.

Young, D.A. and Alder, B.J., 1971, "Critical Point of Metals from the Van Der Waals Equation of State", Physical Review A, 3 (1), pp. 364-371.

Zhang, L. and Wang, X., 2008, "Hybrid Atomistic-Macroscale Modeling of Long-time Phase Change in Nanosecond Laser-Material Interaction", Applied Surface Science, 255, pp. 3097-3103.

Zhang, W. and Yao, Y.L., 2002, "Micro Scale Laser Shock Processing of Metallic Components", Transactions of the ASME, Journal of Manufacturing Science and Engineering, 124, pp. 369-378.

Zhang, W., Yao, Y.L., and Noyan, I.C., 2004, "Microscale Laser Shock Peening of Thin Films, Part 1: Experiment, Modeling and Simulation", Transactions of the ASME, Journal of Manufacturing Science and Engineering, 126, pp. 10-17.

Zhigilei, L.V. and Ivanov, D.S., 2005, "Channels of Energy Redistribution in Short-pulse Laser Interactions with Metal Targets", Applied Surface Science, 248(1-4), pp. 433-439.

APPENDIX

APPENDIX

Some additional experimental observations and MD/SPH prediction results for the copper cases in Chapter 4 are attached here.

Case 1: laser fluence of 42 J/cm^2

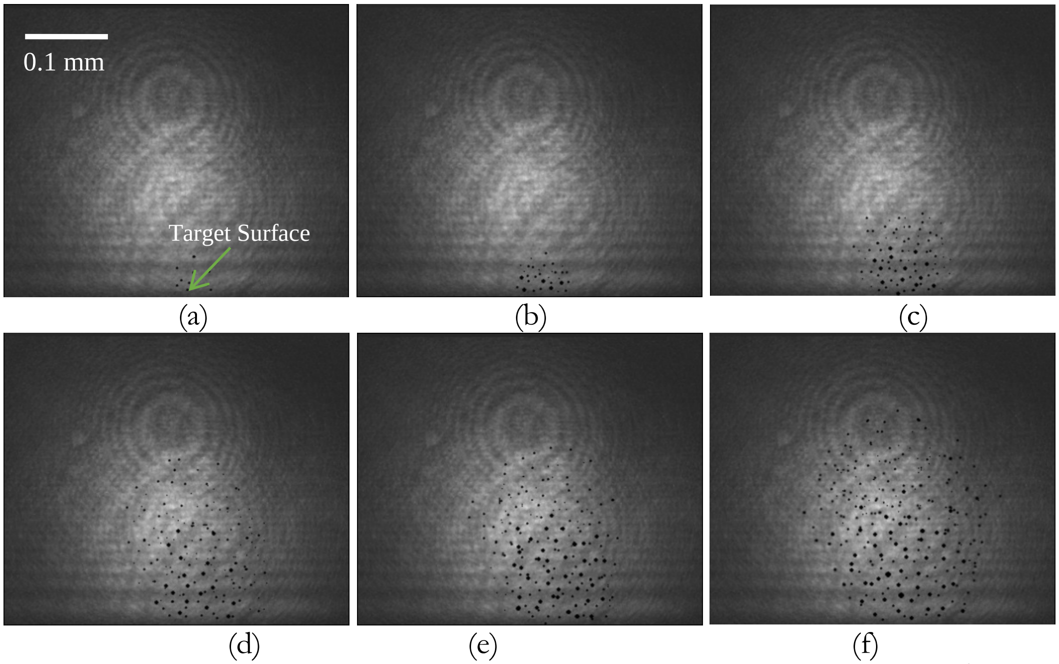

Figure A.1. Experimental observation of melt ejection under laser fluence 42 J/cm^2 (a) t = 50 ns (b) t = 55 ns (c) t = 60 ns (d) t = 65 ns (e) t = 70 ns (f) t = 75 ns (copper target, laser beam coming from the top of the image, pulse duration 6 ns, 1064 nm, beam diameter 100 μm).

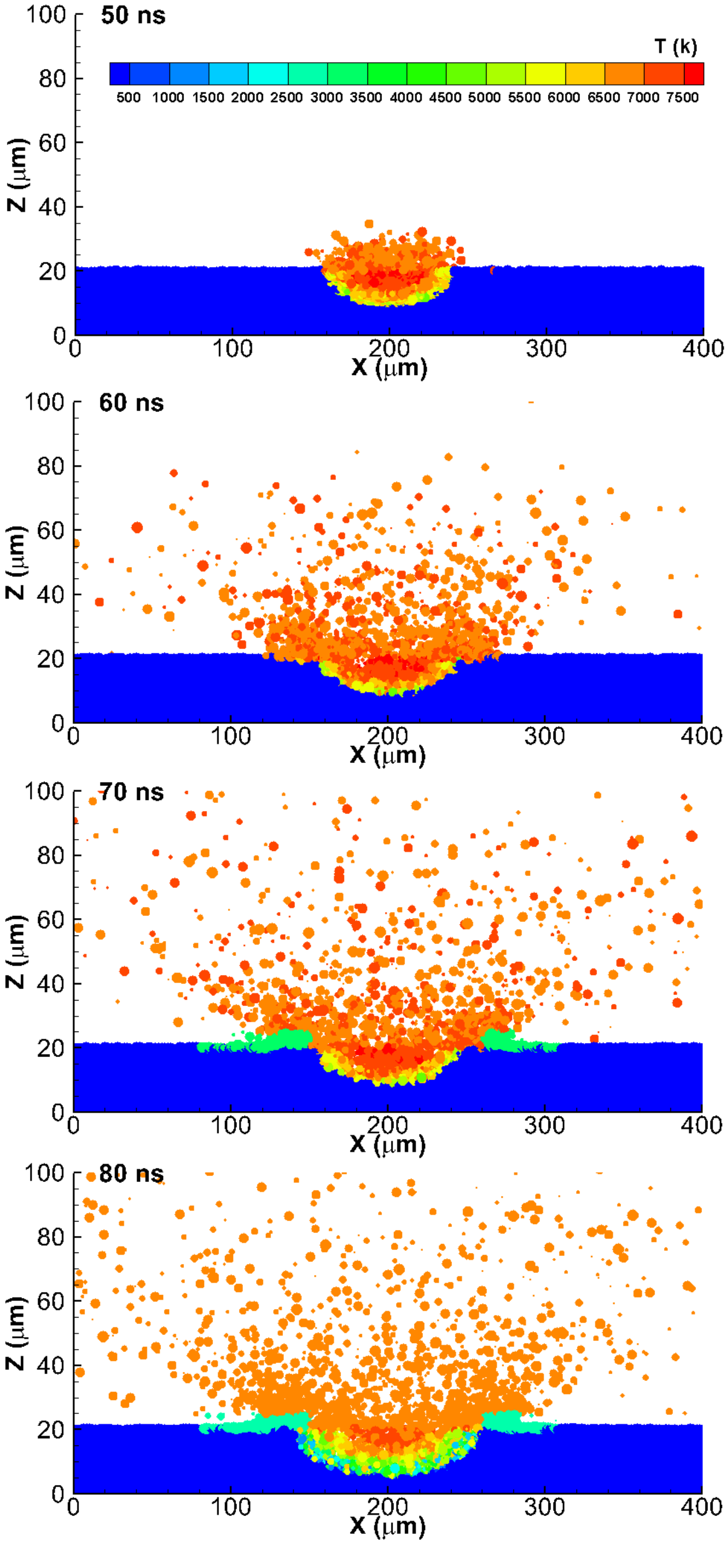

Figure A.2. SPH calculation results showing the melt ejection for copper (laser fluence 42 J/cm^2, wavelength 1064 nm, pulse duration 6 ns, beam diameter 100 μm).

Case 2: laser fluence of 48 J/cm^2

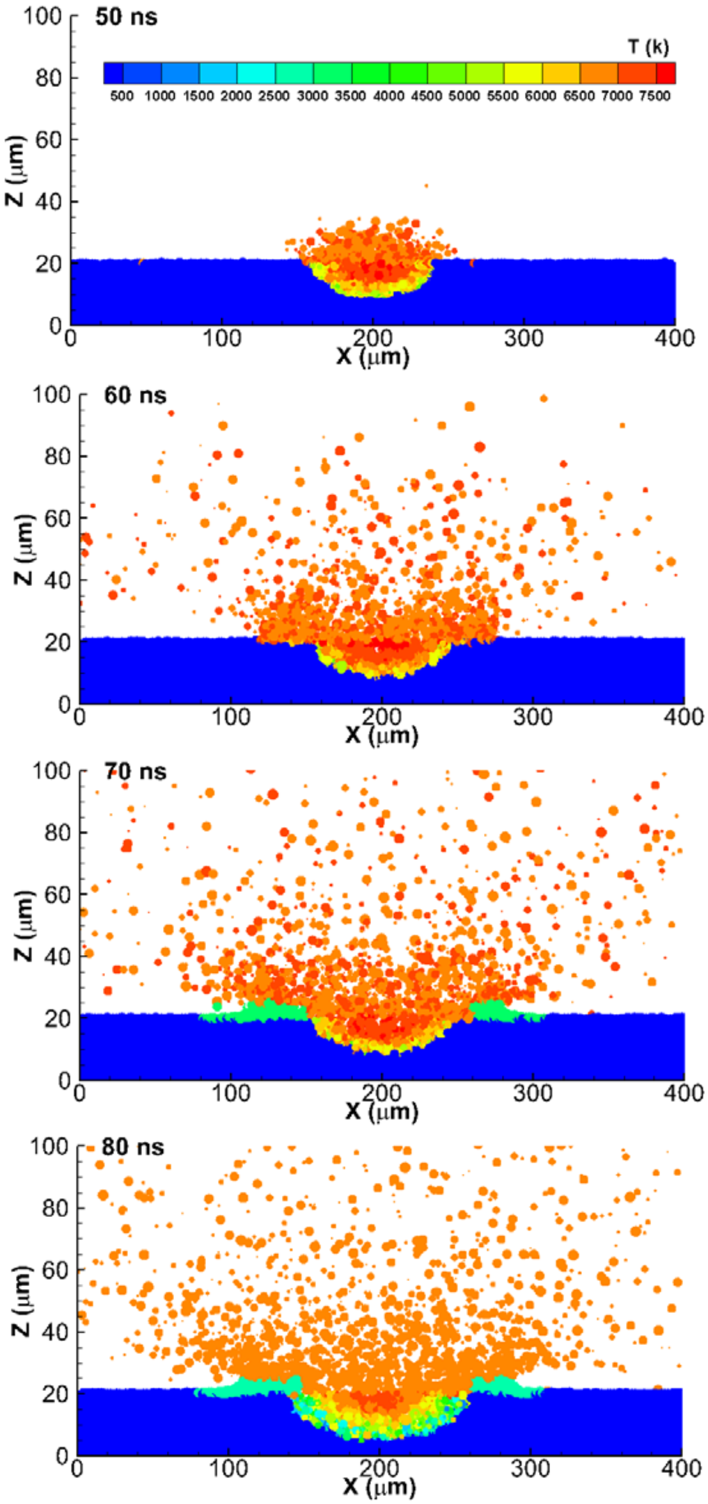

Figure A.3. SPH calculation results showing the melt ejection for copper (laser fluence 48 J/cm^2, wavelength 1064 nm, pulse duration 6 ns, beam diameter 100 µm).

Case 3: laser fluence of 54 J/cm^2

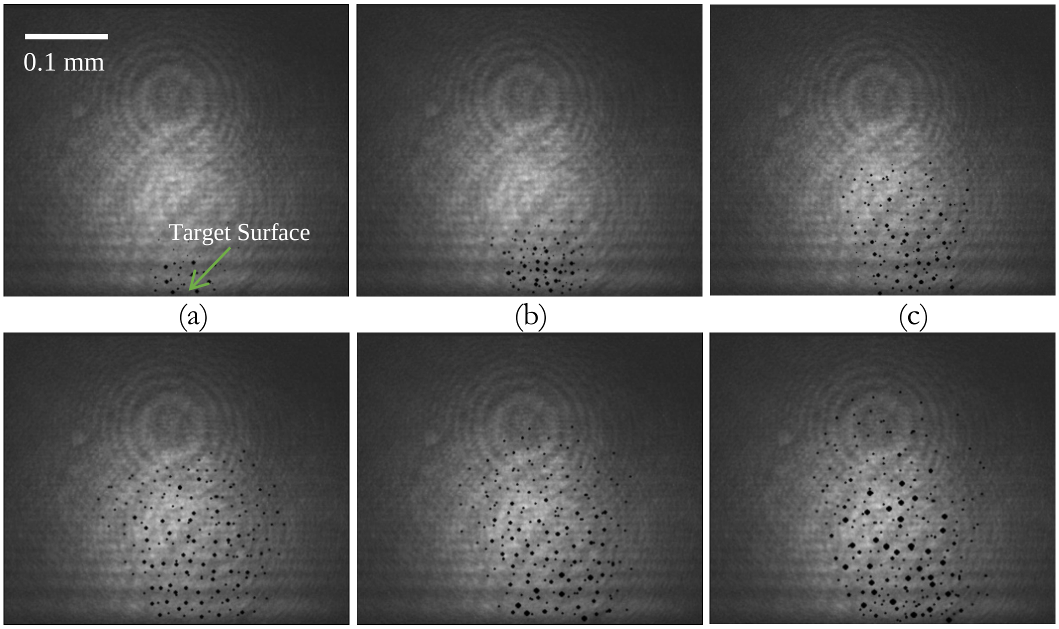

(a) (b) (c)

(d) (e) (f)

Figure A.4. Experimental observation of melt ejection under laser fluence 54 J/cm^2 (a) t = 50 ns (b) t = 55 ns (c) t = 60 ns (d) t = 65 ns (e) t = 70 ns (f) t = 75 ns (copper target, laser beam coming from the top of the image, pulse duration 6 ns, 1064 nm, beam diameter 100 μm).

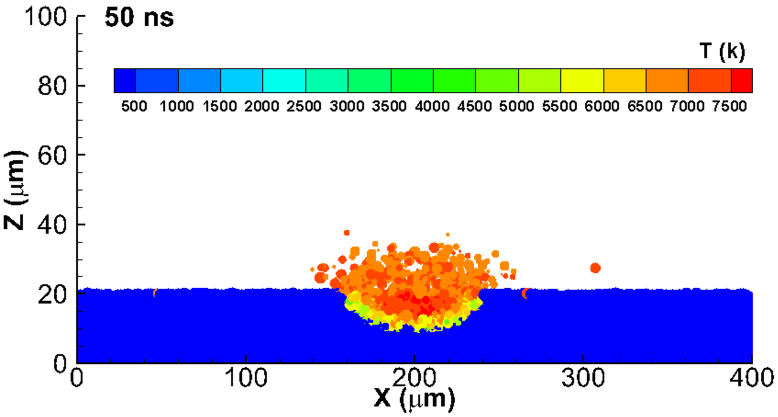

Figure A.5. SPH calculation results showing the melt ejection for copper (laser fluence 54 J/cm^2, wavelength 1064 nm, pulse duration 6 ns, beam diameter 100 μm).

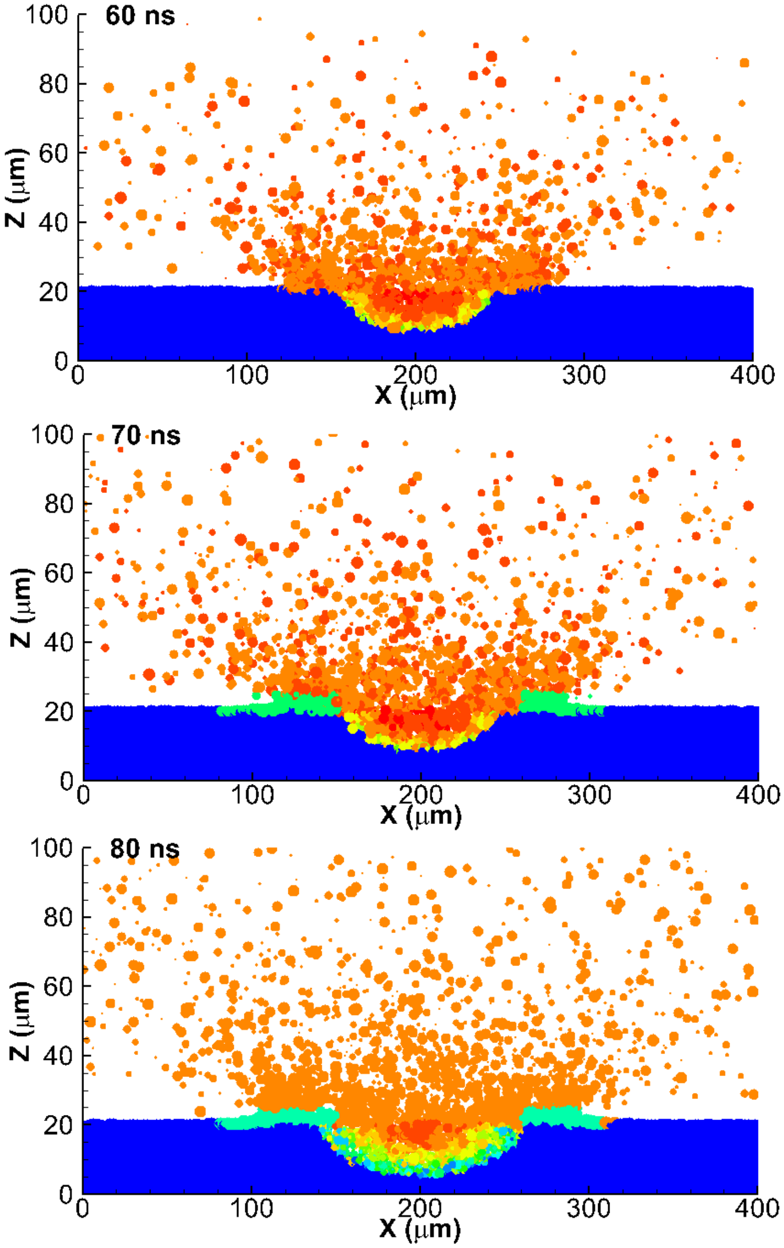

Figure A.5. Continued.

VITA

VITA

Yunfeng Cao was born in Henan Province, China. He graduated from Tsinghua University (Beijing, China) with both B.S. and M.S. degrees in Mechanical Engineering. Before joining Purdue University in 2006, he studied in Missouri University of Science and Technology (formerly University of Missouri, Rolla) and obtained a M.S. degree in Mechanical Engineering. He is currently a Ph. D candidate in the school of Mechanical Engineering at Purdue.

His research at Purdue under the direction of Prof. Yung C. Shin focuses on nanosecond laser matter interaction, laser shock peening, laser-induced water breakdown plasma etching, and melt ejection during phase explosion.